Analysis and modeling of the rear side of industrial-type passivated emitter and rear silicon solar cells

von

Dipl.-Phys. Christopher Kranz

geboren am 30.06.1985 in Minden

2016

Kurzzusammenfassung

Solarzellhersteller führen momentan Solarzellen mit passiviertem Emitter und passivierter Rückseite (PERC) in die Massenproduktion ein als einen möglichen Nachfolger der momentan am Markt dominierenden Solarzelle mit ganzflächigem *back surface field* (BSF). Da der Unterschied beider Solarzellen von einer Verbesserung der Rückseite herrührt, zielt diese Arbeit darauf ab, Effekte des neuen Rückseitendesigns und der dafür nötigen Prozesse zu analysieren und zu modellieren.

Wir analysieren den Einfluss der Rückseitenrauigkeit auf industrietypische PERC-Solarzellen, die Al_2O_3/SiN_x oder SiO_2/SiN_x als rückseitigen Passivierstapel verwenden. Wir beobachten einen kleineren Einfluss im Falle von Al_2O_3/SiN_x, der bereits geringe effektive Oberflächenrekombinationsgeschwindigkeiten $S_{rear} = 100\,cm/s$ für niedrige Polituraberträge von $5\,\mu m$ an einer vorher texturierten Oberfläche aufweist. Dadurch, dass sich die interne Reflexion an planaren Rückseiten im Vergleich zu texturierten Rückseiten nur um etwa 1.5%abs erhöht, steigt die Kurzschlussstromdichte bedingt durch verbesserten Lichteinfang um höchstens $0.2\,mA/cm^2$. Die um 1%abs gesteigerten Wirkungsgrade von stark polierten PERC-Solarzellen gegenüber texturierten PERC-Solarzellen sind daher vor allem auf reduzierte Rekombination zurückzuführen. Ein neuer industrienaher Prozessfluss, der doppelseitige Textur, doppelseitige Diffusion und einseitige Politur beinhaltet, ermöglicht Wirkungsgrade von bis zu 20.7%, was vergleichbar ist zu Referenz-PERC-Zellen, die eine Rückseitenschutzschicht anstelle eines Politurprozesses verwenden. Wir untersuchen zudem verschiedene industrierelevante Reinigungssequenzen vor Al_2O_3/SiN_x-Passivierung und erzielen ausgezeichnete Ergebnisse mit pSC1, HF/HCl, die vergleichbare Wirkungsgrade von 20.4% zur Labor-RCA-Reinigung liefert.

Wir ermitteln eine obere Grenze von $\rho_c < 5\,m\Omega cm^2$ für den Kontaktwiderstand des siebgedruckten Al zum Si an der Rückseite der PERC-Solarzellen, sowohl mittels Transferlängenmethode (TLM) als auch einer Variation des rückseitigen Kontaktabstandes bei PERC-Zellen. Wir bestimmen die BSF-Tiefen von PERC- und bifazialen PERC+-Solarzellen. Bei einer Kontaktbreite von $60\,\mu m$ beobachten wir im Falle von PERC+ signifikant tiefere BSFs von $8\,\mu m$ im Vergleich zu $4\,\mu m$ im Falle von PERC. Die Anpassung eines vorhandenen analytischen Modells zur Berechnung von BSF-Tiefen an den PERC+ Fall resultiert in ausgezeichneter Übereinstimmung zwischen Modell und Experiment und zeigt, dass die tieferen BSFs ihre Ursache in der geringeren, rückseitig aufgebrachten Al-Masse haben. Entsprechend und im Gegensatz zu PERC erreichen die PERC+ Zellen damit sogar für schmale Kontaktlinien von $48\,\mu m$ hohe Wirkungsgrade von 21.1%. Erstmalig zeigen wir in dieser Arbeit, dass die Häufigkeit von Hohlräumen in den Kontakten (sog. *Voids*) von der Kontakthöhe abhängt. Wir stellen ein neues analytisches Modell vor, das die *Void*-Entstehung als einen Effekt der Oberflächenenergieminimierung der flüssigen Al-Si Schmelze während des Feuerns beschreibt und damit den vorher vorgeschlagenen Kirkendall-Effekt als mögliche Ursache verwirft. Das neue Modell ist insbesondere in der Lage die Kontakthöhenabhängigkeit der *Voids* zu beschreiben.

Schlagworte: industrielle Silizium-Solarzellen, nasschemische Politur, Kontaktbildung

Abstract

Solar cell manufacturers are currently introducing the passivated emitter and rear cell (PERC) into mass production as a potential successor of the currently commercially dominating full area back surface field (BSF) solar cell. As the difference between both solar cells arises from an improvement of the rear side, this work aims at analyzing and modeling effects introduced by the new rear side design and processes.

We analyze the impact of the rear surface roughness on industrial-type PERC cells applying Al_2O_3/SiN_x or SiO_2/SiN_x passivation layer stacks. We find a smaller impact in case of Al_2O_3/SiN_x, which exhibits small effective rear surface recombination velocities $S_{rear} = 100\,cm/s$ even for low polishing removals of $5\,\mu m$ at a previously textured surface. As the internal reflectance at the rear only increases by 1.5%abs when comparing textured to planar, the corresponding increase in short circuit current density caused by improved light trapping is determined to a maximum value of $0.2\,mA/cm^2$. The efficiency improvement of 1%abs of strongly polished PERC cells compared to PERC cells with textured rear sides is therefore primarily caused by recombination. Based on these results, we develop a lean industrial-type PERC process flow including double-sided texturing, double-sided phosphorus diffusion and single-sided polishing which achieves up to 20.7% efficiency and is comparable to reference PERC cells using a rear protection layer instead of a polishing step. We investigate different industrially feasible cleans prior to Al_2O_3/SiN_x-passivation and achieve excellent results using pSC1, HF/HCl, which yields efficiencies up to 20.4%, comparable to a laboratory-type RCA clean. An even shorter cleaning sequence of HF/O_3 in a single step, however, causes a roughening of the n^+-doped front surface of the solar cell that leads to increased surface recombination and lower efficiency.

We determine an upper limit of $\rho_c < 5\,m\Omega cm^2$ for the contact resistivity of the screen printed local Al contacts to the silicon Si bulk at the rear of the PERC solar cells using the transfer length method as well as a rear contact pitch variation of PERC cells. We measure the depths of the BSFs of PERC and bifacial PERC+ solar cells, which feature an Al finger grid on the rear side instead of a full area Al layer. At a contact width of $60\,\mu m$ we find significantly deeper BSFs of $8\,\mu m$ for PERC+ compared to $4\,\mu m$ for PERC. Adaption of an existing analytical model for calculation of BSF depths to the PERC+ case results in excellent agreement between model and experimental data and indicates that the deeper BSFs are a consequence of the smaller Al mass printed to the rear side. Accordingly and in contrast to PERC, the PERC+ cells achieve high efficiencies of 21.1% even for narrow contact lines of $48\,\mu m$. For the first time, we show that the amount of voids in local Al-contacts depends on the contact height. We propose a new analytical model that describes void formation as an effect of surface energy minimization of the liquid Al-Si melt during firing rather than the previously suggested Kirkendall effect. The new model is in particular able to describe the observed height dependency of voids.

Keywords: industrial-type silicon solar cells, wet chemical polishing, contact formation

Contents

Contents

Introduction

A frequently used measure to compare the cost of electrical power generation between different sources is the levelized cost of electricity (LCOE) measured in USD/kWh. The LCOE of photovoltaic electricity constantly decreased in the past and is today at a typical value of $0.093\,\mathrm{USD/kWh}$ [1]. In order to further decrease the cost, it is therefore necessary to either improve the efficiency of the solar modules or to reduce the production cost. The latter can be achieved by reducing the production process complexity or by saving material.

The efficiency of a solar cell is the ratio of electrical power output density P_{out} to the power density of the incident light P_{in}:

$$\eta = \frac{P_{\mathrm{out}}}{P_{\mathrm{in}}} = \frac{J_{\mathrm{sc}} \cdot V_{\mathrm{oc}} \cdot FF}{P_{\mathrm{in}}}, \tag{0.1}$$

where J_{sc} is the short circuit current density, V_{oc} the open circuit voltage and FF the fill factor of a measured I-V-curve of the illuminated solar cell. Improving the capability of a solar cell to absorb light (rather than reflecting it), mainly increases the generated current density J_{gen} in the cell and thus the J_{sc}. In contrast, avoiding resistive losses primarily improves the fill factor FF. Assuming a one diode model for the I-V-curve the V_{oc} is given by

$$V_{\mathrm{oc}} = \frac{kT}{q} \ln\left(\frac{J_{\mathrm{gen}}}{J_0} + 1\right) \tag{0.2}$$

with the Boltzmann constant k, the electron charge q, the temperature T and the total saturation current density J_0, which is a measure of the total recombination of charge carriers within a solar cell. Avoiding recombination accordingly increases the open circuit voltage of a solar cell.

Up to date the aluminum back surface field (Al-BSF) silicon solar cells dominate the commercial market with a share of around 87% in 2015 [2]. As shown in Figure 0.1a) these solar cells owe their name to the full-area Al-BSF, a p^+-doped region of silicon (Si) at the rear side of the Si wafer. Al-BSF solar cells achieve up to 19.9% efficiency in research & development (R&D) [3] and about 19% in production lines [4].

In recent years, however, the industry and research institutes developed an industrial-type passivated emitter and rear cell (PERC). These PERC cells currently
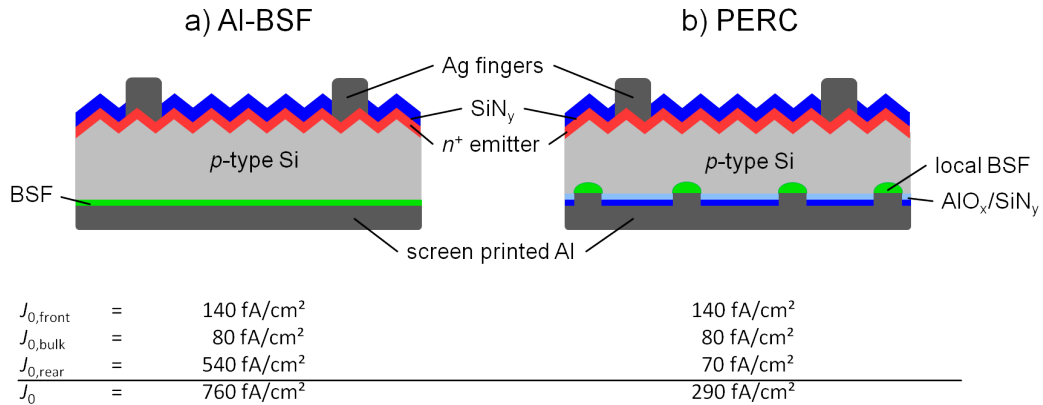
a) Al-BSF

b) PERC

		a) Al-BSF	b) PERC
$J_{0,\text{front}}$	=	140 fA/cm²	140 fA/cm²
$J_{0,\text{bulk}}$	=	80 fA/cm²	80 fA/cm²
$J_{0,\text{rear}}$	=	540 fA/cm²	70 fA/cm²
J_0	=	760 fA/cm²	290 fA/cm²

Figure 0.1: Schematic drawing of a full-area Al-BSF (a) and a PERC (b) solar cell. In principle the only difference between the two solar cell concepts is the design of the rear side, leading to much lower saturation current densities J_0 in case of PERC. The J_0 values are summarized from Ref. [5] and [6].

achieve efficiencies of up to 22.1% in R&D [7,8] and just entered mass production. They are expected to gain a market share of over 30% until 2019 [9]. As illustrated in Figure 0.1b) the wafer rear side of PERC solar cells is covered by a dielectric passivation layer stack and only locally contacts the rear Al paste. Also, the Al-BSF is only formed locally. The advantage of this design is twofold. On the one hand, the internal reflection of light at passivated areas is comparably high with typical values above 90%, whereas the metalized rear side of Al-BSF cells only exhibits values around 65% [10, 11]. This leads to an improved light trapping and higher short circuit current densities of PERC solar cells. On the other hand, the contact recombination is reduced due to the smaller metalized rear surface area. As shown in Figure 0.1 this leads to a significantly smaller J_0-contribution from the rear side.

The resulting enhanced efficiency of PERC solar cells, however, comes at the cost of at least two additional process steps. The first is the deposition of the passivation layer stack and the second the formation of the local contact geometry. Although, at a first glance, this change in solar cell design might appear to be manageable, there is a variety of questions, that arises, when migrating from Al-BSF to PERC solar cell technology: What is an ideal rear surface roughness and cleaning prior to rear side passivation? As the fraction of contacted area is much smaller, will the contact resistance become an important power loss mechanism? What are the fundamentally new aspects of local contact- and BSF-formation compared to the full-area metalization? What is an ideal rear contact geometry? "Ideal" in this context always means "enabling low cost and highest efficiencies simultaneously". This work attempts to answer these questions that are all related to the rear side of PERC solar cells.

This thesis is structured as follows:

- **Chapter 1** briefly sketches the progress in PERC cell development during recent years and points out important technology options for PERC solar cells.

- **Chapter 2** presents the most important characterization techniques used in this work. Current voltage measurements as well as quantum efficiency measurements are frequently used to describe fabricated solar cells. Surface recombination is often assessed by photoconductance decay measurements on test samples. The contact resistivity of Al-contacts is determined using the transfer length method.

- **Chapter 3** summarizes the preparative work required for the experiments of this thesis. It gives details on the frequently used reference PERC process and introduces the bifacial PERC+ solar cell. Additionally, previous work on the main topics of this thesis is presented.

- **Chapter 4** covers polishing and cleaning of the rear side of PERC solar cells. The impact of the rear surface roughness is investigated and, based on these results, a novel and lean process flow for polished PERC cells is presented. Finally, different cleanings prior to passivation layer deposition are evaluated.

- **Chapter 5** covers the screen printed local Al-contacts of PERC solar cells. The contact resistivity is determined using two different methods. Furthermore, the physical differences in contact formation between PERC and PERC+ solar cells are analyzed. A new physical root cause along with an analytical model is proposed to describe voids within the local contacts, which are commonly observed for PERC solar cells. Additionally, different dashed line rear contact geometries are investigated.

- **Chapter 6** applies the simulation-based synergetic efficiency gain analysis (SEGA) to the PERC solar cell with a record efficiency of 21.2%, which was fabricated in the context of this work. The SEGA allows to identify the major power loss mechanisms and compares them on an equal footing.

- **Chapter 7** summarizes the results of this work.

1

Industrial PERC solar cells

The passivated emitter and rear cell (PERC) was introduced by Blakers et al. [12] in 1989. The presented laboratory-type PERC cell with a cell area of 2x2 cm^2 was fabricated on 0.2 Ωcm p-type float zone (FZ) material and achieved an efficiency of 22.8%. Based on this PERC design the same research group further developed a passivated emitter, rear locally diffused (PERL) solar cell, which achieved an efficiency of up to 24.7% [13] in 1999. This efficiency was later corrected to be 25.0% [14] after the irradiation spectrum for measuring solar cells under standard testing conditions have been redefined in 2008. The 25.0% had been the record efficiency for silicon solar cells for about 15 years until Panasonic achieved an efficiency of 25.6% [15] with a back contacted heterojunction solar cell in 2014.

As shown in Figure 1.1, the only difference between the mentioned PERC and PERL solar cells is the addition of a local rear diffusion at the areas of the point contacts in case of PERL. The resulting p^+ doped local back surface fields (BSFs) reduce recombination at the contacts of the Si wafer to the evaporated Al. For both solar cells, however, multiple structuring steps including photolitography were applied in order to form the inverted pyramids front texture, the highly selective emitter produced by two phosphorus diffusions, and the finger geometry using evaporation of Ti and Pd and subsequent Ag plating. These processes as well as the used FZ material are too expensive for industrial production.

In 2006 Agostinelli et al. [17] presented a first approach to simplify the PERC process and adopt it for industry achieving 17.6% efficiency. However, it was around 2010 when several solar cell manufacturers and research institutes started development of industrial-type PERC cells. These industrial-type cells feature a practical size of >100 cm^2 and typically apply screen printing to form the metallization on the front and rear side of the solar cell. Also, Czochralski-grown (Cz) or multi-crystalline Si is used as wafer bulk material. Figure 1.2 schematically shows an industrial-type PERC solar cell as manufactured at ISFH [6]. Similar to the PERL structure, these cells have a local BSF at the rear contacts and consequently both cell types are occasionally called LBSF solar cells. However,
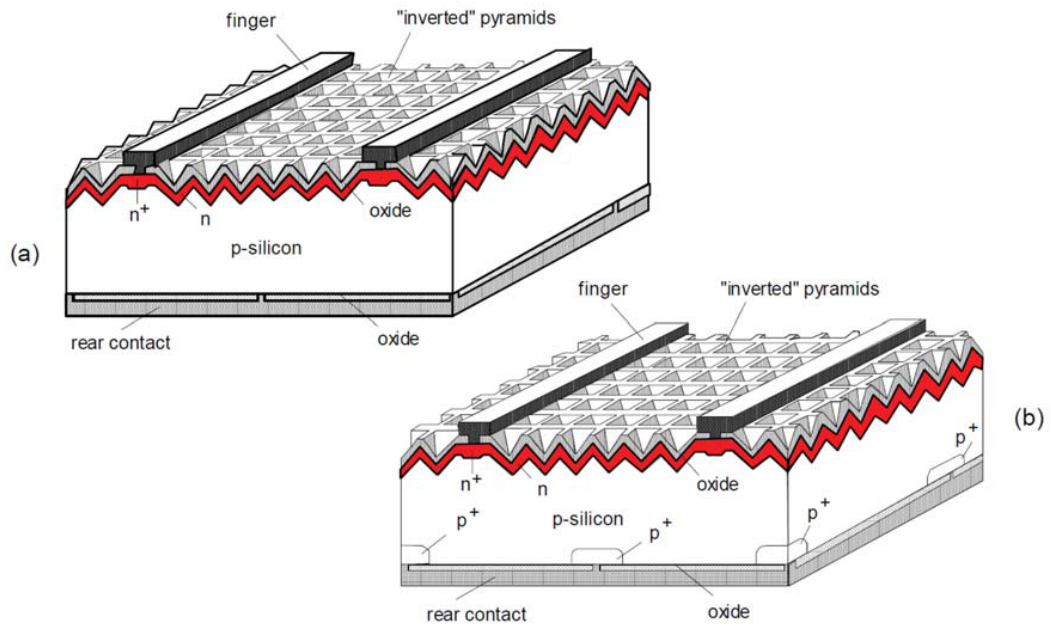
Figure 1.1: Schematic drawings of a laboratory-type PERC (a) and a PERL (b) solar cell with an efficiency of 22.8% [12] and 25.0% [14], respectively. The only difference between both solar cell concepts is the local p^+-diffusion at the rear point contacts in case of PERL. The image is taken from Ref. [16].
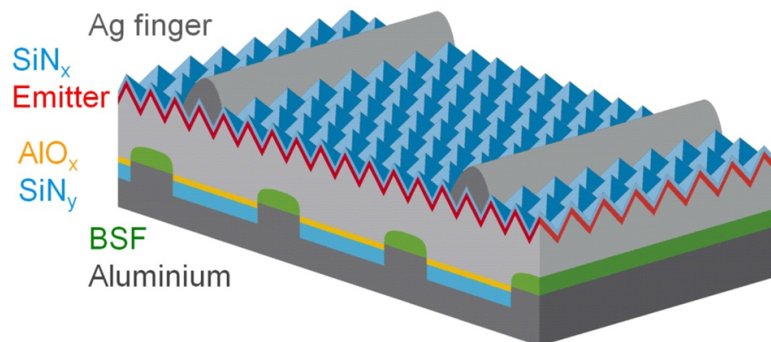
Figure 1.2: Schematic of an industrial-type PERC solar cell as manufactured as ISFH. The solar cell features line contacts at the rear side. The image is taken from Ref. [6].

industrial-type PERC solar cells are generally not considered to be PERL cells, since the p^+ doping profile is not created by diffusion, but results from an Al-Si alloying and Si crystallization process (see section 3.4).

The progress in development of industrial-type PERC solar cells is outlined by Figure 1.3, presenting the record efficiencies from 2010 until today. The first notable
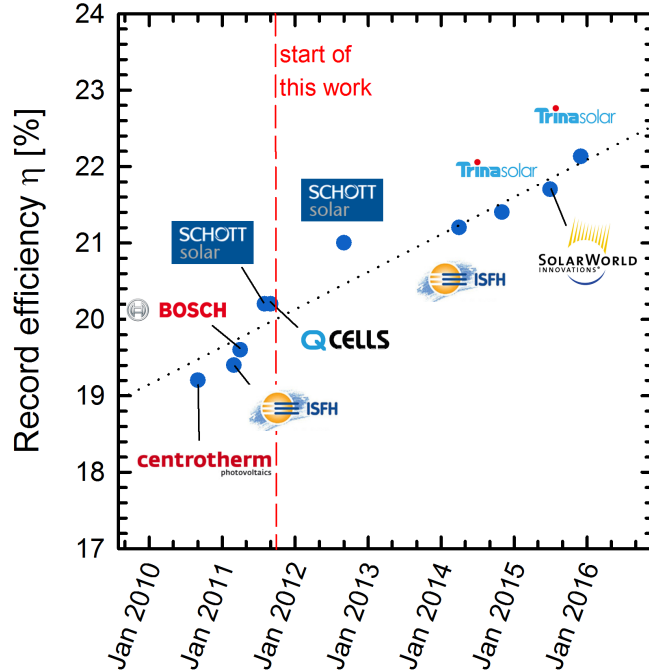
Figure 1.3: Record efficiencies of large-area ($> 100\,\mathrm{cm}^2$) screen printed monocrystalline solar cells from 2010 until today [3, 7, 8, 18–26]. The dotted line is a guide to the eye. The graph is an adapted version of the efficiency chart found in Ref. [27].

result during that time was presented by Centrotherm achieving 19.2% [18] efficiency in 2010. In 2011 the record efficiencies quickly climbed up to 20.2% [21, 22] as reported by Schott Solar and Q.Cells. These results represented the newly published benchmark, when this work started in October 2011. One year later in September 2012 Schott Solar obtained a new record with an efficiency of 21.0% [3, 23] which lasted for 1.5 years until ISFH presented a 21.2%-efficient PERC cell in 2014 [24]. The findings of this work contributed to the development of this 21.2%-efficient solar cell, which is analyzed in detail in chapter 6. During the last two years (2014-2016) it was most notably Trina Solar and SolarWorld reporting new record efficiencies. Up to date both companies have reported comparable values of 22.1% [7, 8] and 22.0% [28], respectively.

Based on the publications summarized by Figure 1.3, we discuss some of the key technologies for PERC solar cells in the following.

Rear contact formation

There are essentially two techniques to form the local contact geometry of industrial-type PERC cells. The laser contact opening (LCO) process locally ablates the rear passivation layer stack prior to Al screen printing to define the contact geometry. The Al-Si alloying process during firing then creates the contact. In contrast, laser fired contacts (LFCs) [29] are formed at the very end of the solar cell process. Here, a laser is used to weld a previously deposited Al-layer to the silicon surface through the rear passivation layer. There are approaches to use the LFC technique in combination with evaporated Al [29], screen printed Al [30] or even conventional aluminum foil [31]. However, the LFC process may induce laser damage to the substrate [30] and generally results in contacts showing no or only very shallow BSFs leading to higher surface recombination velocities at the contacts when compared to LCO. As far as disclosed, most of the record efficiencies of Figure 1.3 are achieved using LCOs [3, 18, 19, 24, 25] whereas only one applied the LFC technique [22].

Screen printed local contacts formed by LCO are a major topic of this work. Hence, the literature is described in more detail in section 3.4, whereas the results of this work are presented in chapter 5.

Rear passivation layer stack

Similar to the laboratory-type PERC cell by Blakers et al. some of the early publications on industrial-type PERC cells report to use a stack of thermal oxide and silicon nitride SiO_x/SiN_y, e.g. Ref. [17] (not included in Figure 1.3) and Ref. [19]. Two of the more recent record efficiencies, however, were achieved applying an AlO_x/SiN_y passivation layer stack [3, 24]. Although thermal SiO_x passivation layers can achieve low surface recombination velocities $<20\,\mathrm{cm/s}$ on low resistivity ($\sim 1\,\Omega\mathrm{cm}$) p-type silicon wafers [32], it has never been adapted by industry due to its nature of a high temperature process [33]. Especially in case of multi-crystalline silicon temperatures above 900°C lead to a significant degradation of the bulk lifetime [34]. In contrast, AlO_x layers are deposited at low temperatures and can also exhibit very low surface recombination velocities $<10\,\mathrm{cm/s}$ on $\sim 2\,\Omega\mathrm{cm}$ material [35]. The high negative fixed charge of AlO_x layers in the order of magnitude $10^{12} - 10^{13}\,\mathrm{cm^{-2}}$ [36, 37] helps to avoid "parasitic shunting" [38] – an effect of enhanced surface recombination that can occur for solar cells applying a rear passivation layer with positive fixed charges, such as SiO_x or SiN_x. Due to those beneficial properties different high-throughput tools like PECVD [39, 40] and spatial ALD [41] for the depostion of AlO_x have been developed in the recent past. Although most of the solar cell manufacturers do not disclose their passivation layers, the AlO_x/SiN_y stack can be considered a mainstream technology as the International Roadmap for Photovoltaic (ITRPV) [2] reports a market share of only 2% for rear passivation technologies other than AlO_x/SiN_y. According to the roadmap this share is even expected to decline in the future.

In this work we compare a SiO_x/SiN_y with an atomic layer deposited Al_2O_3/SiN_y passivation layer stack in section 4.1 and generally obtain higher efficiencies with the latter.

Busbar technology

An attractive way to increase the efficiency of PERC solar cells is to increase the number of busbars (BB) on the front side. This can be achieved by multi-wire module interconnection technologies [42–45] or multi-busbar approaches [6]. An increase of the number of busbars reduces the length of the fingers in-between the busbars and, hence, also the finger line resistance. Alternatively it is possible to increase the finger pitch or decrease the finger width without increasing the total series resistance of the solar cell [46]. However, the application of more – and therefore narrower – busbars introduces new challenges for the module interconnection. Until 2012 a 3 busbar (3BB) layout was the industry-wide standard. The first solar cell in Figure 1.3 reporting a 5BB layout is the 21.2%-efficient solar cell by ISFH in April 2014 [24]. In May 2015 SolarWorld announced to switch their production to the 5BB layout [47]. The 21.7% record efficiency reported two month later [26] is therefore likely to apply the same layout. In industrial production the still dominating 3BB layout is expected to be replaced by 4BB and 5BB layouts in the near future [2].

Emitter technology

Due to the passivated rear side, the efficiency of PERC cells is typically limited by recombination in the emitter at the front surface (compare Figure 0.1 or Chapter 6). For a homogeneous emitter higher sheet resistances and thus lower surface dopant concentrations will result in lower saturation current densities J_{0e} in the passivated areas, but will simultaneously increase the J_{0e} values under the contacts [5]. In addition the contact resistance of the front Ag fingers increases for diffusions with higher sheet resistances. In order to separately optimize the passivated and contacted areas there are different approaches to implement a selective emitter to industrial-type PERC cells using as few additional process steps as possible:

- **Selective laser doping**. During phosphorus diffusion a phosphosilicate glass (PSG) is created on the wafer surface. This PSG can serve as a precursor for a subsequent laser doping process. In this process laser irradiation locally melts the silicon at the wafer surface under the PSG. Additional phosphorus now diffuses from the PSG into the liquid Si phase. Furthermore, interstitial phosphorus atoms are activated in the following re-crystallization process [48, 49]. Laser doping only requires one additional process step.

- **Dopant pastes**. A Dopant paste can be locally screen printed on the front side of the wafer prior to a weak phosphorus diffusion. During this high temperature process phosphorus diffuses from the paste into the adjacent

silicon [50]. The additional process steps for this method are printing and drying of the dopant paste.

- **Selective etch back**. After phosphorus diffusion an etch barrier can be inkjet printed on the areas that will be contacting the Ag fingers [51]. Afterwards a chemical solution etches back the highly doped region of the emitter in-between the future Ag fingers. The etch barrier is then removed. Depending on the applied chemicals and the PSG removal process this technique requires two or three additional process steps. In contrast to the two methods described above etched back (selective) emitters are not limited by the phosphorus surface concentrations achievable by a $POCl_3$ diffusion. Hence, for a given sheet resistance these emitters show lower J_{0e} values [51].

- **Gas phase etch back**. A special variation of the selective etch back is the gas phase etch back (GEB) [52]. Similar to the process described above an etch barrier is locally inkjet printed on the front side emitter after $POCl_3$ diffusion. In the following single sided wet chemical polishing process the reactive gas phase of the polishing bath etches back the front side emitter in between the etch barrier fingers while the polishing bath itself removes the rear emitter. Due to the different etch rates of the liquid and the gas phase this process allows for etch depths of ~50 nm on the front side and several micrometers on the rear side [52]. As polishing processes are typically part of industrial PERC process flows the GEB approach reduces the number of additional process steps by one compared to conventional selective etch back techniques.

As selective emitter technologies provide improved overall J_{0e} values and thus higher efficiencies, three of the record efficiencies of Figure 1.3 were obtained using such emitters [18, 21, 25]. Four of the solar cells applied a homogeneous emitter [3, 19, 22–24], however, one of them was homogeneously etched back [3, 23]. Selective emitter processes currently have a market share below 5%, which is expected to increase to 15% in 2023 [2]. Although selective emitter technology will only play a minor role in industrial production for the years to come, it might become mandatory in order to achieve even higher PERC cell efficiencies.

2

Characterization techniques

This chapter describes the most important characterization techniques used for the measurements presented in this thesis. In particular these are current-voltage and internal quantum efficiency measurements of final PERC solar cells. In addition we use different methods to measure effective carrier lifetimes and the transfer length method to determine contact resistivities. The latter two methods require preparation of special test samples.

2.1 Current voltage characteristics

In this section, we discuss the current-voltage (IV) characteristics of solar cells. All IV measurements presented in this work are measured using a LOANA system by pv-tools [53]. In this tool, the solar cell is placed on a brass chuck contacting the rear side. Contact needles are placed on the front side busbars. A heating and cooling system inside the chuck keeps the temperature at a constant value of $T = 25\,°\text{C}$. In this setup the current can be measured applying different bias voltages and illumination levels.

2.1.1 Recombination characteristics

There are different recombination mechanisms in a solar solar cell. The corresponding voltage-dependent recombination current densities typically obey one diode equations and sum up to the total recombination current density

$$J_{\text{rec}} = \sum_i J_{0,i} \left[\exp\left(\frac{q \cdot V}{n_i \cdot kT} \right) - 1 \right], \tag{2.1}$$

where $J_{0,i}$ are the saturation current densities, n_i the ideality factors, q the elementary electric charge, k the Boltzmann factor and T the temperature. The ideality factor depends on the specific recombination mechanism. For band-to-band and

Shockley-Read-Hall (SRH) recombination in low-level injection the ideality factor equals one. In case of SRH recombination in high-level-injection and recombination in the space charge region one obtains $n = 2$. For Auger recombination the ideality factor is $n = 2/3$. The IV curves of the PERC solar cells presented in this work are well described by using an ideality of $n = 1$ over the whole relevant range of voltages. Therefore we neglect contributions with $n \neq 1$ in the following.

2.1.2 Illuminated IV characteristics

In a one-diode circuit model of a solar cell as shown in Figure 2.1, the total extracted current density $J(V)$ is the net sum of the photogenerated current density J_{gen}, the recombination current density J_{rec} and the current density J_{sh} caused by a low shunt resistance R_{sh} [54]:

$$J(V) = J_{\text{gen}} - J_{\text{rec}} - J_{\text{sh}} = J_{\text{gen}} - J_0 \left[\exp\left(\frac{q(V + R_{\text{s}} \cdot J)}{kT} \right) - 1 \right] - \frac{V + R_{\text{s}} \cdot J}{R_{\text{sh}}}. \quad (2.2)$$

Here, R_{s} is the series resistance as illustrated in Figure 2.1. Figure 2.2 shows an exemplary IV curve for a choice of typical PERC cell parameters: $J_{\text{gen}} = 40 \, \text{mA/cm}^2$, $J_0 = 250 \, \text{fA/cm}^2$, $R_{\text{s}} = 0.5 \, \Omega\text{cm}^2$ and $R_{\text{sh}} = 10000 \, \Omega\text{cm}^2$. Under short circuit conditions ($V = 0$) the current density becomes the short circuit current density $J(0) = J_{\text{sc}}$. Under open circuit conditions the current density is zero ($J(V_{\text{oc}}) = 0$) and the corresponding voltage is called the open circuit voltage V_{oc}. In our example of Figure 2.2 we obtain $V_{\text{oc}} = 662 \, \text{mV}$ and $J_{\text{sc}} \approx J_{\text{gen}} = 40 \, \text{mA/cm}^2$ due to the high shunt resistance. The output power density $P = J \cdot V$ can be calculated for all points (J,V) of the IV curve. The point where P becomes maximal is called the maximum power point $(J_{\text{mpp}}, V_{\text{mpp}})$. Using this point the fill factor is defined as

$$FF = \frac{V_{\text{mpp}} \cdot J_{\text{mpp}}}{V_{\text{oc}} \cdot J_{\text{sc}}}. \quad (2.3)$$
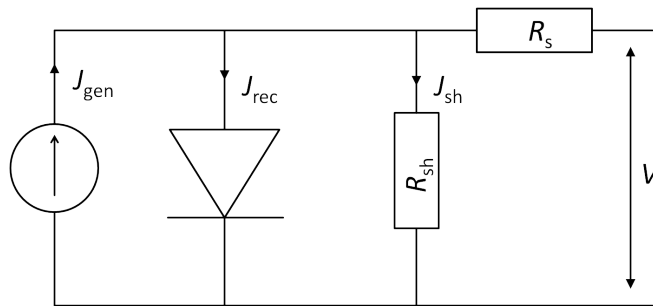

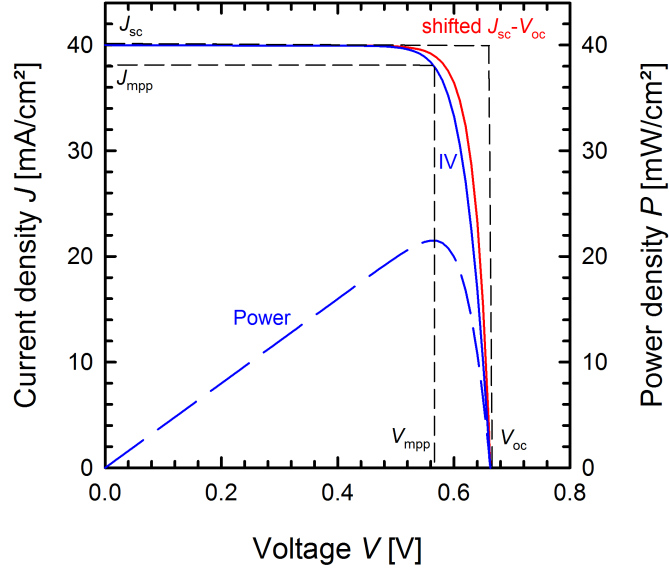**Figure 2.1:** One-diode circuit of a solar cell.

Figure 2.2: Calculated IV-curves for typical PERC cell parameters (see text). The solid blue line shows the IV curve under illumination and the red line the shifted $J_{sc}(V_{oc})$ curve. The difference between both curves stems from the series resistance contribution. The dashed blue line represents the power output density.

The FF is dependent on the series resistance, the shunt resistance and the specific recombination behavior of the solar cell. Using an empiric expression, the ideal fill factor FF_0 without shunt or series resistances can be calculated from the V_{oc} of a solar cell [55]:

$$FF_0 = \frac{v_{oc} - \ln(v_{oc} + 0.72)}{v_{oc} + 1} \quad \text{with} \quad v_{oc} = \frac{q \cdot V_{oc}}{kT}. \tag{2.4}$$

Also, Ref. [55] gives an approximate expression for the fill factor in the presence of a series resistance:

$$FF = FF_0 \left(1 - \frac{R_s \cdot J_{sc}}{V_{oc}}\right). \tag{2.5}$$

The conversion efficiency η of the solar cell can be calculated according to:

$$\eta = \frac{J_{mpp} \cdot V_{mpp}}{P_{in}} = \frac{J_{sc} \cdot V_{oc} \cdot FF}{P_{in}}, \tag{2.6}$$

where P_{in} is the power density of the incident light. For measurement of a solar cell under standard testing conditions (STC) an AM 1.5 G spectrum with an intensity of $P_{in} = 100\,\text{mW/cm}^2$ is used. This intensity is typically referred to as 1 sun. In order to maximize the efficiency η, the saturation current density J_0 and the series

resistance R_s need to be minimized, whereas the generated current density J_gen and the shunt resistance R_sh need to be maximized.

2.1.3 $J_\text{sc}(V_\text{oc})$ characteristics

In a $J_\text{sc}(V_\text{oc})$-measurement pairs of values of J_sc and V_oc are measured at different illumination intensities. Since under open circuit conditions there is no current flow, the V_oc values represent the voltage of the solar cell at a given illumination level without series resistance. Assigning these values to the J_sc of the same illumination level therefore results in the shape of a curve, that would be obtained by an IV measurement, if there was no series resistance present in the solar cell. The $J_\text{sc}(V_\text{oc})$ curve can be written as:

$$J_\text{sc}(V_\text{oc}) = J_0 \left[\exp\left(\frac{q \cdot V_\text{oc}}{kT} \right) - 1 \right] + \frac{V_\text{oc}}{R_\text{sh}}. \tag{2.7}$$

However, to make this curve directly comparable to the illuminated IV curve discussed in the previous section, we need to substract this curve from the measured J_sc @ 1 sun:

$$J_\text{sc}(V_\text{oc}), \text{shifted} = J_{sc,1\,\text{sun}} - J_\text{sc}(V_\text{oc}). \tag{2.8}$$

Figure 2.2 compares the shifted $J_\text{sc}(V_\text{oc})$ curve with the light IV curve of our exemplary solar cell and thus reveals the impact of the series resistance of $R_\text{s} = 0.5\,\Omega\text{cm}^2$. Both curves intersect at $V = V_\text{oc}$, where both measurements apply the same illumination level. In analogy to the fill factor FF of the IV curve, we can define a pseudo fill factor

$$pFF = \frac{\max\left(V_{\text{J}_\text{sc}(\text{V}_\text{oc}),\text{shifted}} \cdot J_{\text{J}_\text{sc}(\text{V}_\text{oc}),\text{shifted}} \right)}{V_\text{oc} \cdot J_\text{sc}}, \tag{2.9}$$

which would be the fill factor of a solar cell if there was no series resistance present. Using equation 2.5 we can calculate the series resistance R_s from the measured fill factor FF and pseudo fill factor pFF by setting $FF_0 = pFF$. If not stated otherwise all values of R_s in this work are measured using this method, which is called "the fill factor method".

2.2 Effective carrier lifetime measurements

In this section we present the different methods used in this work to measure the effective lifetime of excess carriers. The surface recombination velocities of passivation layers is often derived from these measurements and is also briefly discussed.

2.2.1 Photoconductance lifetime measurements

Photoconductance decay (PCD) measurements [56] are well-established as a technique to determine the effective lifetime of excess charge carriers in a semiconductor. During such a measurement the sample is placed on a coil and thus inductively couples to an oscillator circuit. The circuitry allows to measure the conductivity σ of the sample. The conductivity of a wafer with thickness W is given by

$$\sigma = q \int_0^W (n\,\mu_n + p\,\mu_p)\,\mathrm{d}z, \tag{2.10}$$

where n and p are the electron and hole concentrations and μ_n and μ_p the electron and hole mobilities. If the sample is now illuminated by a flash, which creates a photogenerated excess carrier density $\Delta n = \Delta p$, the circuitry will measure a corresponding increase in conductivity $\Delta \sigma$. By using an infrared filter for the flash, the photogeneration can be adjusted to be homogeneous within the wafer and equation 2.10 reduces to

$$\Delta n = \frac{\Delta \sigma}{qW(\mu_n + \mu_p)}. \tag{2.11}$$

The mobilities μ_n and μ_p are themselves functions of Δn [57], which is why equation 2.11 needs to be solved numerically.

The time dependency of Δn is given by the continuity equation

$$\frac{\partial \Delta n}{\partial t} = G(t) - U(t) + \frac{1}{q}\nabla J, \tag{2.12}$$

where G is the generation rate, U the recombination rate and J the current density. For a spatially uniform photogeneration and a sample of homogeneous passivation and material quality J becomes zero. Writing U in terms of a time constant

$$U = \frac{\Delta n}{\tau_{\mathrm{eff}}} \tag{2.13}$$

with the effective carrier liftime τ_{eff} allows to rewrite equation 2.12:

$$\tau_{\mathrm{eff}} = \frac{\Delta n}{G(t) - \frac{\partial \Delta n}{\partial t}}. \tag{2.14}$$

This equation offers two methods to measure τ_{eff}. The first one is the quasi-steady-state photoconductance (QSSPC) method, where a long flash is used to create a generation G and a corresponding excess carrier density Δn, that are constant in time. In this case equation 2.14 simplifies to

$$\tau_{\mathrm{eff}} = \frac{\Delta n}{G}. \tag{2.15}$$

However, this approach requires to calculate G from the known incident light intensity that is measured by a calibrated reference cell. This calculation requires knowledge of the absorption probability and, hence, the optics of the specific sample. The second possibility to measure τ_{eff} is the transient method, where an initial short flash is applied and the measurement is subsequently started in the dark, where $G(t) = 0$. Accordingly, Equation 2.14 becomes

$$\tau_{\text{eff}} = \frac{\Delta n}{-\frac{\partial \Delta n}{\partial t}}. \tag{2.16}$$

In contrast to a QSSPC measurement this method does not require any knowledge of the optics of the sample. However, the effective lifetime needs to be much larger than the duration of the flash $\tau_{\text{eff}} \gg t_{\text{flash}}$ to ensure that there are still measurable excess carriers at the time where $G(t) = 0$. This is the case for all samples measured in this work and therefore all PCD measurements apply the transient method.

2.2.2 Dynamic infrared lifetime mapping

In order to gain a spatially resolved measurement of the effective carrier lifetime the dynamic infrared lifetime mapping (dynILM) [58, 59] can be used. The dynILM measures the infrared emission of free charge carriers of a sample by an infrared camera (see Figure 2.3). An LED array illuminates the sample with pulses of

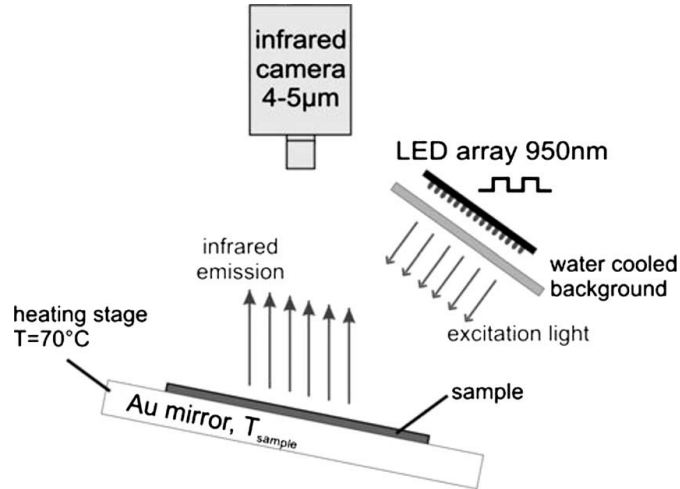**Figure 2.3:** Schematic drawing of the experimental setup of the PC-PLI measurement. The photoluminescence imaging is performed under the same excitation conditions as the PCD measurement. The image is taken from Ref. [60].

infrared excitation light. Images are taken at different times during a pulse period. With this method the effective carrier lifetime is obtained calibration-free from the

transient behaviour of the excess charge carriers. In order to increase the signal to noise ratio the sample is placed on an Al mirror at a temperature of $70\,°C$.

2.2.3 Photoconductance-calibrated photoluminescence lifetime imaging

The photoconductance-calibrated photoluminescence lifetime imaging (PC-PLI) [60, 61] is another possibility to obtain a spatially resolved image of the effective carrier lifetime. For this method the excitation light is provided by laser with a wavelength of $808\,nm$. The laser beam is widened and homogenized in order to illuminate the whole sample. The resulting band-to-band photoluminescence of the sample is detected by a Si CCD camera. A long-pass filter in front of the camera blocks reflected laser light and allows the camera to only detect the photoluminescence signal. The photoluminescence signal I_{PL} can be converted into the excess carrier density Δn using

$$I_{\mathrm{PL}} = C_{\mathrm{PL}}(\Delta n N_{\mathrm{dop}} + \Delta n^2), \tag{2.17}$$

where N_{dop} is the dopant concentration and C_{PL} is a constant that depends on the optical properties of the measurement setup and the sample [61]. In order to obtain C_{PL} the sample is placed on the coil of a PCD measurement setup for calibration (see Figure 2.4). A fit of equation 2.17 to the average photoluminescence signal at the coil area as a function of the PCD-measured excess charge carrier density Δn yields C_{PL}. The spatially resolved PC-PLI-measured Δn values can be used to calculate the effective lifetime according to equation 2.15.
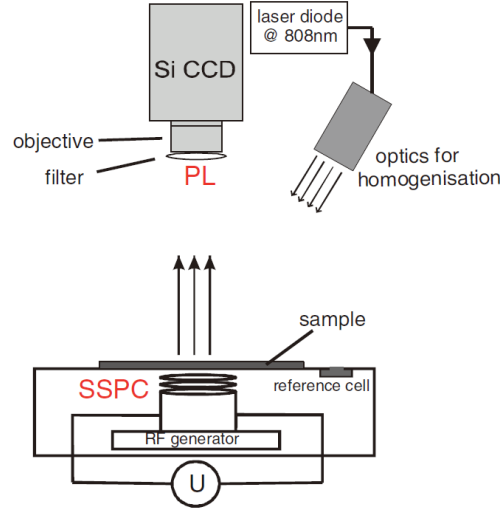

Figure 2.4: Schematic drawing of the experimental setup of the PC-PLI measurement. The photoluminescence imaging is performed under the same excitation conditions as the PCD measurement. The image is taken from Ref. [60].

2.2.4 Surface recombination velocities

In this thesis, we typically use effective lifetime measurements to asses the passivation quality of fully passivated lifetime test samples. The recombination rate per surface area can be defined similarly to equation 2.13:

$$U_{\mathrm{s}} = S_{\mathrm{pass}} \cdot \Delta n_{\mathrm{s}}, \tag{2.18}$$

where S_{pass} is the surface recombination velocity (SRV) and Δn_{s} the excess carrier concentration at the passivated surface. In general the excess charge carrier density is not equal in the bulk and at the surface $\Delta n \neq \Delta n_{\mathrm{s}}$ and diffusion needs to be taken into account. From a measured value τ_{eff} of a symmetrically passivated sample the SRV S_{pass} is therefore calculated according to [62]

$$S_{\mathrm{pass}} = \sqrt{D \left(\frac{1}{\tau_{\mathrm{eff}}} - \frac{1}{\tau_{\mathrm{b}}} \right)} \tan \left[\frac{W}{2} \sqrt{D \left(\frac{1}{\tau_{\mathrm{eff}}} - \frac{1}{\tau_{\mathrm{b}}} \right)} \right], \tag{2.19}$$

where τ_{b} is the wafer bulk lifetime and D the diffusion coefficient. In this work we use high quality float zone (FZ) material with very high bulk lifetimes τ_{b} for the lifetime test samples. This allows to neglect the terms $1/\tau_{\mathrm{b}}$ in equation 2.19. Due to this approximation the S_{pass} values reported in this work might also be considered as upper limits.

2.3 Quantum efficiency measurements

The LOANA tool used for the current voltage measurements can also be used for measurement of the quantum efficiency (QE) and the reflectance of solar cells. The (absolute) external quantum efficiency EQE_{abs} of a solar cell is defined as the ratio of the number of extracted electrons N_{e} to the number of incident photons N_{ph} of a wavelength λ under J_{sc} and 1 sun conditions:

$$EQE_{\mathrm{abs}}(\lambda) = \frac{N_{\mathrm{e}}}{N_{\mathrm{ph}}(\lambda)}\big|_{\mathrm{J_{sc,bias}}} = \frac{J_{\mathrm{sc,1sun}}(\lambda)}{q \cdot \Phi_{\mathrm{in,1sun}}(\lambda)}, \tag{2.20}$$

where $\Phi_{\mathrm{in,1sun}}(\lambda)$ is the flux of incident photons. Due to the potential nonlinear response of the solar cell to the incident light intensity, the absolute external quantum efficiency (EQE) cannot be measured directly using a monochromatic light source, e.g. a laser. Instead a bias light with AM 1.5 G spectrum is used and a chopped monochromatic light $\Phi_{\mathrm{signal}}(\lambda)$ with a small intensity compared to the bias light is superimposed. Filtering of this signal in the current domain results in a measurement of the differential EQE

$$EQE_{\mathrm{diff}}(\lambda) = \frac{\mathrm{d}J_{\mathrm{sc}}(\lambda)}{q \cdot \mathrm{d}\Phi_{\mathrm{signal}}(\lambda)}\big|_{\mathrm{J_{sc,bias}}}, \tag{2.21}$$

with a constant current contribution $J_{\text{sc,bias}}$ generated by the bias light. The differential EQE is measured at a wavelength of $1050\,\text{nm}$ during a sweep of the bias light intensity. From this measurement the absolute EQE at 1 sun can be calculated according to

$$EQE_{\text{abs}} = \frac{J_{\text{sc,1sun}}}{\int_0^{J_{\text{sc,1sun}}} \frac{1}{EQE_{\text{diff}}} \mathrm{d}J_{\text{sc,bias}}}. \tag{2.22}$$

The bias light intensity where EQE_{diff} coincides with EQE_{abs} @ 1 sun is then used as a good approximation for the measurement of a quasi-absolute EQE at the other wavelenghts. A typical value, where $EQE_{\text{diff}} = EQE_{\text{abs}}$ is about $\frac{1}{3}$ sun. More details on quantum efficiency measurements can be found in Ref. [63].

From the reflectance in the intermediate area between the Ag fingers of the front metalization $R(\lambda)$ the internal quantum efficiency (IQE) of a solar cell can be calculated according to

$$IQE(\lambda) = \frac{EQE_{\text{abs}}(\lambda)}{1 - R(\lambda)}. \tag{2.23}$$

Therefore the IQE describes the ratio of collected electrons under J_{sc} conditions to the number of incident photons that are not reflected. The IQE is a suitable measure for the electrical properties of a solar cell as optical properties only have a minor impact on it. Due to the reflectance of the fingers of the front metalization $R_{\text{met}}(\lambda)$ the reflectance in the intermediate area $R(\lambda)$ is typically not directly accessible by measurement of the solar cell with an integrating sphere. Instead the total reflection

$$R_{\text{meas}}(\lambda) = M_{\text{met}} \cdot R_{\text{met}}(\lambda) + (1 - M_{\text{met}}) \cdot R(\lambda) \tag{2.24}$$

is measured, where M_{met} is the fraction of the metalized area. The reflectance of the metalization $R_{\text{met}}(\lambda)$ can be determined in preceding measurements on fully metalized test structures. Using the approximation, that the anti reflective coating (ARC) allows for a minimum value of $R(\lambda) = 0$ for a specific wavelength λ, equation 2.24 can be used to calculate M_{met}. This value enables us to calculate $R(\lambda)$ for all wavelengths. This work only presents measured reflectance data that has been corrected by the metalization contribution in the described way and thus all curves have a minimum of $R(\lambda) = 0$.

We model the IQE using our in-house developed software SCAN, which is based on the analytical model for QE introduced by Brendel et al. [64]. This model considers the contributions to the IQE from different regions:

$$IQE = \sum_{i=e,scr,b} IQE_i, \tag{2.25}$$

where the index i denotes the emitter e, the space charge region *scr* and the bulk b, respectively. For the different contributions the model uses

$$IQE_i = \frac{A_i \eta_i}{1 - R},\tag{2.26}$$

where A_i is the absorption probability and η_i the collection efficiency of the respective region. The ratio of the absorption probability A_i to the total absorption probability A is given by the fraction of actively absorbed photons in region i to the total number of actively absorbed photons:

$$\frac{A_i}{A} = \frac{\int_{\text{region }i} g(z)\mathrm{d}z}{\int_{\text{total cell}} g(z)\mathrm{d}z},\tag{2.27}$$

where $g(z)$ is the generation profile. Similarly, the collection efficiencies η_i are the ratios of electrons collected from a region i in the short circuit current densities $j(g_i)$ to the absorbed photons in that region:

$$\eta_i = \frac{j(g_i)}{q \cdot \int_{\text{region }i} g(z)\mathrm{d}z}.\tag{2.28}$$

The artificial generation profiles $g_i(z)$ are equal to $g(z)$ in their respective region i and zero elsewhere. Inserting equation 2.27 and 2.28 into equation 2.26 yields

$$IQE_i = \frac{A}{1 - R} \cdot \frac{j(g_i)}{q \int_{\text{total cell}} g(z)\mathrm{d}z}.\tag{2.29}$$

In order to calculate IQE_i Ref. [64] first introduces an optical model that allows for calculation of the reflectance R and the generation profile $g(z)$. This optical model applies different "microscopic" quantities such as the reflectance at the front and rear surfaces, several light propagation angles, the absorption coefficient α or the thickness of each region. Since this work primarily focuses on the rear side of PERC solar cells, we are primarily interested in the internal reflectance at the rear R_{b} and the Lambertian fraction Λ_{b} that describes the diffuse part of the rear reflectance.

From the modeled $g_i(z)$ the transport model of Ref. [64] calculates the current density $j(g_i)$ by solving the diffusion equation for the excess minority charge carrier concentration. In case of the bulk the solution depends on the bulk diffusion length L_{b} and the SRV at the rear S_{rear} as a boundary condition.

A simultaneous fit of the modeled reflectance to the measured reflectance and the modeled IQE to the measured IQE yields – amongst others – a set of parameters R_{b}, Λ_{b}, S_{rear} and L_{b}. Since many combinations of S_{rear} and L_{b} typically result in a good fit, L_{b} is set to a fixed value that is estimated from $L_{\mathrm{b}} = \sqrt{D \cdot \tau_b}$ with diffusion coefficient D and a measurement of the bulk lifetime τ_{b} of the used wafer

material. A typical value for the bulk lifetime of the *p*-type Cz materials used in this work is 400–500 µs.

Differing to the bare model as presented in Ref. [64] our software SCAN applies minor modifications to account for parasitic absorption in the ARC and free carrier absorption. An exemplary measurement of the IQE and reflectance and the resulting fits of the model are shown in Figure 2.5. The measurements belong to a PERC solar cell with a record efficiency of 21.2%, which is analyzed in more detail in chapter 6.
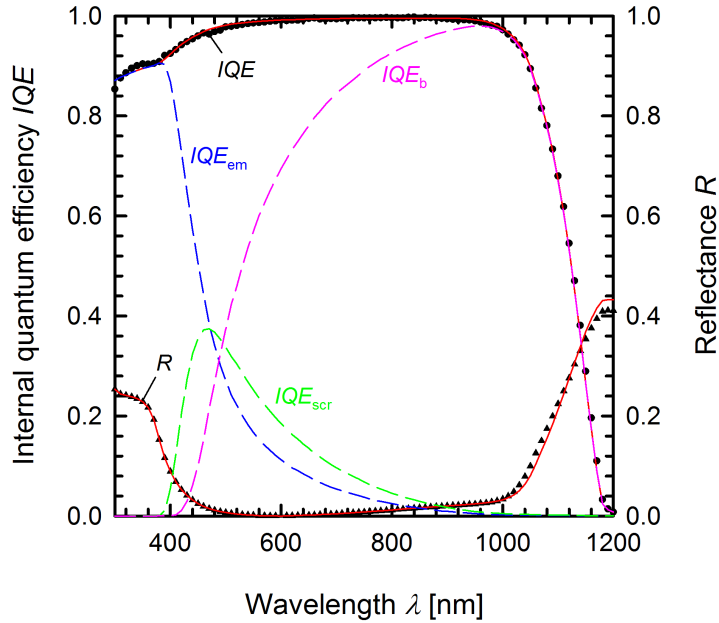

Figure 2.5: Measurements of the IQE (circles) and reflectance (triangles) of a 21.2%-efficient PERC solar cell. The red lines show a fit of the model of Ref. [64] to both quantities. The dashed lines indicate the modeled IQE-contributions from the emitter (blue), the space charge region (green) and the bulk (pink).

2.4 Transfer length method

The specific contact resistivity ρ_c of a metal-semiconductor interface can be measured using the transfer length method (TLM) [65, 66]. Figure 2.6a) schematically shows the structure of a TLM-sample with parallel metal contact stripes of width w and length l that are positioned at different distances d_x to each other. Applying the four point probe method, the resistance R between neighboring metal stripes
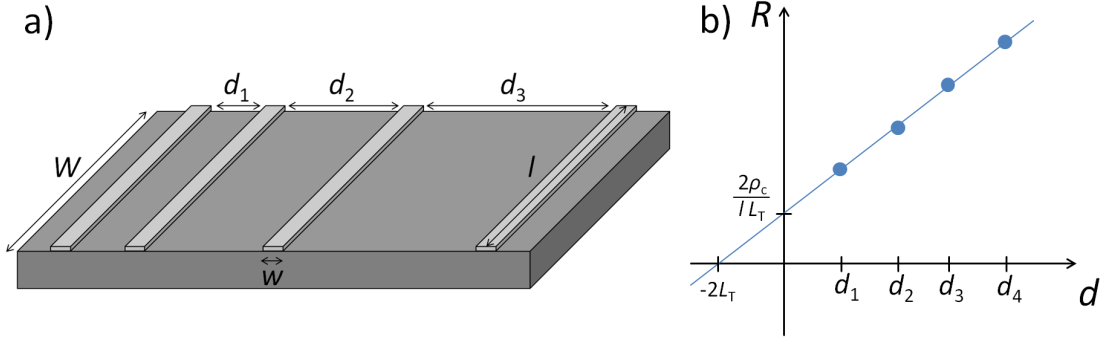
Figure 2.6: a) Schematic drawing of a TLM sample including the different geometrical parameters used in the evaluation. b) Virtual TLM measurement indicating the ordinate of the linear fit required for determination of the contact resistivity ρ_{c}.

can be measured in dependence of the distance d (see Figure 2.6b). A fit of the equation

$$R(d) = \frac{d \cdot R_{\text{sh}}}{l} + \frac{2\rho_{\text{c}}}{l \cdot L_{\text{T}}} \tag{2.30}$$

to the measurement allows for calculation of the sheet resistance R_{sh} from the slope R_{sh}/l of the resulting line. The contact resistivity ρ_{c} is given by the ordinate of equation 2.30, where $L_{\text{T}} = \sqrt{\rho_{\text{c}}/R_{\text{sh}}}$ is called the transfer length. The TLM assumes a thin conductive layer with sheet resistance R_{sh} to connect the metal stripes. For a wafer of finite thickness an advanced evaluation has recently been introduced [67], but is however not applied in this work. The TLM-sample geometry should meet the following requirements: $w > L_{\text{T}}$, $l \gg w$ and $\delta = W - l \ll W$ [66], where W is the width of the sample.

State-of-the-art PERC processing

This chapter describes parts of the preparative work and results required for the investigations of the following chapters. The reference PERC process is introduced along with a bifacial solar cell, called PERC+. In addition, the literature on the most important topics of this work is presented.

3.1 Reference PERC process

As a high quality and stable reference for most of the solar cell experiments presented in this work, we use a PERC process, which has been developed and continuously improved at ISFH [68]. This section summarizes the process flow and discusses the statistics of this reference PERC process.

3.1.1 Reference PERC process flow

The reference PERC process flow as shown in Figure 3.1a) uses pseudo-square 156x156 mm^2 2 Ωcm p-type boron-doped Czochralski (Cz) silicon wafers with an initial thickness of around 190 µm. After a cleaning procedure including a KOH-based saw damage etch, we deposit a protection layer on the rear side of the wafers. This allows for a subsequent single sided alkaline texturing process using a KOH chemistry with additives and resulting in randomly distributed pyramids of around 4 µm height on the wafer front side. The rear protection layer also serves as a diffusion barrier in the following POCl$_3$ diffusion performed in a quartz-tube furnace aiming at a phosphorus doping profile with a sheet resistance of 100 Ω/sq at the wafer front. The resulting phosphosilicate glass (PSG) and the protection layer are then removed by etching in HF. After an RCA clean we deposit a rear passivation layer stack consisting of atomic layer deposited (ALD) Al$_2$O$_3$ and a 200 nm thick plasma enhanced chemical vapor deposited (PECVD) SiN$_x$. The front side applies a PECVD-SiN$_x$ anti reflective coating (ARC) with a refractive index

of $n = 2.05$. Afterwards the dielectric rear passivation layer stack is locally ablated by laser contact opening (LCO) in order to form line shaped contact openings. Ag screen printing on the front side forms an H-patterned 5 busbar (BB) Ag finger grid. Applying a commercially available Al paste, we perform full-area screen printing resulting in an Al layer of $30\,\mu m$ thickness on the rear side. Both screen printing processes are followed by a drying step. The reference PERC process flow is concluded by a co-firing step in a conveyor belt furnace. The final PERC solar cell is shown in Figure 3.1b). Further details can be found in Ref. [24].
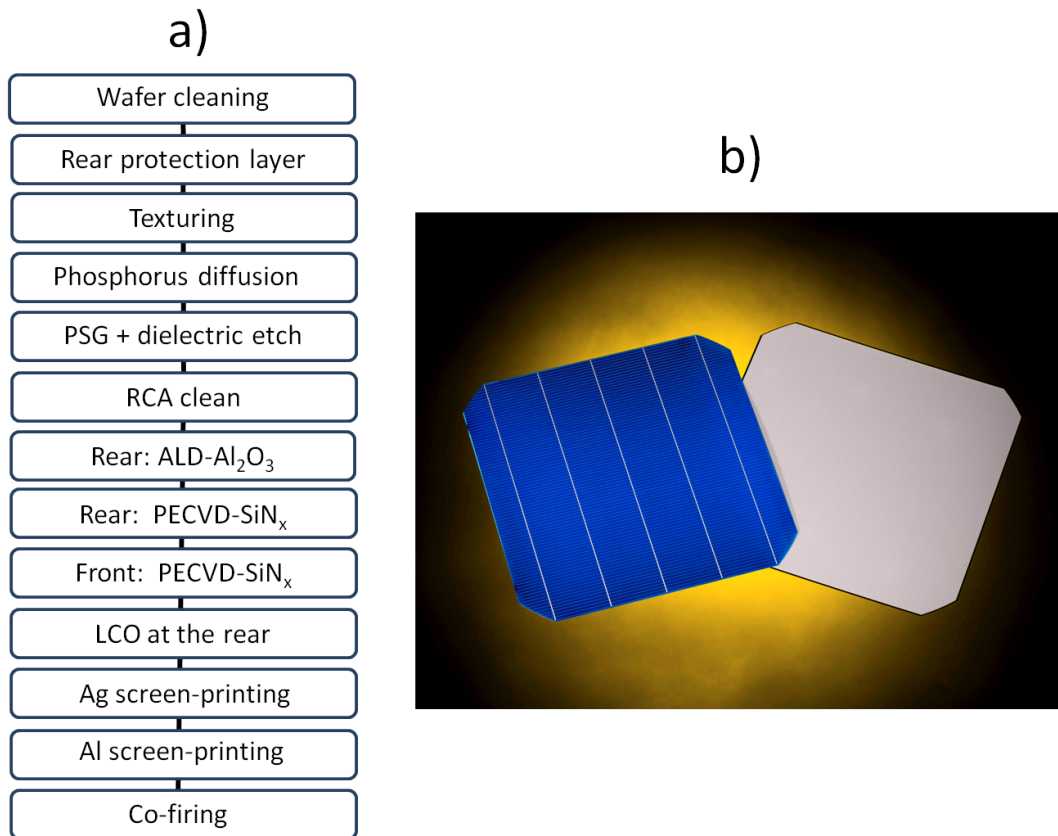
a)

- Wafer cleaning
- Rear protection layer
- Texturing
- Phosphorus diffusion
- PSG + dielectric etch
- RCA clean
- Rear: ALD-Al$_2$O$_3$
- Rear: PECVD-SiN$_x$
- Front: PECVD-SiN$_x$
- LCO at the rear
- Ag screen-printing
- Al screen-printing
- Co-firing

b)

Figure 3.1: The reference PERC process flow (a) and a photograph of the front and rear side of the resulting 5BB PERC solar cells (b).

As the best PERC cell efficiencies obtained at ISFH increased from 19.4% in 2011 [19] to 21.2% in 2014 [24](compare chapter 1), the efficiencies of the reference PERC cells of this work often differ between the various experiments presented in chapter 4 and 5. Accordingly, higher efficiencies generally correspond to later points in time. The process flow, however, remained similar and the individual processes have been optimized. The most important improvements during that time were:

- Application of a 5BB Ag finger grid layout with a busbar width of 0.5 mm instead of a 3BB layout with 1.3 mm wide busbars [24]. This leads to a decrease in total front side shadowing from 5.8% to 4.0%, while keeping the series resistance contribution from the finger grid small.

- Optimization of the fineline screen printing process towards narrower fingers and higher aspect ratios in order to further reduce the shadowing loss and resistance contribution [69, 70].

- Optimization of the phosphorus doping profile including lower phosphorus concentrations at the surface and thus leading to lower surface recombination. Also, improved Ag pastes allow to achieve low contact resistances even for low phosphorus surface concentrations.

- Application of new Al pastes that obtain a deeper or more homogeneous back surface field (BSF).

3.1.2 Statistics of the reference PERC process

In order to provide the reader with an assessment of the statistical relevance of the results presented in this work, we briefly discuss the statistics of our reference PERC process. Figure 3.2 shows a histogram of 77 reference PERC solar cells processed at ISFH.
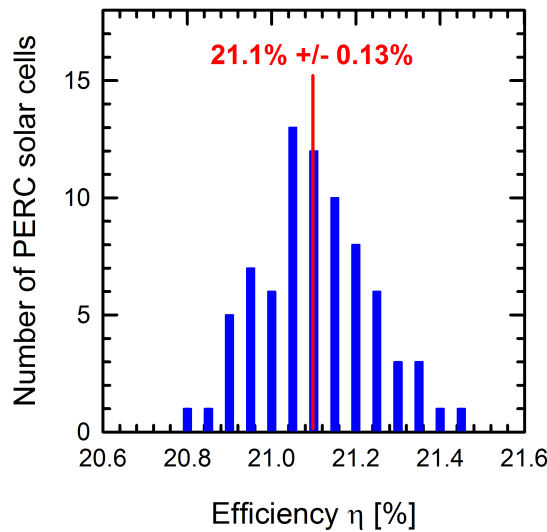

Figure 3.2: Histogram of the conversion efficiency of 77 reference PERC solar cells processed at ISFH. The average conversion efficiency is 21.1% with a standard deviation of $\pm 0.13\%$.

We obtain a normal distribution with an average efficiency of $\mu = 21.1\%$ and a standard deviation of $\sigma = 0.13\%$. We consider these values to accurately describe our reference process for the discussion of this section. In daily solar cell development

we often include process variations in split groups of $n = 5$–10 PERC solar cells and afterwards possibly measure a higher average efficiency $\bar{\eta}$ for this split group. Assuming that the modified solar cells are also normally distributed and posses the same standard deviation $\sigma = 0.13\%$, according to the central limit theorem [71], the arithmetic means $\bar{\eta}$ of samples with size n are again normally distributed with a standard deviation of

$$s = \frac{\sigma}{\sqrt{n}}, \tag{3.1}$$

which is now called the standard error. However, after measurement of a specific value for $\bar{\eta}$ the question arises: For a given confidence level, are the solar cells applying the new process more efficient compared to the reference process? In order to answer that question we carry out a (one tailed, one sample) Z-test [72], which includes calculation of the z-score[1]

$$z = \frac{\bar{\eta} - \mu}{s}. \tag{3.2}$$

This score can be thought of as "the difference of the corresponding means in units of the standard error". It can now be compared with the integral of the standard normal distribution (i.e. with a mean of 0 and a standard deviation of 1) in order to decide if the new process obtains higher efficiencies. For example 80% of the values of the standard normal distribution are smaller than 0.842, whereas 90% are smaller than 1.282 and 95% are smaller than 1.645. If the z-score is larger than 1.282 the new solar cell process can be considered to be more efficient with a confidence level of 90%. Table 3.1 summarizes exemplary confidence levels assuming different measured increments in conversion efficiency $\bar{\eta} - \mu$ and sample sizes n.

Please note, that in practice the standard deviation of the new process is not known. It can, however, be estimated from the (small) sample:

$$\sigma = \sqrt{\frac{1}{n-1} \sum_{i=1}^{n} (\eta_i - \bar{\eta})}, \tag{3.3}$$

---

[1]For a measured apparent increase in efficiency $|\bar{\eta} - \mu|$ this question might be answered positively at a confidence level of e.g. $p = 95\%$, which means that a similar sampling of the reference process would result in equally high (or higher) values of $|\bar{\eta} - \mu|$ with a probability of $1 - p = 5\%$. However, one might instead ask the question if the new process is different (worse or better) compared to the reference and thus carry out a two tailed Z-test. Outcomes with a result equally or more extreme ($\pm|\bar{\eta} - \mu|$) are twice as frequent (10%) due to the symmetry of the normal distribution. Thus, using the same example, the new process would be considered to be different from the reference at a confidence level of only 90%, leading to the counterintuitive situation that a measurement can show significantly *higher* efficiencies, without showing significantly *different* efficiencies. In solar cell development we are interested in higher efficiencies and typically disregard measurements with $\bar{\eta} < \mu$. We therefore choose to apply the one tailed test.

Table 3.1: Confidence levels for an increase in efficiency calculated for different exemplary values of $\bar{\eta} - \mu$ and sample sizes n.

sample size n	$\bar{\eta}$-μ [%]			
	0.05	0.10	0.15	0.20
5	72.845%	88.806%	96.595%	99.250%
10	80.511%	95.729%	99.506%	99.971%
15	85.390%	98.242%	99.921%	99.999%

where η_i are the efficiencies of the separate solar cells of one sample. This estimation requires to carry out a Student's t-test [73] instead of a Z-test. Similar to equation 3.2 the t-score is

$$t = \frac{\bar{\eta} - \mu}{\sigma/\sqrt{n}},\tag{3.4}$$

which can now be compared with the values of the t-distribution with $n - 1$ degrees of freedom. For example, in the t-distribution with 4 degrees of freedom (which corresponds to a sample size of 5) 80% of the values are smaller than 0.941 (compared to 0.842 for the standard normal distribution). For $n \to \infty$ the t-distribution is equal to the standard normal distribution. Hence, the difference between Z-test and t-test vanishes for large sample sizes.

The mean value and standard deviation of the reference process are often not as precisely known as for the high statistics evaluation as shown in Figure 3.2. Instead they are calculated from a comparably small sample, too. In this case a two sample t-test needs to be applied. For the two sample test the t-score becomes

$$t_{2\text{sample}} = \frac{\bar{\eta}_1 - \bar{\eta}_2}{\sigma_{2\text{sample}} \cdot \sqrt{\frac{1}{n_1} + \frac{1}{n_2}}},\tag{3.5}$$

where $\bar{\eta}_1$ and $\bar{\eta}_2$ are the average efficiencies and n_1 and n_2 the sample sizes of sample 1 and 2, respectively.

$$\sigma_{2\text{sample}} = \sqrt{\frac{(n_1 - 1)\sigma_1^2 + (n_2 - 1)\sigma_2^2}{n_1 + n_2 - 2}}\tag{3.6}$$

is an estimator of the common standard deviation of the two samples with their respective standard deviations σ_1 and σ_2. The two sample t-test yields reliable results, if the variances of the two populations (i.e. the two solar cell processes) are equal. For the general case, that the variances may differ, there are more elaborate methods like Welch's t-test [74].

t-tests are occasionally performed during the solar cell development connected with this work. However, they require calculation of the standard deviation for the

specific samples and are not explicitly shown for the various experiments presented in this thesis. For a general but slightly optimistic assessment of the statistical significance the reader may refer to Table 3.1. We often apply split groups with a sample size of $n = 5$. According to Table 3.1 a measured difference in efficiency of $\bar{\eta} - \mu = 0.10\%$ thus would indicate an improved process at a confidence level of 88%. Larger increments in efficiency improve the statistical significance. In this thesis, split groups with a difference of $\leq 0.1\%$ are generally considered to be comparable, whereas differences of $>0.1\%$ are considered to be significant.

3.2 Design of an Al-finger grid for bifacial PERC+ solar cells

Typical production processes for industrial PERC cells include full-area aluminum screen printing on the rear side even though the aluminum paste contacts the silicon wafer only at the areas where the LCO process removes the rear passivation layer. Due to the full-area rear Al layer, the resulting PERC cells only absorb light entering the solar cell from the front side and hence are not suited for bifacial module applications. The so-called PERC+ solar cell concept features screen printing of an Al finger grid aligned to the LCO line contacts at the wafer rear side [75], enabling bifaciality (see Figure 3.3). The Al finger grid design of the PERC+ cells reduces the Al paste consumption by 90% when compared with full-area Al layers. Also, this approach reduces the wafer bow measured as the maximal distance of the solar cell to a flat surface.

In order to optimize the layout of the front and rear grid of PERC+ solar cells simultaneously, we adapt an existing model for grid optimization of monofacial solar cells [46] for bifaciality. From Ref. [46] we read that the total shadowing of an H-patterned metalization grid is

$$p_s = \frac{s \cdot w_{\text{buc}}(1 - t_b) + w_f(l_f + w_{\text{buc}}t_b)(1 - t_f)}{s \cdot a}, \tag{3.7}$$

where s is the finger pitch, w_f the finger width and l_f the finger length. w_{buc} is half the busbar width and $a = l_f + w_{\text{buc}}$ the length of a unit cell (see Figure 3.4). To account for possible reflections of light at the metalization into the solar cell, the equation includes the effective transparency of fingers t_f and busbars t_b. Since our PERC+ solar cell features an Ag finger grid on the front and an Al finger grid on the rear side, we calculate two separate shadowings ($p_{s,\text{Ag}}$ and $p_{s,\text{Al}}$) with their respective geometrical parameters and introduce an effective total shadowing

$$p_{s,\text{eff}} = p_{s,\text{Ag}} \cdot I_{\text{Ag}} + p_{s,\text{Al}} \cdot I_{\text{Al}} \quad \text{with} \quad I_{\text{Ag}} + I_{\text{Al}} = 1, \tag{3.8}$$

where I_{Ag} and I_{Al} are the percentages of incident light intensity from the front and the rear, respectively. Equation 3.8 implies that the reflectances of the front and rear ARC are similar. If they are not, I_{Ag} and I_{Al} can be replaced by effective values.
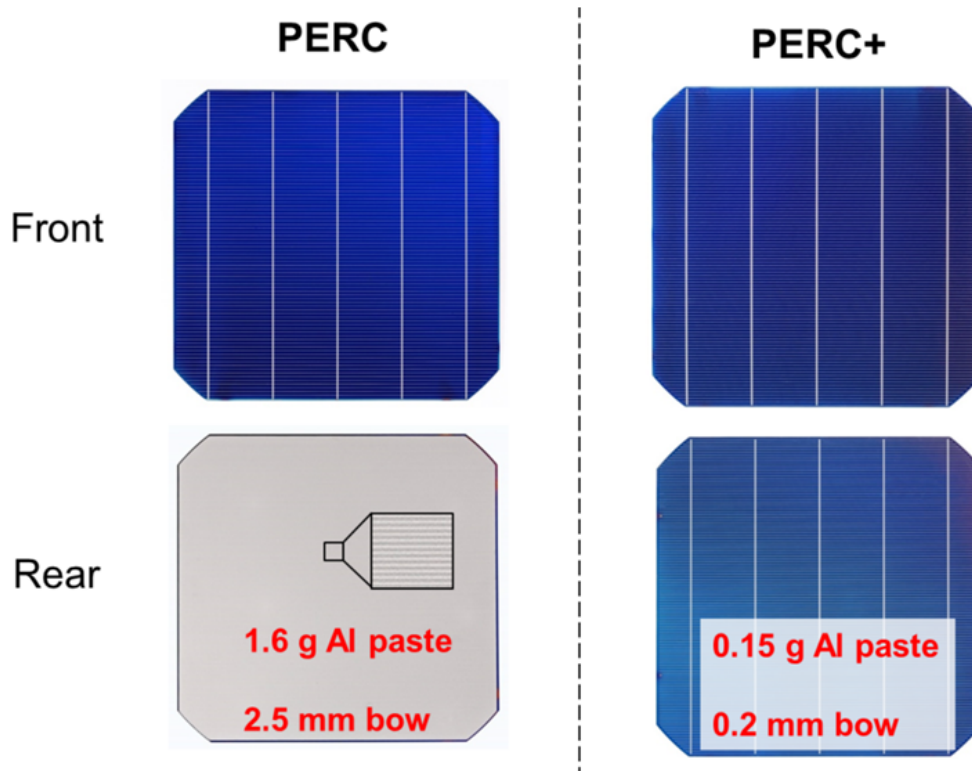
Figure 3.3: Photographs of the front and rear side of a PERC and a PERC+ solar cell. Both solar cells follow the same process flow described in section 3.1.1. The PERC+ cell, however, features an Al finger grid on the rear side instead of a closed Al layer, enabling bifaciality, lower Al paste consumption and a smaller wafer bow. The image is taken from Ref. [76].
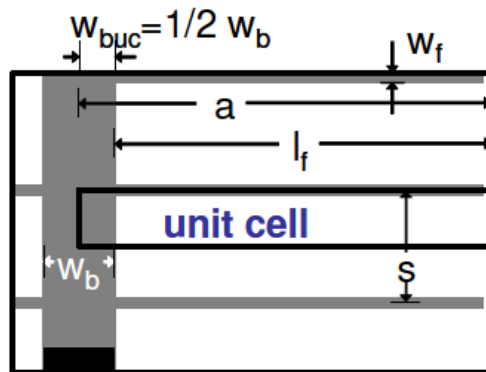

Figure 3.4: Illustration of a unit cell of an H-patterned metalization grid and the corresponding geometrical parameters. The image is taken from Ref. [46].

29

We calculate the (area-weighted) resistance contributions from the front side using the following three expressions all taken from Ref. [46]. The contribution from lateral currents through the emitter is

$$R_{\text{em}} = \frac{1}{12} R_{\text{sh}} \frac{s - w_{\text{f}}}{l_{\text{f}}} a s, \tag{3.9}$$

where R_{sh} is the emitter sheet resistance. The contact resistance contribution from the Ag fingers to the emitter is calculated according to

$$R_{\text{c,Ag}} = \frac{\sqrt{R_{\text{sh}} \rho_{\text{c,Ag}}}}{l_{\text{f}}} \coth \left(\frac{w_{\text{f}}}{2} \sqrt{\frac{R_{\text{sh}}}{\rho_{\text{c,Ag}}}} \right) a \frac{s}{2} \tag{3.10}$$

with $\rho_{\text{c,Ag}}$ as the corresponding contact resistivity. Finally, the resistance of the Ag-fingers is

$$R_{\text{f,Ag}} = \frac{1}{3} \rho_{\text{f}} \frac{l_{\text{f}}}{A_{\text{f}}} a s \tag{3.11}$$

with the specific resistivity ρ_{f} and the cross sectional area A_{f} of the Ag-fingers. In order to calculate the resistance contribution of the rear Al-fingers $R_{\text{f,Al}}$, we use the same equation 3.11 with analogous geometry and material parameters. The contact resistance of the Al contacts to the wafer is calculated according to

$$R_{\text{c,Al}} = \frac{\rho_{\text{c,Al}}}{f}, \tag{3.12}$$

where f is the fraction of the metalized area on the rear side and $\rho_{\text{c,Al}}$ the contact resistivity (see section 5.1 for determination of this parameter). We complete our analytical description by calculating the resistance contribution from the wafer bulk for line shaped rear contacts according to an equation by Saint-Cast [77]:

$$R_{\text{b}} = \frac{a_{\text{c}}}{2} \rho \left(37f - 2 - \frac{0.3}{f} \right) + \frac{2.82 (2W/a_{\text{c}})^{0.88} f^{0.64}}{\tanh \left(2.82 (2W/a_{\text{c}})^{0.88} f^{0.64} \right)} \frac{a_{\text{c}}^2 \rho}{12W} \cdot \left(\frac{1}{f} - 1 \right)^2 + W \rho, \tag{3.13}$$

where a_{c} is the width of the rear contact lines, W the thickness of the wafer bulk and ρ the specific resistivity of the wafer material. As shown in section 5.1 the values calculated according to equation 3.13 fit well to simulated bulk resistance contributions for a large interval of the metalization fraction f. Neglecting other series resistance contributions like, e.g., the busbar line resistance, the total series resistance R_{s} is now the sum of the individual series resistances:

$$R_{\text{s}} = R_{\text{f,Ag}} + R_{\text{c,Ag}} + R_{\text{em}} + R_{\text{b}} + R_{\text{c,Al}} + R_{\text{f,Al}}. \tag{3.14}$$

Using the derived effective total shadowing loss and the total series resistance, we can now calculate a "relative power output" p, which is defined as the power output

of a solar cell P_{mpp} divided by the hypothetical power output $P_{\mathrm{mpp,max}}$, when there would be no optical or electrical losses present [46]:

$$p = \frac{P_{\mathrm{mpp}}}{P_{\mathrm{mpp,max}}} = 1 - p_{\mathrm{s,eff}} - (1 - p_{\mathrm{s,eff}})^2 R_{\mathrm{s}} \frac{J_{\mathrm{mpp,max}}}{V_{\mathrm{mpp,max}}}. \qquad (3.15)$$

Here, $J_{\mathrm{mpp,max}}$ denotes the current density and $V_{\mathrm{mpp,max}}$ the voltage for the ideal case:

$$P_{\mathrm{mpp,max}} = J_{\mathrm{mpp,max}} V_{\mathrm{mpp,max}}. \qquad (3.16)$$

For given values of the incident intensities I_{Ag} and I_{Al}, both finger pitches can now be varied in order to maximize p. Applying a 5 busbar layout for the rear and the front side, we use this method to design the screens for both screen printing processes of the PERC+ process flow. For a set of typical geometrical parameters and resistivities, we exemplary calculate the optimal number of front Ag fingers and rear Al fingers in dependence of the relative rear side illumination $I_{\mathrm{Al}}/I_{\mathrm{Ag}}$ as shown in Figure 3.5. In case of no rear side illumination $I_{\mathrm{Al}}/I_{\mathrm{Ag}} = 0$ the described model yields the same result for the optimal number of front Ag fingers as the model for monofacial solar cells in Ref. [46].
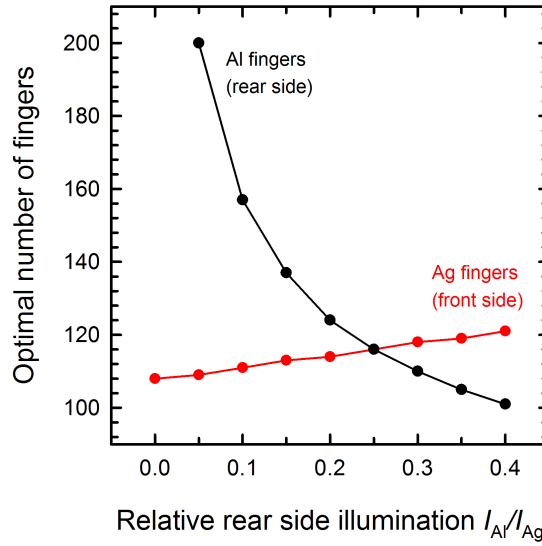

Figure 3.5: Optimal calculated number of front Ag fingers and rear Al fingers for different relative rear side illumination levels $I_{\mathrm{Al}}/I_{\mathrm{Ag}}$ and a typical set of input parameters. The lines are a guide to the eye.

The experimental PERC+ solar cells related to this work achieve rear side efficiencies of up to 16.7%, whereas the front side efficiencies remain comparable to monofacial PERC solar cells with values of up to 21.5% [78]. Also, the use of Al fingers for PERC+ cells increases the depth of the local p^+-doped Al back surface

fields (BSF) compared with full-area Al layers applied to PERC cells [75]. The physical root cause for the deeper BSFs is analyzed in section 5.2.

3.3 Polishing and cleaning of the rear side

In case of full-area Al-BSF solar cells the process steps affecting the rear side are: double sided texturing, double sided diffusion, single sided wet chemical removal of the rear emitter (edge isolation), full-area Al screen printing and firing. During the firing the aluminum in the Al paste melts, dissolves silicon from the wafer surface and subsequently forms the Al-BSF during cooldown. For a PERC cell, however, the contact including the Al-BSF is only formed locally. The remaining surface is covered by a dielectric passivation layer. A transfer of the same process sequence as described above to a PERC process flow would result in a rough textured surface in the passivated area. Hence, it might be beneficial to replace the edge isolation by a wet chemical polishing process with enhanced etch rate to remove the rear emitter and simultaneously reduce the surface roughness. Another characteristic of a PERC process flow is the requirement to sufficiently clean the wafer rear surface prior to passivation to allow for a low surface recombination.

Since chapter 4 focuses on polishing and cleaning of the rear side of industrial-type PERC solar cells, this section briefly presents the polishing tool used in this work. It also gives an overview on previous literature dealing with the impact of surface roughness and different cleans on the rear side of PERC solar cells.

3.3.1 Single sided wet chemical polishing tool

We use the RENA InPilot tool [79] for the rear side polishing process. In this tool, wafers are transported inline on rollers similar to the wet chemical junction isolation process in order to allow a single sided etching of the wafer rear side as shown in Figure 3.6. The polishing bath is based on HNO_3 and HF chemistry. Different polishing removals can be applied by adjusting the rotation velocity of the rollers and thus the process time. The wet polishing chemistry forms a gas phase which can lead to an etching of the front wafer surface, however with much lower etch rates compared to the rear polishing etch rates. The reactive gas phase may also create porous silicon on the front side of the wafer. Therefore the polishing process should be followed by a cleaning with sufficient etching capability to remove the porous silicon.
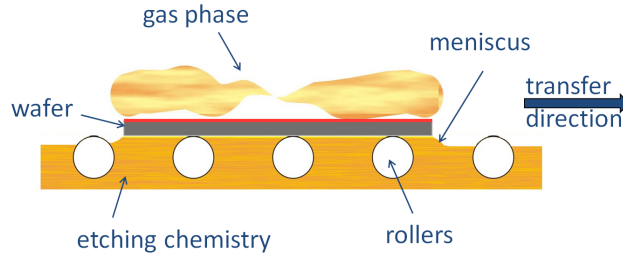
Figure 3.6: Schematic drawing of the rear polishing process. The phosphorus emitter on the front side of the wafer is displayed in red color.

3.3.2 Previous work on surface roughness

As demonstrated in Ref. [80,81], the surface recombination velocity (SRV) increases for rougher silicon surfaces. This is due to several effects. Assuming a fully textured surface with (111) orientation, the surface area increases by a factor of 1.73 compared to a planar (100) surface. Secondly, there is a significantly higher amount of dangling bonds at (111) surfaces compared to (100) surfaces [82]. Finally it seems that additional recombination arises from edges and ridges [83] and potential stress within the passivation layer [84]. Several years ago, the impact of the silicon surface orientation on the surface passivation quality of POCl$_3$ diffused surfaces passivated with SiN$_x$ and SiO$_2$ layers was studied for the front surfaces of silicon solar cells [85–88]. These studies revealed increasing SRVs for planar (111) and textured (111) surfaces, when compared to planar (100) surfaces. For example, Jin et al. [87] reported values for thermally oxidized wafers of 10–700 cm/s for textured surfaces and 2–60 cm/s for planar (100) surfaces, where the large spread results from different thermal treatments applied after oxidization. The SRVs for planar (111) surfaces are reported to be in between those of planar (100) and textured surfaces. With respect to optical properties, it is known that smoother rear sides increase the internal reflectance and reduce the fraction of diffuse scattered light [89].

Schwab et al. [90] demonstrated the influence of the rear surface roughness on the recombination and optical parameters of PERC solar cells with physical vapor deposited (PVD) aluminum rear contacts and thermal oxide as rear surface passivation. Here it was shown that the effective SRV at the rear increases from 200 cm/s to 950 cm/s when moving from planar to textured surfaces. The internal reflection at the rear R_b was found to decrease from 93.3% for planar surfaces to 90.4% for textured ones. Correspondingly, the PERC cell efficiency decreased from 19.4% for planar to 18.4% for textured rear surfaces. Using a HNO$_3$ and HF solution with non-organic additives as polishing bath Dastgheib-Shirazi et al. [91] showed that the SRV of 2 Ωcm p-type float zone (FZ) wafers fully passivated with Al$_2$O$_3$ decreases from approximately 10 cm/s for textured surfaces to 2 cm/s for

polished surfaces with a removal of about 5 μm. However, this work does not report IV parameters of PERC solar cells.

In section 4.1 we investigate the impact of surface roughness on screen printed PERC solar cells as well as on lifetime test samples. Based on the results of the surface roughness analysis, we develop a short PERC process flow including a polishing step, which results in efficiencies comparable to the reference PERC process (see section 4.2).

3.3.3 Previous work on cleans prior to passivation

As described in section 3.1.1, we use a high quality RCA clean [92] prior to passivation as a reference process. The RCA consists of four process steps: Standard Clean 1 (SC1), HF-Dip, Standard Clean 2 (SC2), HF-Dip. The SC1 is an aqueous solution of ammonium hydroxide (NH_4OH) and hydrogen peroxide (H_2O_2) and removes organic residues and particles. The following SC2 is an aqueous solution of hydrochloric acid (HCl) and H_2O_2 and removes remaining metallic contaminants. In industry the RCA clean is costly due to its expensive chemicals and process length. Therefore different groups searched for alternative cleans.

Vermang et al. [93] evaluated cleanings like SPM, HF, APM – including a sulphuric acid-hydrogen peroxide mixture (SPM) and an ammonia peroxide mixture (APM) – that result in hydrophilic surfaces as well as cleanings like SPM, HF that result in hydrophobic surfaces prior to atomic layer deposition of Al_2O_3 on lifetime test samples. Whereas both exhibited similar effective surface recombination velocities of around 100 cm/s using p-type Cz material, they favoured the hydrophilic cleanings due to its higher thermal stability and homogeneity. Other previous work [94] also reported good surface passivation with SPM, HF/HCl, HNO_3 cleans which form a hydrophilic surface and showed lifetimes around 300 μs using p-type Cz wafers and PERC cell efficiencies of up to 19.4%. More recent work [95] suggests, that with lifetimes around 1 ms, cleanings resulting in hydrophobic surfaces are superior in terms of cleaning efficiency. Using a Seluris® C solution, which aims at combining SC1 and SC2 in one step, they applied a Seluris, HF cleaning sequence prior to ALD-Al_2O_3 passivation to achieve an effective lifetime of 800 μs with p-type Cz material and PERC cell efficiencies of 19.9%. The reference applying a high quality SPM, HF/HCl clean yielded comparable values.

Ozone based cleans are known from different applications in microelectronics [96, 97]. Moldovan et al. [98] first applied an HF/HCl/O_3 clean to solar cell precursors and reported cleaning efficiencies of at least 98.7% for iron and 99.8% for copper. By varying the ozone concentration the increase in emitter sheet resistance during the cleaning process could be adjusted to values between 12 Ω/sq and 35 Ω/sq as measured on samples with a 90 Ω/sq emitter after diffusion.

In section 4.3 we evaluate even shorter cleaning sequences, e.g. HF/O_3 in a single step, on fully-processed PERC solar cells.

3.4 Formation of screen printed local Al contacts

Chapter 5 focuses on the analysis of screen printed local Al contacts formed by LCO. This section describes the contact formation during firing and presents previous work on this topic.

3.4.1 The alloying process at the Al-Si interface

During the firing process of full-area Al-BSF solar cells the aluminum in the Al paste starts to melt at temperatures around 660 °C [99]. The liquid Al then starts to dissolve Si from the solid Si surface. As the temperature further increases the ongoing dissolution of Si increases the Si concentration in the Al paste until it reaches the solubility of Si in Al. For a typical peak firing temperature of PERC cells of 800 °C this solubility is around 27% [99]. During cool down the solubility of Si in Al decreases again until it reaches the eutectic point at 577 °C with a Si concentration of 12% [99]. At this point the Al-Si melt solidifies. The decrease in solubility leads to oversaturation and a re-crystallization of Si from the melt which occurs mainly at the interface to the solid Si. This epitaxial growth of Si at the interface incorporates Al according to its solid solubility in Si and thus forms an Al-doped Si layer – the aluminum back surface field (Al-BSF). Since the Si concentration in the Al-Si melt cannot drop below the eutectic concentration of 12%, some of the Si dissolved from the wafer remains in the Al paste.

3.4.2 Previous work on local rear contacts

In case of PERC the Al paste only contacts the Si wafer at the LCO areas and the alloying process only takes place locally. The dissolution process therefore creates trenches in the Si wafer. Also, the Si concentration only locally reaches the solubility limit in the Al melt. The laterally inhomogeneous Si concentration leads to a transport of Si away from the contact area due to diffusion [100]. This again causes an effective reduction of the near-contact Si concentration and thus to an enhanced dissolution and reduced recrystallization process, which also reduces the depth of the resulting local Al-BSF.

Müller et al. [101] demonstrated by carrier lifetime measurements of test wafers that an increasing Al-BSF depth $W_{\mathrm{p^+}}$ reduces the effective surface recombination velocity (SRV) at a local Al contact S_{cont}. The same author then developed an analytical model to calculate the Al-BSF depth $W_{\mathrm{p^+}}$ of the local Al contacts of PERC cells in dependence of several process parameters [102]. Since this model is used in the analysis of the measurements of this work (see section 5.2), it is described in detail in the following.

The model can be used to describe a rectangular shaped contact with base area A, final contact width after firing a and final height h as shown in Figure 3.7. To account for the fact that only a limited volume of the Al paste layer with thickness d contributes in the alloying process with the silicon, the model introduces a diffusion
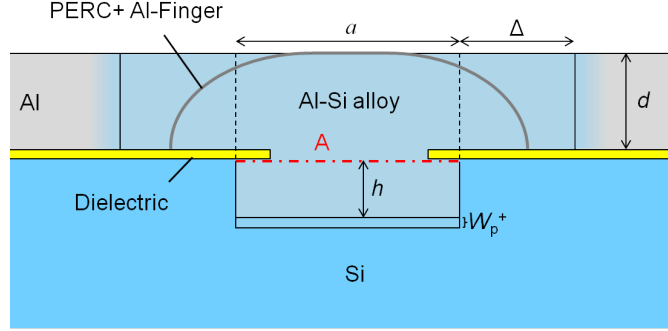
Figure 3.7: Schematic drawing of the rectangular contact geometry as used throughout this work. The sketch shows the final contact width after firing a, the contact height h, the thickness of the screen printed Al layer d and the depth $W_{\mathrm{p+}}$ of the Al-BSF. It also indicates the diffusion length Δ of Si in Al as used by the model of Müller et al. and the confinement of the Si diffusion in case of screen printed PERC+ Al-fingers. The red dotted line indicates the contact area A, which is orthogonal to the plane of projection.

length Δ. The resulting rectangle with edge lengths $a + 2\Delta$ and d defines a volume of Al with homogeneous silicon concentration.

The analytical description by Müller et al. [102] starts with an expression for the maximal depth $W_{\mathrm{p+}}$ of the Al-BSF as stated in Ref. [103]:

$$W_{\mathrm{p+}} = \frac{m_{\mathrm{Al}}}{A \rho_{\mathrm{Si}}} \left[\frac{c_{\mathrm{Si}}(t_{\mathrm{firing}})}{1 - c_{\mathrm{Si}}(t_{\mathrm{firing}})} - \frac{E}{1 - E} \right]. \tag{3.17}$$

Here, m_{Al} is the mass of the Al participating in the alloying process, ρ_{Si} the density of solid silicon, $E = 12\%$ the eutectic concentration and $c_{\mathrm{Si}}(t_{\mathrm{firing}})$ the silicon concentration in the Al-Si melt right before epitaxial regrowth. Since contact formation starts with the melting of Al at $660\,°\mathrm{C}$ and ends with solidification at $577\,°\mathrm{C}$, t_{firing} describes the time between these points. During this time the temperature T_{peak} is assumed to be constant. The analytical description is completed by the following two expressions [102]. The function

$$c_{\mathrm{Si}}(t) = F \left(1 - e^{-\frac{A}{m_{\mathrm{Al}}} \frac{\rho_{\mathrm{Si}} v_{\mathrm{diss}}}{F} t} \right) \tag{3.18}$$

describes an exponentially saturating silicon concentration towards the equilibrium concentration F at the temperature T_{peak}. $v_{\mathrm{diss}} = {}^{dh}\!/_{dt}$ represents the velocity of Si dissolution at the time $t = 0$. Finally, geometric considerations lead to

$$\frac{m_{\mathrm{Al}}}{A} = d \left(1 + \frac{2\Delta}{a} \right) \rho_{\mathrm{Al}}^{*} \tag{3.19}$$

with the effective aluminum density ρ^*_{Al} in the screen printed layer. By setting ρ^*_{Al} to 74% of the density of solid aluminum, we account for the non-compact screen printed layer and assume a dense sphere packing.

A variation of the contact line width a of PERC solar cells and measurement of the resulting BSF depths W_{p+} now allows to gain information about Δ and v_{diss} as the only two fit parameters in the model. Please note that Δ is a control parameter used to adjust the effective amount of Al paste participating in the alloying and recrystallization process. It must not be confused with the maximum spread of Si.

The model predicts that the Al-BSF depth increases with higher Si concentrations in the molten Al paste adjacent to the LCO area during furnace firing. Therefore different approaches to increase the near-contact Si concentration and to prevent the out-diffusion of Si into volumes of the Al paste more distant to the contact are described in literature. For example the beneficial measures of adding silicon to the Al paste [104] or reducing the diffusivity D of Si in commercial Al pastes [100] have been investigated.

It is often observed, that there is no eutectic in the volume of the trench formed by dissolution of silicon from the wafer but instead a void is formed during the alloying process [105–107]. Under certain conditions voids can increase the series resistance of a solar cell [108], but also very good specific contact resistances are reported for voided contacts [109]. Furthermore, there are publications that indicate a reduced BSF depth of contacts with voids compared to filled contacts [107, 110]. However, both contact types can also exhibit comparable BSF depths [106]. It is experimentally found that increasing the Si concentration in the Al-paste suppresses void formation [100, 105, 107] and different approaches to achieve this have been reported. These approaches include reducing the contact line pitch [105], optimizing the firing profile [110, 111] and screen printing Al-fingers instead of a full-area Al layer [75, 107, 112]. This last approach is inherent to the bifacial PERC+ cell concept described in section 3.2. The physical root cause of void formation has been attributed [107, 113] to the Kirkendall effect [114]. Recently, however, Dressler et al. [111] investigated void rates in dependence of the applied firing temperature profile and indicated, that the Kirkendall effect does not describe the experimental data.

Section 5.3 of this work presents a new analytical model, which proposes surface energy minimization as the root cause of void formation.

Polishing and cleaning of the rear side of industrial-type PERC solar cells

In this chapter we investigate for the first time the impact of the rear surface roughness on the electrical and optical properties of PERC solar cells with screen printed rear side metalization. Based on these findings we adopt the edge isolation process known from full-area Al-BSF solar cells to a novel PERC process flow with reduced process complexity. Finally, we evaluate different cleans prior to ALD-Al_2O_3/SiN_x passivation.

4.1 Impact of the rear surface roughness

In order to determine the amount of polishing required to obtain excellent PERC cell conversion efficiencies, we vary the rear surface roughness by adjusting the polishing process time of the RENA InPilot tool (see section 3.3.1). By comparing two different rear surface passivation layer stacks, namely thermal SiO_2/SiN_x and atomic layer deposited (ALD) Al_2O_3/SiN_x, we evaluate a potentially different impact of the rear surface roughness on different passivation layers. We study the corresponding impact on the solar cell parameters of industrial-type PERC solar cells. The rear surface recombination velocity (SRV) is analyzed based on IQE measurements of these PERC cells in addition to measurements of the effective lifetime on test samples. Both approaches are checked on consistency by comparing the IQE-measured SRV S_{rear} with calculated S_{rear} values derived from the measurements on the lifetime test wafers.

Test wafer experiments: Impact of the surface roughness on surface recombination velocity

In order to analyze the impact of the surface roughness on the surface recombination velocity, we use $300\,\mu m$ thick p-type boron-doped FZ wafers. After wafer cleaning

and double sided alkaline texturing, we subsequently polish both sides of the FZ wafer using the RENA InPilot tool. We vary the polishing time of the single sided wet chemical polishing process resulting in different silicon removals between 0 and 20 µm in order to obtain different surface roughness ranging from textured to planar. Figure 4.1 shows scanning electron microscope (SEM) cross sections of alkaline textured wafers with varying wet chemical polishing times resulting in different Si removals between 0 µm and 20.9 µm. The resulting surface roughness as determined by the residual pyramid height varies between 0 µm (20.9 µm removal) and 5 µm (0 µm removal, fully textured).
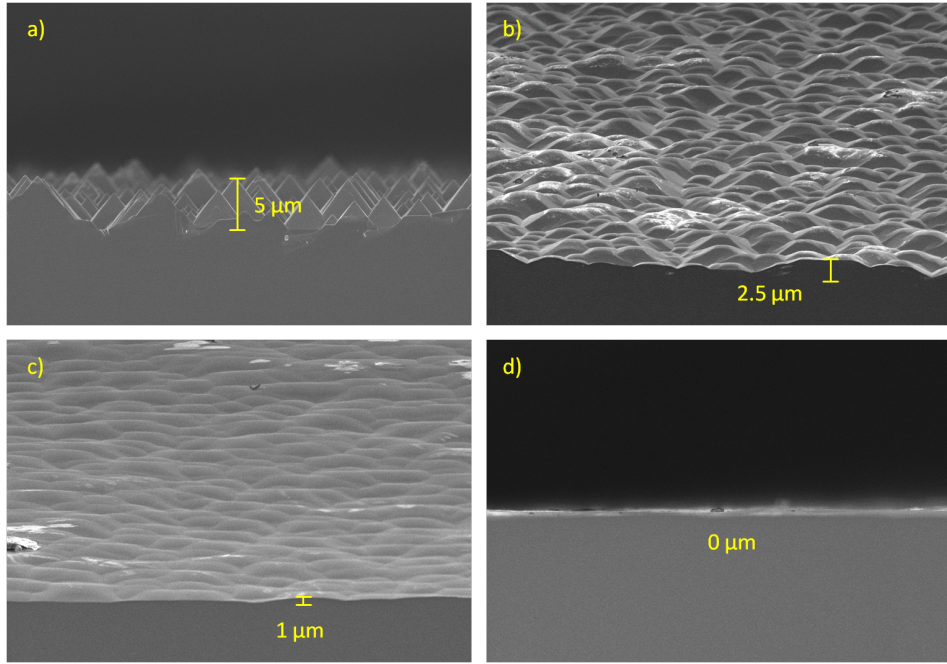
Figure 4.1: SEM cross-section images of different polishing removals: a) 0 µm polishing removal (fully textured) b) 5.8 µm c) 14.0 µm d) 20.9 µm. Derived from the SEM images, the surface roughness is around 5 µm, 2.5 µm, 1 µm and 0 µm, respectively.

We compare two different passivation layer stacks: Either a stack of thermal SiO_2 (10 nm thickness) and 200 nm PECVD SiN_x or alternatively ALD-Al_2O_3 (10 nm thickness) with a 200 nm thick PECVD SiN_x capping layer. Finally, the wafers are fired in a conveyor belt furnace with a typical firing temperature profile. Afterwards, we measure the lifetimes via photoconductance-calibrated photoluminescence lifetime imaging (PC-PLI, see section 2.2.3) and dynamic infrared lifetime mapping (dynILM, see section 2.2.2). We prepare a second set of wafers where we locally open the rear passivation by laser contact opening (LCO) using different contact line pitches and then apply full-area Al screen printing. After firing, we measure the lifetime for each pitch size by dynILM. This methodology allows to determine the surface recombination velocity of the passivated areas S_{pass} and the surface
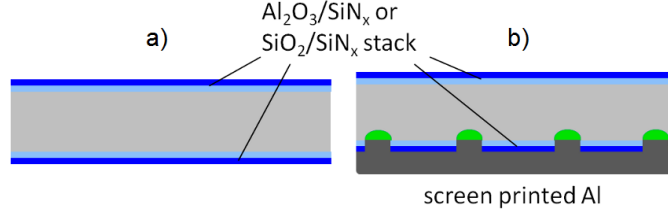
Figure 4.2: Schematic drawing of FZ wafers for lifetime measurements. Symmetrical test wafers of type a) are used to determine the SRV S_{pass}. Wafers with rear metallization (type b) allow for determining the SRV in the passivated (S_{pass}) as well as the metallized (S_{met}) areas.

recombination velocity of the metalized areas S_{met} [115]. As a reference we process wafers without texturing and wet chemical polishing. Thus the passivation layer is deposited directly after cleaning and damage etching on the FZ wafer. The surfaces of these wafers are termed planar. Figure 4.2 shows schematic drawings of the test wafers resulting from the process flow as described above.

Figure 4.3 shows PCPLI measurements of SiO_2/SiN_x and Al_2O_3/SiN_x passivated test wafers according to Figure 4.2a) with different surface roughness. In case of SiO_2/SiN_x passivation, the SRV S_{pass} considerably increases from 10–20 cm/s for samples with planar surfaces to values between 50–200 cm/s for rougher surfaces at an excess carrier density of $2 \cdot 10^{13}\,\mathrm{cm}^{-3}$. Also, for rough surfaces the SRV strongly increases with lower injection level. In case of the Al_2O_3/SiN_x surface passivation, S_{pass} depends significantly less on the surface roughness and the injection level with S_{pass} values from 10–30 cm/s for the planar case and 30–100 cm/s for rougher samples.

We additionally measure S_{pass} of passivated wafers according to Figure 4.2a) by dynILM at an injection level of $\Delta n = 1 \cdot 10^{15}\,\mathrm{cm}^{-3}$ as shown in Figure 4.4. For SiO_2/SiN_x passivation stacks we observe a decrease of S_{pass} from about 60 cm/s for textured surfaces to values below 20 cm/s for planar surfaces. In contrast, the S_{pass} values of Al_2O_3/SiN_x improve from 30 cm/s to around 10 cm/s already for small polishing removals of 5 µm. The values are in good accordance with Figure 4.3 considering the same injection level and surface roughness. Figure 4.4 also shows the SRV values S_{met} of the local screen printed aluminum rear contacts obtained from test wafers with Al_2O_3/SiN_x passivation according to Figure 4.2b). The SRV S_{met} is constant for wide ranges of the rear surface roughness at values around 300–600 cm/s. However, two data points for fully textured and planar surfaces show an increase to S_{met} of 1500 cm/s. To check if the surface roughness influences the contact formation on the rear side and thus S_{met}, we take SEM images of samples with textured and planar rear side as shown in Figure 4.5. We observe identical sizes of the local contacts and identical depths of the local back surface field (BSF). Hence the increase in S_{met} for textured rear sides is not expected based on the SEM cross-sections.
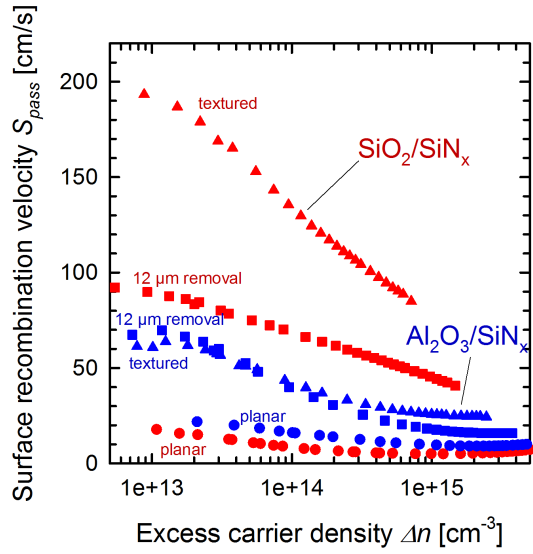
Figure 4.3: Surface recombination velocity S_{pass} determined by PCPLI measurements of test wafers according to Figure 4.2a). The results are shown for samples with planar (circles), textured (triangles) and polished (squares, 12 μm removal) surfaces for both Al_2O_3/SiN_x (blue) and SiO_2/SiN_x (red) passivation stacks.
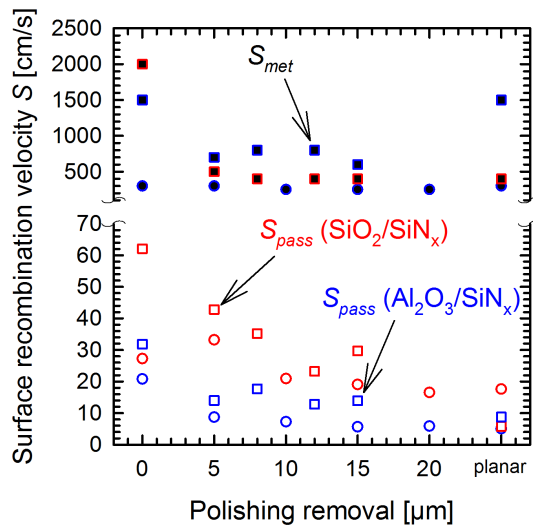

Figure 4.4: Surface recombination velocities S_{pass} (open symbols) measured by dynILM on test wafers according to Figure 4.2a) with SiO_2/SiN_x (red) and Al_2O_3/SiN_x (blue) passivation in dependence of the Si polishing removal. The values correspond to an injection level of $\Delta n = 1 \cdot 10^{15}\,\text{cm}^{-3}$. The SRV values of the local aluminum contacts S_{met} (black filled symbols) are extracted from test wafers according to Figure 4.2b) using SiO_2/SiN_x (red) or Al_2O_3/SiN_x (blue) passivation. Different symbol shapes indicate different wafer batches.
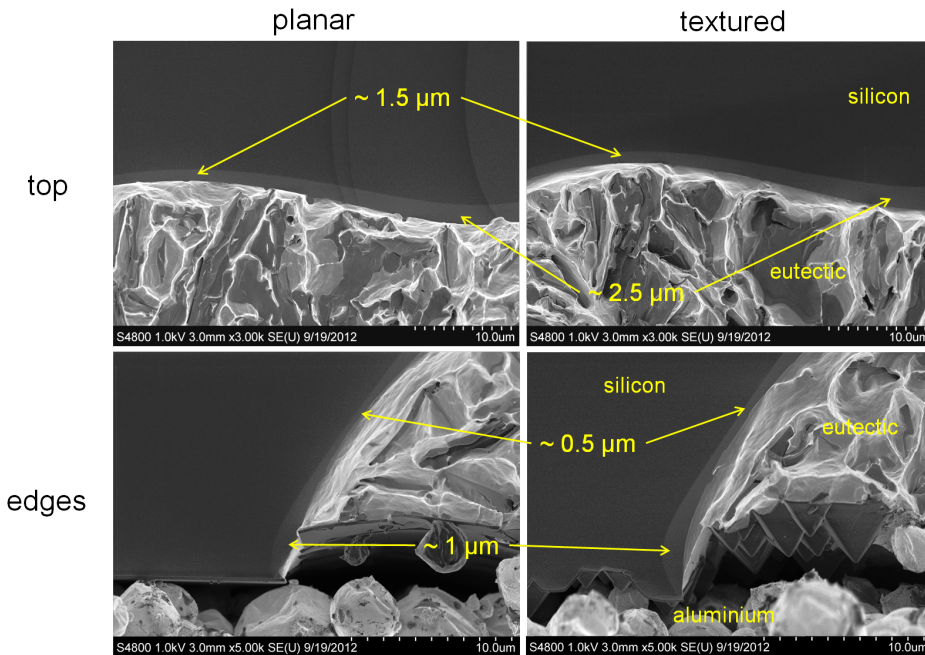
Figure 4.5: SEM cross-sections of the top and the edge of a local screen printed aluminum rear contact for planar and textured rear surfaces. The yellow arrows indicate position and depth of the BSF.

PERC solar cell results: Impact of surface roughness on electrical and optical properties

In order to investigate the impact of the rear surface roughness on PERC solar cells, we develop a process flow where we systematically vary the rear surface roughness without influencing other process parameters. The process flows are shown in Figure 4.6. The process flow with blue boxes refers to the reference PERC process flow of section 3.1.1. The process steps shown in red boxes describe the modified PERC process flow applying the wet chemical polishing of the wafer rear after double sided texturing.

We start processing the rear polished PERC cells by wafer cleaning and KOH damage etching. The KOH damage etch time is adjusted for the different rear side polishing removals resulting in a final wafer thickness of 150 μm for all split groups including the reference cells. After texturing, the RENA InPilot tool is used to polish the rear surface of the wafers. The variation of the polishing time results in different Si removals between 0 μm and 20.9 μm. Therefore, the surface roughness corresponds to those of the wafers shown in Figure 4.1 and varies between 0 μm and 5 μm. Afterwards, a rear protection layer is deposited which enables a single sided phosphorus diffusion. The PSG and the rear protection layer are then removed by a wet etch step. We compare two different rear passivation
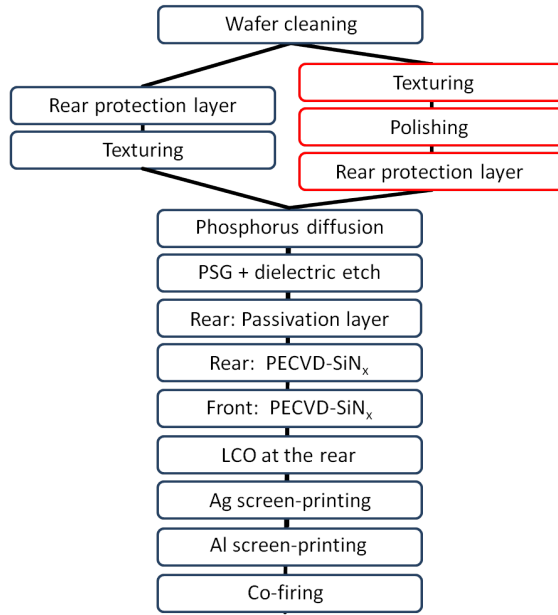
Figure 4.6: Process flows of the PERC solar cells. Reference PERC cells (blue) with planar rear side are compared to wet chemically polished cells (red) with different polishing removals resulting in different rear surface roughness.

stacks, thermal SiO_2/SiN_x and ALD-Al_2O_3/SiN_x. In case of the SiO_2/SiN_x stack we oxidize the wafers resulting in a $10\,nm$ thin thermal SiO_2 on both wafer surfaces followed by a PECVD SiN_x capping layer on the rear. In case of the Al_2O_3/SiN_x stack, we deposit a $10\,nm$ thin plasma-assisted ALD-Al_2O_3 layer on the wafer rear followed by a PECVD SiN_x capping layer. The subsequent process steps correspond to the reference PERC process of section 3.1.1. A schematic drawing of the resulting PERC solar cell with SiO_2/SiN_x passivation is shown in Figure 4.7. We process 5 PERC solar cells for each polishing removal value. We vary the peak firing temperature for the 5 different solar cells in order to ensure an optimum
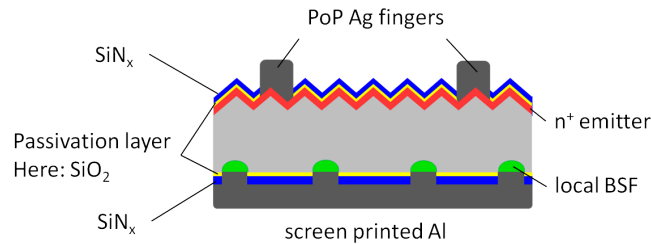

Figure 4.7: Schematic drawing of the SiO_2/SiN_x rear-passivated PERC solar cell applied in this study. In case of the Al_2O_3/SiN_x passivated PERC cells there is no thermal SiO_2 between the emitter and the SiN anti-reflection coating.
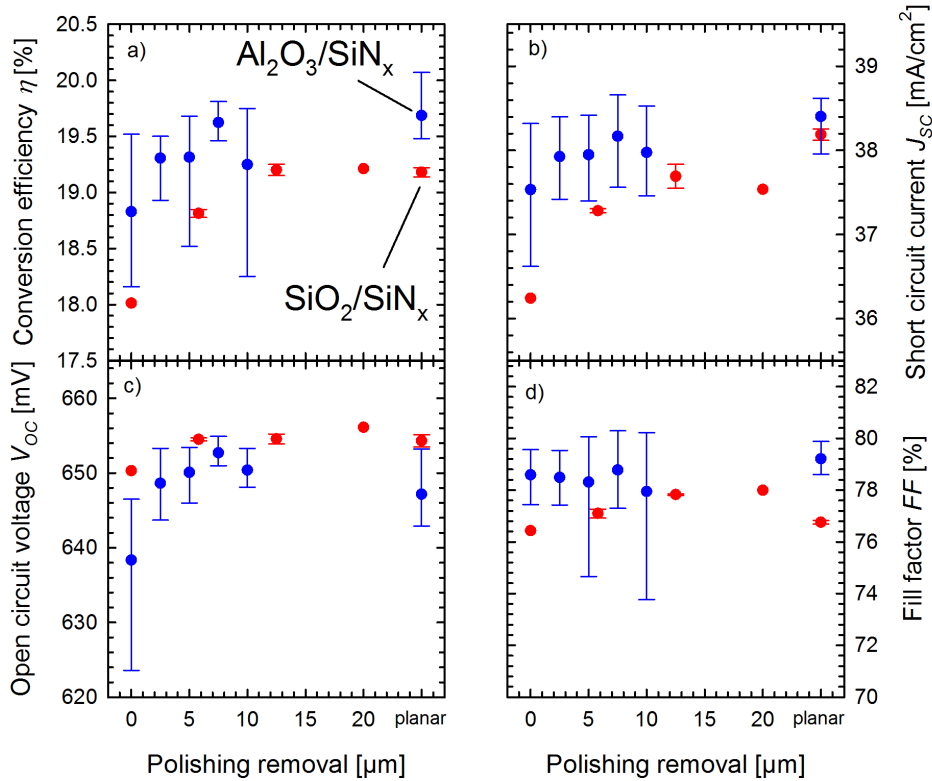
Figure 4.8: Conversion efficiency η (a), short circuit current density J_{sc} (b), open circuit voltage V_{oc} (c) and fill factor FF (d) for Al_2O_3/SiN_x (blue) and SiO_2/SiN_x (red) passivated PERC solar cells with different rear polishing removals. Each data point represents an average value of solar cells fired at optimal conditions, whereas the error bars indicate minimal and maximal values. The total number of PERC solar cells per polishing removal is 4–7 for Al_2O_3/SiN_x and 1–2 for SiO_2/SiN_x passivation.

contact firing and lowest contact resistance for each polishing removal. In case of Al_2O_3/SiN_x we process two batches of PERC solar cells resulting in 2x5 cells per polishing removal. The peak firing temperatures resulting in highest fill factors and lowest series resistances are considered to be optimal.

Figure 4.8 shows the average values of the measured IV parameters in dependence of the polishing removal for all solar cells fired at optimal conditions. In addition, the error bars indicate minimum and maximum values. For the SiO_2/SiN_x passivated PERC cells, only one or two solar cells per polishing removal are considered to be fired at optimum temperature. In case of the Al_2O_3/SiN_x passivated PERC cells, four to seven PERC cells receive optimum firing temperatures per polishing removal which partly explains the higher scattering of the Al_2O_3/SiN_x IV data. The results of the reference PERC cells with planar rear side are displayed as "planar" on the x-axis. In case of SiO_2/SiN_x passivation the conversion efficiency

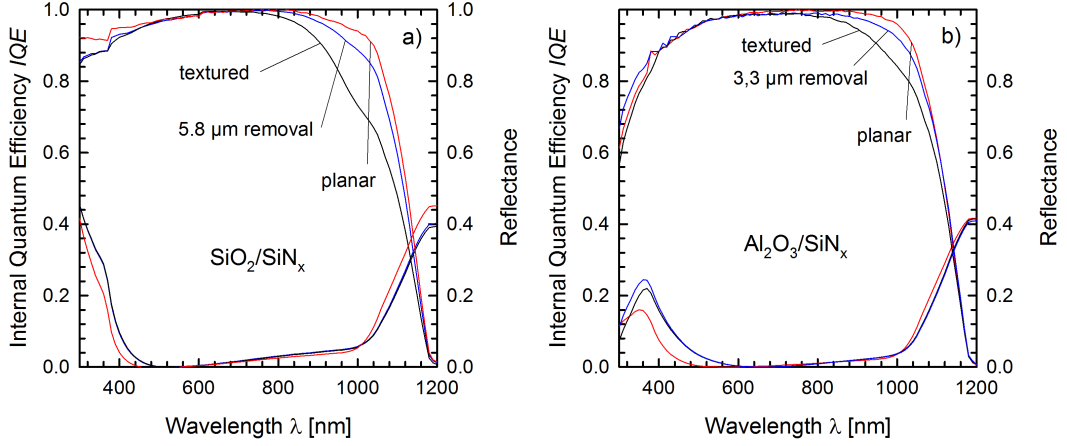**Figure 4.9:** Internal quantum efficiency (IQE) and reflectance for cells with SiO_2/SiN_x (a) and Al_2O_3/SiN_x (b) passivation and rear surface roughness as indicated.

η strongly increases from 18.0% to 19.2% when moving from a textured to a planar rear surface. For the Al_2O_3/SiN_x passivation, an increased polishing removal improves the average conversion efficiency from 18.8% to 19.7%. For rear-polished PERC cells, the best efficiency of 19.8% has been achieved using an Al_2O_3/SiN_x passivation and a polishing removal of 7.8 μm. For both rear passivation stacks, the dependence of the efficiency on the polishing removal is mainly caused by an increased short circuit densitiy J_{sc} by 1–2 mA/cm^2 and by an increased open circuit voltage V_{oc} by 5–15 mV when moving from textured to planar. The fill factor FF shows no systematic dependence on the polishing removal with average values around 78.5% (Al_2O_3/SiN_x) and 77% (SiO_2/SiN_x). Based on Figure 4.8 we conclude, that PERC cells with Al_2O_3/SiN_x passivation require a polishing removal of around 7 μm, whereas SiO_2/SiN_x-passivated PERC cells need 10–15 μm polishing removal to obtain highest efficiencies.

In order to analyze the impact of the rear surface roughness on the J_{sc}, we measure the internal quantum efficiency (IQE) and the reflectance for both passivation layers as shown in Figure 4.9a) and b). The IQE in the infrared wavelength regime strongly decreases with increasing rear surface roughness for SiO_2/SiN_x, whereas this decrease is less pronounced for Al_2O_3/SiN_x rear passivated PERC cells. We model the experimental reflectance and IQE data (see section 2.3) in order to obtain the effective rear surface recombination velocity S_{rear} as presented in Figure 4.10. The S_{rear} values of the SiO_2/SiN_x passivated PERC cells (red circles) strongly increase from about 130 cm/s for planar surfaces up to over 2000 cm/s for the textured rear whereas for Al_2O_3/SiN_x passivated PERC cells (blue circles) we find an increase from 50 cm/s to around 500 cm/s. The S_{rear} values of Figure 4.10 can
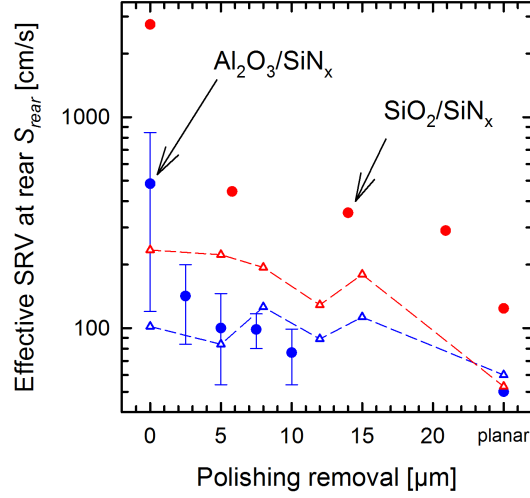
Figure 4.10: Average S_{rear} values of PERC solar cells extracted from IQE measurements (circles) and calculated S_{rear} values (triangles with lines) using equation 4.1, S_{pass} values from Figure 4.3 and S_{met} values from Figure 4.4. Values are presented for Al_2O_3/SiN_x (blue) and SiO_2/SiN_x (red) passivation in dependence of the polishing removal. Error bars indicate the minimal and maximal values. The lines are a guide to the eye.

be related to the S_{pass} values in Figure 4.3 and the S_{met} values in Figure 4.4 by using the equation developed by Fischer [63]

$$S_{rear} = \left(\frac{R_{bulk} - \rho W}{\rho D} + \frac{1}{f S_{met}} \right)^{-1} + \frac{S_{pass}}{1 - f} \qquad (4.1)$$

with a base resistivity $\rho = 2\,\Omega cm$, thickness $W = 150\,\mu m$, diffusion coefficient $D = 29.8\,cm^2/s$, metallization fraction $f = 10\%$ and the contribution of the bulk to the series resistance $R_{bulk} = 0.17\,\Omega cm^2$ [116]. Based on Figure 4.4 and Ref. [117], S_{met} is assumed to be $400\,cm/s$, whereas S_{pass} is derived from Figure 4.3 at an excess carrier density of $\Delta n \approx 2 \cdot 10^{13}\,cm^{-3}$ which corresponds to the injection level of the IQE measurement under bias light. The corresponding calculated S_{rear} values are shown in Figure 4.10 as triangles. The calculated S_{rear} values by the Fischer equation correspond well to the S_{rear} values determined by the IQE measurements for most of the Al_2O_3/SiN_x data. However, the S_{rear} values of the SiO_2/SiN_x-passivated PERC cells clearly exceed the corresponding S_{rear} values calculated from the test wafers. For fully textured rear surfaces ($0\,\mu m$ polishing) the measured S_{rear} values strongly exceed the calculated S_{rear} values, also partly in case of the Al_2O_3/SiN_x passivated PERC cells. Even when assuming an S_{met} value of $1500\,cm/s$ for textured surfaces, which would be in accordance with Figure 4.4, S_{rear} values of $300\,cm/s$ and beyond cannot be described. Although the discrepancies for

textured rear sides remain unclear, the generally larger offset in case of SiO_2/SiN_x is probably caused by parasitic shunting [38]. Parasitic shunting describes the effect, that a passivation layer with positive fixed charges – such as SiO_2/SiN_x – induces a floating junction at the rear side, which accumulates minority carriers. These carriers may flow to the rear contacts through the parasitic shunt resistance causing a higher effective recombination at the rear. This effect is not expected for Al_2O_3/SiN_x passivation with its negative fixed charges that repel minority carriers at the rear side.

We model the reflectance measurements of Figure 4.9a) and b) (see section 2.3 in order to extract the internal reflectance at the rear side R_b, the Lambertian fraction Λ indicating the diffuse part of the rear reflectance and the optical path enhancement factor (P.E.F.) Z_0. Since $Z_0 \cdot W$ describes the effective path length in a device with wafer thickness W for nearbandgap light at 1200 nm, Z_0 is a suitable measure for the light trapping capability of a cell [118, 119]. As shown in Figure 4.11a), R_b tends to increase slightly from 90% to 91% (Al_2O_3/SiN_x) or 92% (SiO_2/SiN_x) with increasing polishing removal. According to the model the
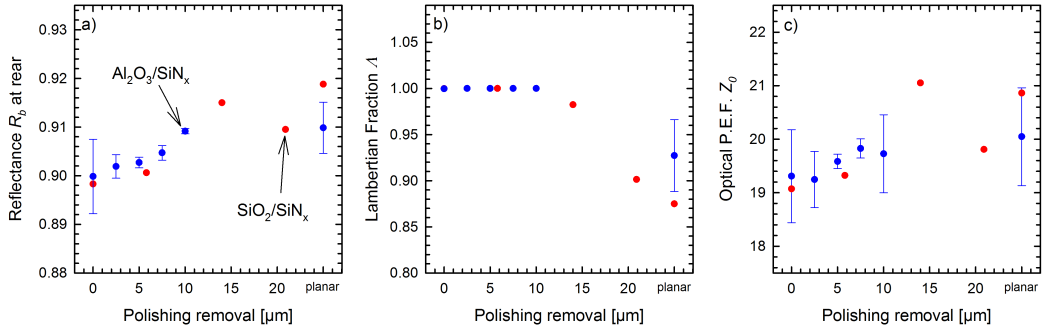

Figure 4.11: Average values for optical parameters in dependence of the polishing removal at the rear side: (a) Reflectance at the rear R_b, (b) Lambertian fraction Λ and (c) optical path enhancement factor Z_0. Error bars indicate minimal and maximal values.

improvement in R_b from 90% to 92% and thus in light trapping increases the short circuit current density by only ~0.2 mA/cm^2 and thus does not explain the strong J_{sc} variation in Figure 4.8. The lambertian fraction Λ remains at 1 for rough surfaces and begins to decrease slightly to values of 0.9 for very smooth surfaces. The optical P.E.F. Z_0 strongly correlates with R_b: It tends to increase with increasing polishing removals from 19 up to 20.5.

4.2 Development of a single-step polishing process for PERC solar cells

A possibility to reduce the process complexity and cost of PERC solar cells is to reduce the number of additional process steps compared to full-area Al-BSF cells.

Industrial PERC process flows typically involve two wet chemical single side etching steps [79, 120]. The first etching step – similar to the polishing process of the previous section 4.1 – aims at polishing the previously textured rear side of the cell and thus reduces the rear surface roughness in order to increase efficiencies [121]. The second etching step is applied after $POCl_3$ diffusion in order to remove the rear emitter. This edge isolation process is well-known from full-area Al-BSF cells.

In this section, we develop a novel single step polishing process after double sided texturing and phosphorus diffusion that simultaneously removes the rear side emitter and reduces the rear surface roughness. In contrast to the process flow of section 4.1, the emitter is already present during this polishing process, allowing the reactive gas phase to etch back the front emitter and potentially form porous silicon. Therefore the new polishing process flow requires to optimize several process parameters including the reactivity of the gas phase, the sheet resistance of the $POCl_3$ diffusion, the polishing duration as well as the cleaning sequence post polishing. This cleaning sequence must not only allow for a high quality rear surface passivation, but also remove porous silicon from the wafer front side that originates from the polishing process. The necessary optimization, however, is rewarded by a reduced process complexity as illustrated by Figure 4.12. The resulting industrial-type PERC solar cells with polished rear surface are compared to the reference PERC cells which apply a rear protection layer instead of a rear polishing process (see section 3.1.1).
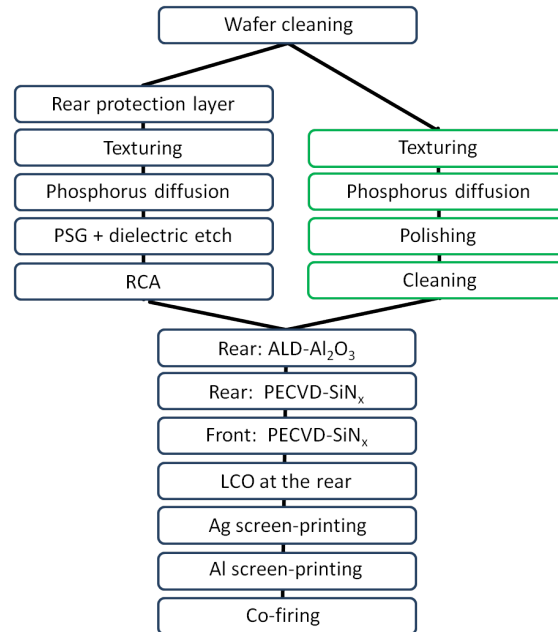

Figure 4.12: Process flows for reference PERC solar cells applying a rear protection layer (blue, see section 3.1.1) and polished PERC cells (green/blue).

Test wafer results

In order to evaluate the impact of the polishing process and the cleaning sequence on the emitter saturation current J_{0e}, the emitter sheet resistance R_{sh} and the effective carrier lifetime τ_{eff}, we fabricate two types of test wafer samples (see Figure 4.13). We apply two different cleaning sequences: 1) pSC1, HF/HCl, HF-Dip; 2) pSC1,
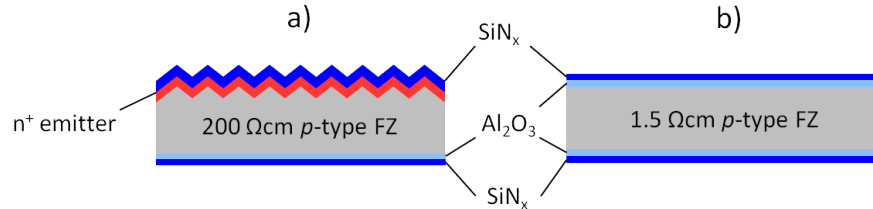

Figure 4.13: Schematic drawing of test wafers for measurement of the emitter saturation current J_{0e} and emitter sheet resistance R_{sh} (a) and of test wafers for measurement of the effective carrier lifetime τ_{eff} (b).

HF/HCl, HF/O$_3$. These cleaning sequences are designed as shortened versions of the RCA clean. The pseudo-SC1 (pSC1) clean applies KOH/H$_2$O$_2$ chemistry and aims at removing organic contamination similar to the Standard Clean 1 (SC1) in the RCA clean. The HF/HCl clean removes metallic contaminants similar to the Standard Clean 2 (SC2) in the RCA clean sequence. Both, the pSC1 and HF/HCl clean, are well known as typical industrial cleans prior and post texturing, respectively. The test wafers of Figure 4.13a) are processed applying double sided texturing and a POCl$_3$ diffusion with a sheet resistance of $45\,\Omega$/sq. We then use the InPilot tool to apply the wet chemical single sided polishing process to remove the rear emitter and reduce rear surface roughness. We choose rear side polishing removals of $3\,\mu$m, $7\,\mu$m and $12\,\mu$m by adjusting the process time. The gas phase of the rear polishing process slightly increases the emitter sheet resistances from $45\,\Omega$/sq to $50\,\Omega$/sq ($3\,\mu$m), $60\,\Omega$/sq ($7\,\mu$m) and $70\,\Omega$/sq ($12\,\mu$m) as measured with a four point probe on parallely processed reference test wafers. After cleaning either with pSC1, HF/HCl, HF-Dip or pSC1, HF/HCl, HF/O$_3$, we deposit the Al$_2$O$_3$/SiN$_x$ passivation layer stack on the rear and the SiN$_x$ on the front side and conclude with a firing step. Test wafers as shown in Figure 4.13b) are double sided textured and subsequently polished with different removals, where each polishing removal is applied to both wafer sides. Then we carry out one of the cleaning sequences, deposit the Al$_2$O$_3$/SiN$_x$ on both sides and finish again by firing the wafers. The measurements of J_{0e}, R_{sh} and τ_{eff} of the final wafers are carried out on a Sinton lifetime tester.

When moving from $3\,\mu$m to $12\,\mu$m polishing removal, the emitter saturation current densities decrease from 110–140 fA/cm^2 down to 70–95 fA/cm^2 for both cleaning sequences as shown in Figure 4.14a). The improved J_{0e} values are very likely due to a reduced phosphorus concentration on the front surface caused by
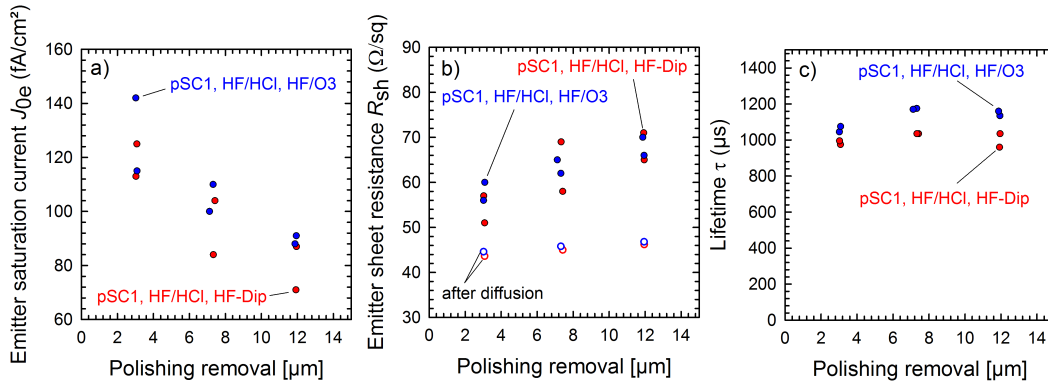
Figure 4.14: PCD-measured parameters of test wafers of type a) and b) in Figure 4.13: (a) Emitter saturation current density J_{0e}; (b) Emitter sheet resistance R_{sh}; (c) Effective carrier lifetime τ_{eff} at an injection level of $1 \cdot 10^{15}\,\mathrm{cm}^{-3}$.

the longer gas phase etch during polishing [122]. The low J_{0e} values demonstrate, that both cleaning sequences sufficiently remove the porous silicon to allow a good emitter surface passivation while maintaining emitter sheet resistances below $70\,\Omega/\mathrm{sq}$ as shown in Figure 4.14b), where both cleaning sequences only contribute about $2\,\Omega/\mathrm{sq}$ sheet resistance increase as measured on reference wafers. The PCD measurements of testwafers according to Figure 4.14b) show effective lifetimes τ_{eff} around 1 ms for all polishing removals, where wafers cleaned with pSC1, HF/HCl, HF/O_3 obtain 100–150 μs higher lifetimes compared to the pSC1, HF/HCl, HF-Dip clean. Accordingly, both cleaning sequences allow an excellent rear surface passivation quality with SRVs $S_{pass} < 15\,\mathrm{cm/s}$ when combined with an Al_2O_3/SiN_x rear passivation.

Solar cell results

In a next step we process polished PERC cells according to the process flow in green boxes in Figure 4.12. The two cleaning sequences used in the test wafer experiment are now designed to be slightly shorter: 1) pSC1, HF/HCl; 2) pSC1, HF/O_3. The wafers apply double sided texturing and a phosphorus diffusion aiming at a sheet resistance of $45\,\Omega/\mathrm{sq}$. After the polishing process with a rear side polishing removal of $5\,\mu\mathrm{m}$, we carry out the cleaning sequences. We then continue with deposition of the rear side passivation following the same process flow of PERC solar cells as described in section 3.1.1.

Figure 4.15a) shows the energy conversion efficiencies η of the polished PERC solar cells for different cleaning sequences. The laboratory type RCA cleaning prior to passivation resulted in a polished PERC solar cell with an efficiency of 20.7%, a V_{oc} of 659 mV, a J_{sc} of $38.7\,\mathrm{mA/cm^2}$ and a FF of 81.0%. PERC cells cleaned with the pSC1, HF/O_3 or the pSC1, HF/HCl cleaning sequence show significantly reduced efficiencies of up to 19.9% and 19.4%, respectively. The cause

for this trend is revealed by the IQE measurements of the PERC cells as shown in Figure 4.15b). Here the cells cleaned with pSC1, HF/O$_3$ or pSC1, HF/HCl show lower IQE values at short wavelengths when compared to the RCA clean indicating increased recombination at the cell's front side. We model the experimental QE
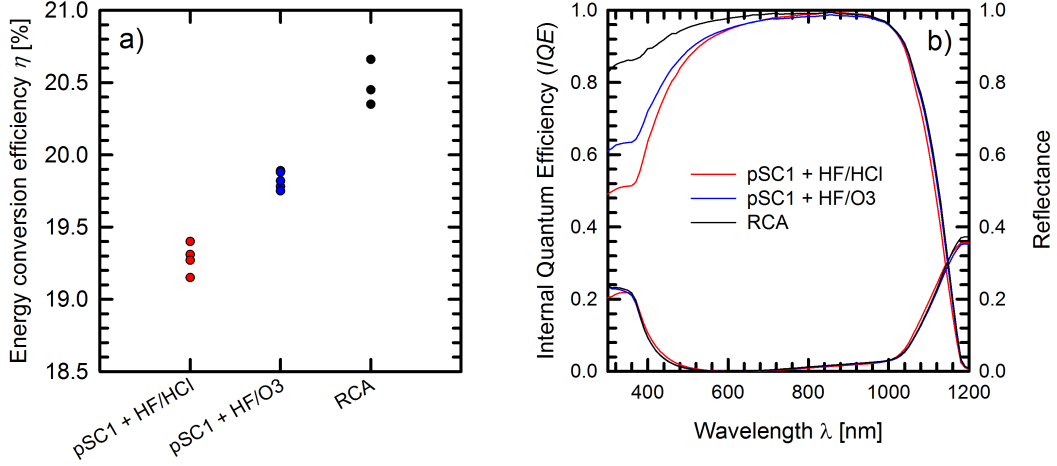

Figure 4.15: (a) Energy conversion efficiencies η of polished PERC solar cells cleaned with different cleaning sequences prior to passivation. The spread of data is partly due to a variation of peak firing temperatures; (b) IQE and Reflectance measurements of the best solar cell shown in a).

data to extract the diffusion length L_{em} and front surface recombination velocity S_{front}. Using

$$J_{0e} = \frac{qn_i^2}{N_A} \cdot \frac{D}{L_{eff}} \text{ with } L_{eff} = L_{em}\frac{L_{em}S_{front}\sinh\left(\frac{W_{em}}{L_{em}}\right) + D\cosh\left(\frac{W_{em}}{L_{em}}\right)}{L_{em}S_{front}\cosh\left(\frac{W_{em}}{L_{em}}\right) + D\sinh\left(\frac{W_{em}}{L_{em}}\right)} \quad (4.2)$$

we obtain J_{0e} values of $85\,\text{fA/cm}^2$ (RCA), $200\,\text{fA/cm}^2$ (pSC1, HF/O$_3$) and $310\,\text{fA/cm}^2$ (pSC1, HF/HCl) which fit well to the results of a second set of test wafers (Figure 4.13a) processed in parallel to the PERC solar cells. Whereas the J_{0e} value for the RCA cleaned PERC cells is comparable to the values shown in Figure 4.14a), the J_{0e} values of the pSC1, HF/O$_3$ and the pSC1, HF/HCl cleaned cells and second set of test wafers strongly exceed the J_{0e} values shown in Figure 4.14. The enhanced recombination is expected to result from porous silicon formed during the polishing step and not completely removed during the clean. We could not identify the root cause of the missing porous silicon etching capability of the cleans when applied to the PERC cells and second set of test wafers. However, it is very likely not caused by the missing HF-Dip or the missing HF/HCl step, since these cleans should not significantly etch silicon. When extracting S_{rear} we obtain comparable values $< 40\,\text{cm/s}$ for all three cleaning sequences, demonstrating

that pSC1, HF/HCl and pSC1, HF/O$_3$ suffice to allow excellent passivation using an ALD-Al$_2$O$_3$/PECVD-SiN$_x$ passivation layer stack.

4.3 Industrial cleaning sequences for Al$_2$O$_3$ passivated PERC solar cells

The best PERC solar cells from the previous section, that include double sided texturing, double sided POCl$_3$ diffusion and single sided wet chemical polishing use an RCA clean after polishing and prior to ALD-Al$_2$O$_3$ deposition. This clean however is costly in industrial process flows due to its process length and expensive chemicals. In this section, we evaluate shorter cleaning sequences e.g. HF/O$_3$ in a single step resulting in hydrophobic surfaces similar to the RCA clean. In order to decouple the impact of the cleans from the impact of the polishing process on the PERC cells, we apply the cleans to the reference PERC process flow from section 3.1.1.

Lifetime sample results

Using the RENA Batchlab – a down-sized industrial cleaning tool – we evaluate four different cleaning sequences targeted for industrial application prior to Al$_2$O$_3$/SiN$_x$ passivation: 1) pSC1, HF/HCl; 2) pSC1, HF/HCl, HF/O$_3$; 3) HF/O$_3$; 4) PSG-etch (1% HF) and compare the results to a laboratory type RCA clean. As described in the previous section the cleaning sequences 1 and 2 are designed as shortened versions of the RCA clean where the pSC1 clean aims at removing organic contamination similar to the SC1 and the HF/HCl clean removes metallic contaminants similar to the SC2 clean. In cleaning sequence 3, SiO$_2$ formed by ozone is removed by HF chemistry. The resulting etching of the silicon wafer surface might remove contaminants from the surface. The PSG-etch (clean 4) is chosen because it is the typical clean of a standard full-area Al-BSF production process applied after phosphorus diffusion and before Al screen printing. To evaluate the impact of a cleaning sequence on the subsequent rear side passivation only, we fabricate test wafers for measurement of the effective lifetime τ_{eff} (compare Figure 4.13b) from the previous section). Using 1.5 Ωcm FZ material these wafers are cleaned with the 5 cleaning sequences as described above. Then the ALD-Al$_2$O$_3$/PECVD-SiN$_x$ passivation layer stack is deposited on both sides. After a firing step τ_{eff} is measured using a Sinton lifetime tester.

Figure 4.16 shows, that highest lifetimes of 1–2 ms are achieved using the RCA clean or one of the HF/O$_3$ based cleaning sequences. Using $S_{\text{pass}} = W/2 \cdot \tau_{\text{eff}}$ this corresponds to a SRV of 8–15 cm/s. The two wafers cleaned with pSC1 + HF/HCl show lower lifetimes of 700 µs and 1200 µs yielding S_{pass} values of 12–20 cm/s. The lowest lifetime of around 500 µs – corresponding to an S_{pass} of 30 cm/s – is obtained for the PSG etch, probably due to insufficient removal of metallic contaminants.
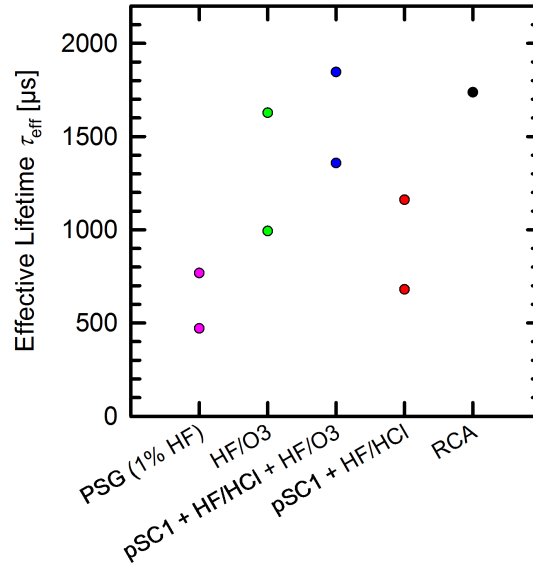
Figure 4.16: Effective carrier lifetime τ_{eff} of test wafers according to Figure 4.13b) cleaned with different cleaning sequences prior to passivation.

PERC solar cell results

In addition to the test wafers we fabricate PERC solar cells according to the PERC process flow as described in section 3.1.1. The PERC cells apply a POCl$_3$ diffusion aiming at a sheet resistance of $60\,\Omega/\text{sq}$. After wet chemical removal of the PSG and the rear protection layer, we use the RENA Batchlab to carry out the same five cleaning sequences that were applied to the test wafers mentioned above. The process flow continues with the deposition of the passivation layers, LCO and the screen printing steps.

Figure 4.17a) shows the resulting energy conversion efficiencies η of the PERC solar cells for all 5 cleaning sequences. The best efficiencies of up to 20.4% are achieved using the pSC1, HF/HCl cleaning sequence. The cleaning sequences pSC1, HF/HCl, HF/O$_3$ and HF/O$_3$ show efficiencies of around 20.0%, and the PSG etch of up to 19.4%. Figure 4.17a) also shows the results of identically processed PERC cells from another batch that applied a laboratory type RCA clean before passivation with a best efficiency of 20.3%. The different cell efficiencies primarily result from different open circuit voltages V_{oc} that range from lowest values around 630 mV for the PSG-etch up to 657 mV for the RCA clean. The lower Voc of the PERC cells with PSG clean is in accordance with the low lifetimes as shown in Figure 4.16. The lower V_{oc} of the PERC cells applying HF/O$_3$ terminated cleans will become obvious in the following experiment. The PERC cells cleaned with the HF/O$_3$-based sequences also show lower fill factors FF (see Figure 4.17b) when compared to the cells cleaned with pSC1, HF/HCl or RCA. The EL-images of the HF/O$_3$ cleaned PERC cells show dark spots, hinting to an increased contact
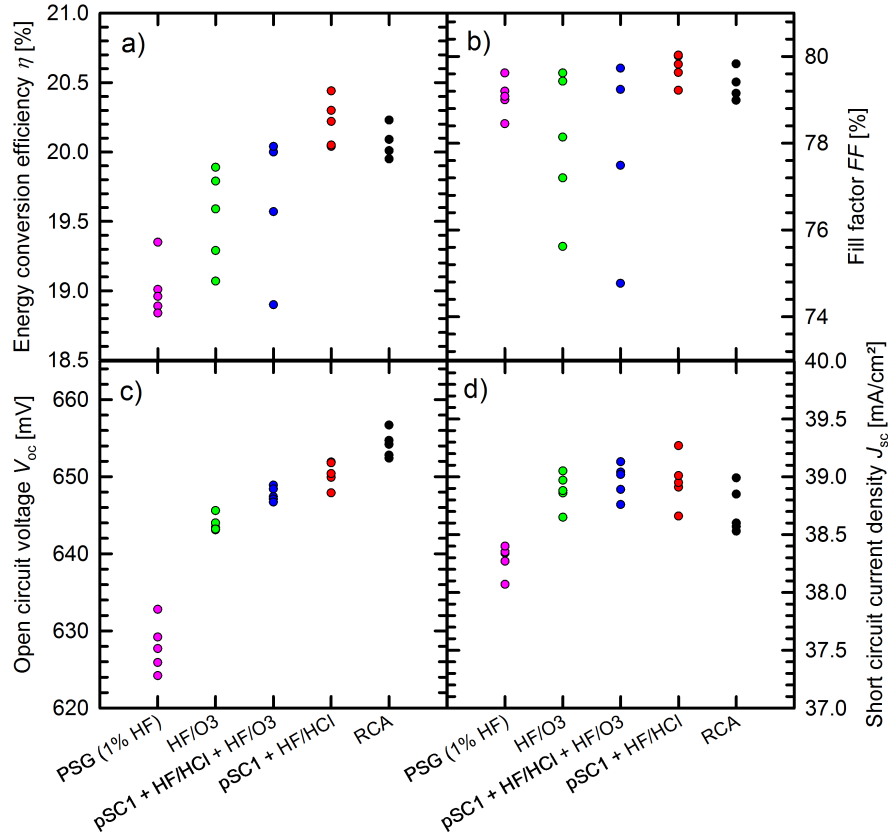
Figure 4.17: Measured IV parameters of PERC solar applying different cleaning sequences prior to passivation: (a) Energy conversion efficiency η; (b) fill factor FF; (c) open circuit voltage V_{oc}; (d) short circuit current density J_{sc}. The spread of data is partly due to a variation of peak firing temperatures.

resistance of the Ag fingers to the emitter which might be caused by a too strong etching of the HF/O$_3$ chemistry of the emitter on the front side.

Measurements of the IQE in the infrared regime as displayed in Figure 4.18 show comparable values for most cleaning sequences except for the PSG-etch, which exhibits significantly lower values. We model the experimental reflectance and IQE data to obtain the effective SRVs at the rear S_{rear}. For the PSG-etch we extract 330 cm/s, whereas the other cleaning sequences show values <50 cm/s indicating that the lower V_{oc} and J_{sc} values of the cells cleaned with the PSG-etch primarily result from higher recombination at the rear.

HF/O$_3$ process variation

The HF/O$_3$ clean is of particular interest as a candidate for industrial application due to its affordable chemistry and short process. The results described above used
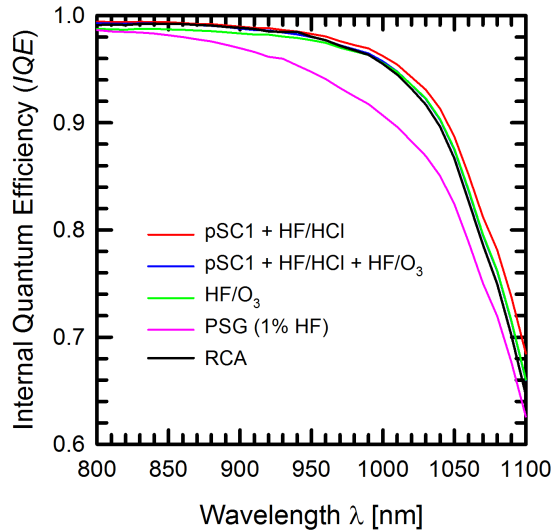
Figure 4.18: IQE measurement in the infrared regime of the best solar cells shown in Figure 4.17.

0.5% concentrated HF and an ozone concentration of $125\,g/cm^3$ that is created by an ozone generator via electrical discharge. The process time was chosen to be 5 min. In order to reduce the etch back, that led to lower fill factors in the previous experiment we fabricate another PERC solar cell batch according to the process flow in section 3.1.1 and reduce the HF/O_3 process time as well as the ozone concentration. The HF concentration for all HF/O_3 cleans in this experiment is 1%. As a reference we process PERC cells with an RCA and a pSC1 + HF/HCl clean prior to passivation.

Figure 4.19a) shows the energy conversion efficiencies in dependence of the applied clean. In accordance with the previous experiment the RCA and pSC1 + HF/HCl cleans achieve comparable best efficiencies of 20.4% and 20.3%, respectively. The best HF/O_3 cleaned solar cell achieves an efficiency of 19.8% only with an ozone concentration of $75\,g/m^3$ and a process time of 1 min. With increasing O_3 concentration and with increasing process time the efficiencies decrease even further to values below 19%. The best HF/O_3 cleaned solar cells with a process time of 1 min and ozone concentration of $75\,g/m^3$ exhibit similar fill factors around 79.5% when compared to the RCA clean. However the open circuit voltage V_{oc} is strongly reduced from 656 mV (RCA) to 642 mV and lower (HF/O_3 – $75\,g/m^3$ – 1 min). Figure 4.19b) shows that this decrease in V_{oc} is correlated to a decrease of the IQE at short wavelength and becomes more pronounced for longer process times and increasing ozone concentration (not explicitly shown in Figure 4.19b). This indicates that the HF/O_3 cleans introduce additional recombination at the n^+-doped front surface of the solar cell.
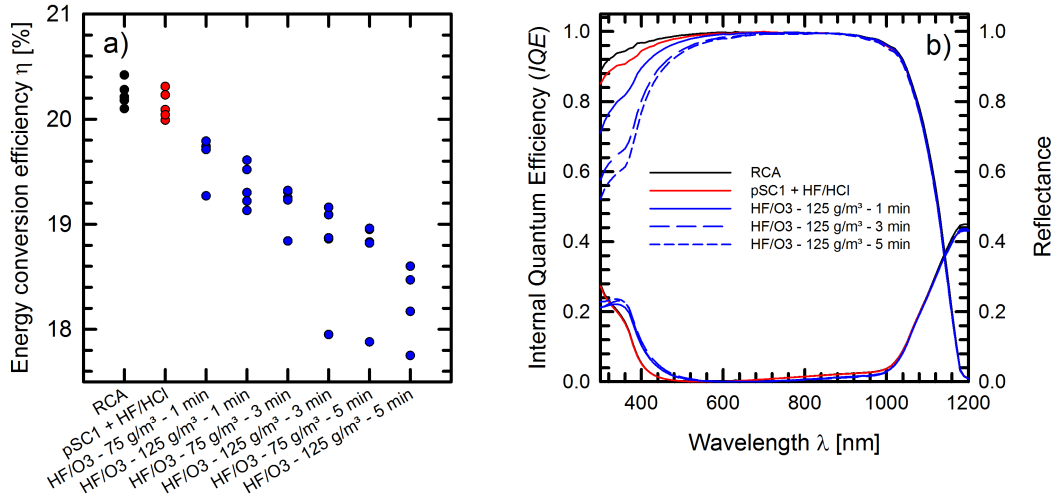
Figure 4.19: The graphs compare the following cleans prior to passivation when applied to our PERC process flow: RCA, pSC1 + HF/HCl and HF/O$_3$ with ozone concentrations and process times as indicated. The graphs show the efficiencies of each solar cell (a) and the IQE and Reflectance of the best solar cell of a group (b). For reasons of a clear view not every group is represented in b).

In order to understand the root cause of the enhanced front surface recombination we prepare special samples for analysis in a transmission electron microscope (TEM). These samples apply the PERC process flow of section 3.1.1 until the clean prior to passivation. At this point we carry out an RCA clean for one sample and an HF/HCl/O$_3$ + HF-Dip clean for another sample. The HF/HCl/O$_3$ + HF-Dip is slightly different to the HF/O$_3$ clean variations presented above. The process bath features 1% concentrated HCl in addition to the 1% HF, which aims at an improved removal of metallic contaminants during the clean. To exclude the possibility that remaining oxide from the ozone process causes the enhanced recombination on the wafer front side, we carry out an additional HF-Dip. From experiments not shown in this work we know, however, that these modifications have very little or no effect on solar cell results and can not prevent the enhanced surface recombination to arise. To maximize the impact of the HF/HCl/O$_3$ process we choose an ozone concentration of $285\,g/m^3$ and a long process time of $8\,min$. Prior to TEM imaging both samples are embedded in glue. Figure 4.20 and Figure 4.21 show TEM cross sections of wafer front surfaces of the samples cleaned with RCA and HF/HCl/O$_3$ + HF-Dip, respectively.

The RCA cleaned sample shows a very smooth surface of the pyramid flank. In contrast, the sample cleaned with the ozone based process reveals a certain roughness or even porosity on a nanometer scale. It is possible to recognize that the periodic structure of the silicon crystal is maintained even in the tips of the rough surface, indicating that the roughness is not caused by an unintended deposition of
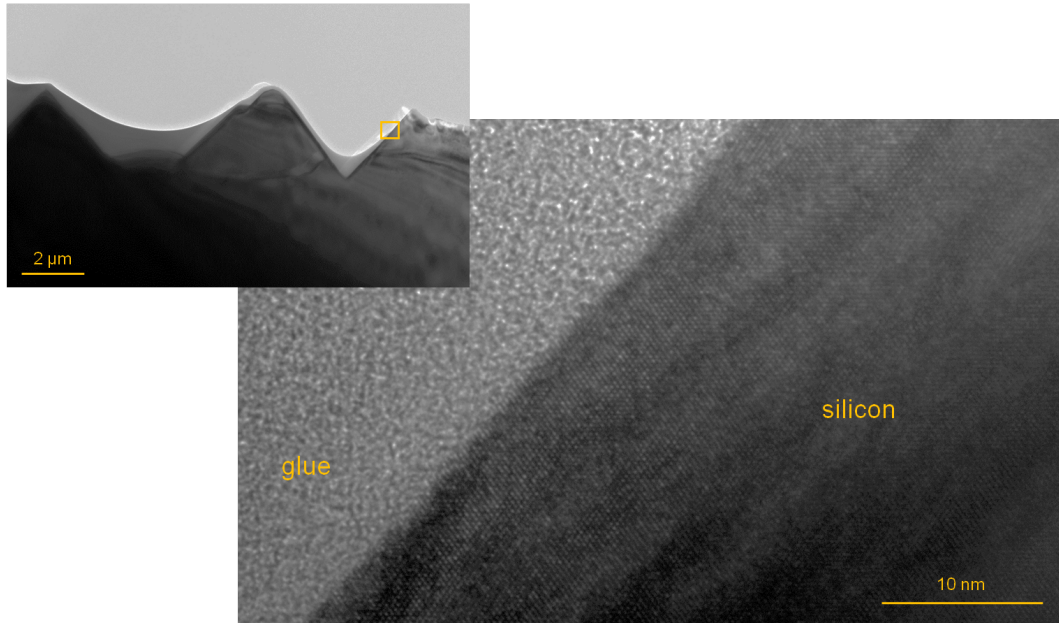
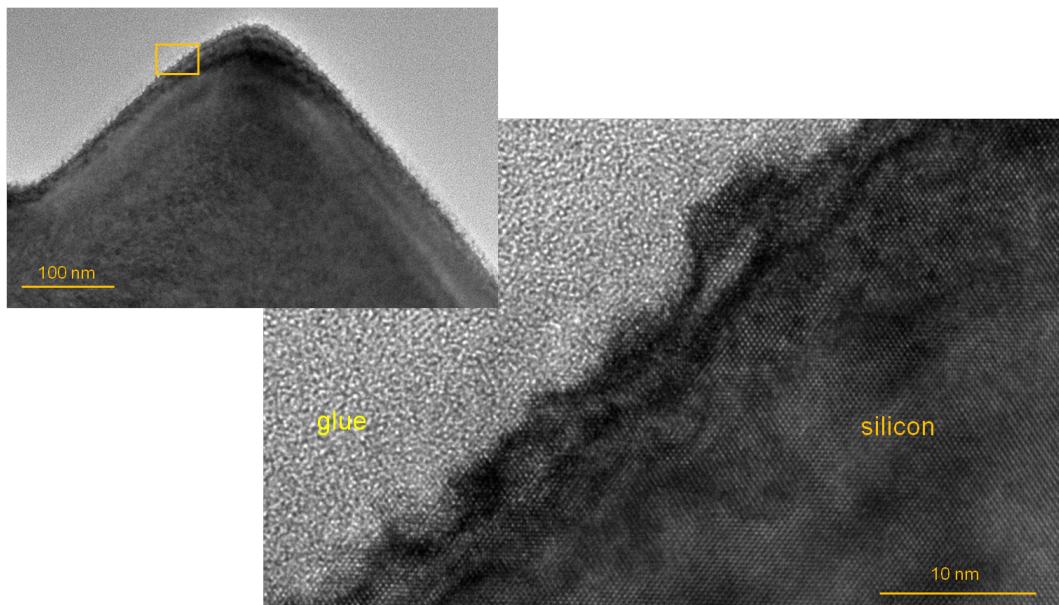**Figure 4.20:** TEM cross section image of a wafer front surface cleaned with RCA.

Figure 4.21: TEM cross section image of a wafer front surface cleaned with HF/HCl/O$_3$ + HF-Dip.

material on the surface. The rough structure increases the physical surface area in comparison to a planar (111) surface. Additionally it is challenging to passivate such rough structures using CVD deposition techniques. The observed surface morphology is therefore likely to explain the enhanced front surface recombination.

4.4 Chapter summary

The analysis of the test wafers with different rear surface roughness shows that for both passivation layer stacks, SiO_2/SiN_x and Al_2O_3/SiN_x, the surface recombination velocity S_{pass} decreases with increasing polishing removal which corresponds to a reduced surface roughness. However, the Al_2O_3/SiN_x surface passivation achieves small S_{pass} values below 20 cm/s already for 5 μm polishing removal whereas the SiO_2/SiN_x passivation requires more than 10 μm removal to obtain comparable low surface recombination velocities. The S_{pass} values of the SiO_2/SiN_x passivation stack reported in this work are in good accordance with Ref. [90]. The SRV S_{met} of the local Al rear contacts is constant at values around 400 cm/s for a large range of surface roughness with the possible exception of a considerably increased S_{met} for textured surfaces. PERC solar cells with SiO_2/SiN_x rear passivation show a strong increase of the conversion efficiency by up to 1.2%abs with reduced rear surface roughness, which has been reported similarly in Ref. [90]. However, for Al_2O_3/SiN_x passivated PERC solar cells the dependence of the conversion efficiency on the polishing removal is less pronounced with efficiencies of up to 20.1% for a planar rear surface and up to 19.8% for a polished rear surface with 7.8 μm removal. The internal quantum efficiency analysis reveals that the SiO_2/SiN_x passivated PERC cells show a very strong increase of the rear SRV S_{rear} with increasing rear surface roughness whereas the S_{rear} of Al_2O_3/SiN_x-passivated PERC cells achieves values around 100 cm/s even for small polishing removals. Although the improved conversion efficiency for higher polishing removals is primarily due to a reduced rear surface recombination, there is a small contribution of enhancement from an improved rear reflectance R_b as well, which increases by roughly 2%abs from textured to planar rear sides leading to a slightly improved light trapping. This improvement should contribute an increase in short circuit current density of $\Delta J_{sc} = 0.2 \, mA/cm^2$ as determined by analytic modeling.

Based on the surface roughness analysis we developed a novel industrial-type PERC cell process flow including double-sided texturing and phosphorus diffusion and subsequent single-sided polishing to remove the rear emitter and to reduce the rear surface roughness. Applying a rear side polishing removal of 5 μm and an RCA clean after the polishing process the resulting PERC solar cells achieve up to 20.7% efficiency, which is comparable to similarly processed reference PERC solar cells, which apply a rear protection layer according to the process flow described in section 3.1.1. The test wafer results indicate that adjustment of the polishing process time allows to tune the emitter saturation current J_{0e} and the emitter sheet resistance R_{sh} due to the etch back by the reactive gas phase which reduces the phosphorus

concentration near the front surface. Lifetime test samples, which are polished on both sides and subsequently cleaned with different cleaning sequences – pSC1, HF/HCl, HF-Dip or pSC1, HF/HCl, HF/O_3 – achieve effective lifetimes above 1 ms indicating an excellent surface passivation when using an Al_2O_3/SiN_x passivation layer stack. The polished rear sides of PERC solar cells, that applied similar cleaning sequences (pSC1, HF/HCl and pSC1, HF/O_3) confirm this result with effective SRVs at the rear of $S_{rear} < 40$ cm/s. The low J_{0e} values around 100 fA/cm^2 from the test wafer experiment however could not be reproduced, reducing the efficiency of the PERC cells cleaned with these cleaning sequences when compared with the PERC cells using an RCA clean.

We demonstrate on test wafers, that HF/O_3 terminated cleaning sequences such as pSC1, HF/HCl, HF/O_3 or HF/O_3 prior to Al_2O_3/SiN_x passivation result in effective lifetimes >1 ms and corresponding surface recombination velocities S_{pass} <15 cm/s. Accordingly, reference PERC solar cells applying these cleaning sequences show effective surface recombination velocities S_{rear} <50 cm/s. However, the highest reference PERC cell efficiency of 20.4% was obtained with the cleaning sequence pSC1, HF/HCl on an industrial batch-type cleaning tool which is comparable to PERC cells applying a laboratory type RCA clean. The lower performance of HF/O_3-based cleans for PERC cells when compared to pSC1, HF/HCl or RCA cleans results from an increase of surface recombination at the n^+-doped front surface, which is caused by a roughening on a nanometer scale during the HF/O_3 process step. This effect even occurs for short process times (1 min) and low ozone concentrations of 75 g/m^3.

5

Analysis and modeling of screen printed local Al contacts

In this chapter we analyze different aspects of screen printed local Al contacts. We measure the effective contact resistivity of the Al/Si interface and analyze the local BSF depth and contact geometry for PERC and PERC+ solar cells. The properties of voids are investigated and a new model for void formation is introduced.

5.1 Determination of the contact resistivity

As manufacturers improve aluminum pastes to form contacts with low surface recombination even for narrow LCOs the fraction of metallized area at the rear might further decrease in the future, possibly making the series resistance contribution of the contact resistance of the aluminum-silicon interface a noticeable power loss mechanism. Therefore knowledge of the specific contact resistivity ρ_c is required. Gatz et al. [123] used a variation of the rear contact pitch of PERC solar cells to determine ρ_c to $40 - 55$ mΩcm². However, for this approach the contribution of the bulk to the series resistance R_b needs to be acquired either by calculation or numerical simulation. Müller et al. [124] showed that the calculation of R_b according to the model of Plagwitz [125] as used in Ref. [123] leads to an underestimation of R_b und thus an overestimation of ρ_c. In this section we apply the method of rear contact pitch variation for PERC cells using R_b values acquired by simulation with Sentaurus Device. In addition we manufacture PERC-like test wafers to determine ρ_c using the transmission line method (TLM).

Experimental

For the PERC solar cells we use the process flow described in 3.1.1. The process for the PERC-like TLM samples is very similar to the one of the PERC solar cells. Until co-firing the only difference is an adapted LCO geometry for different

TLM samples on one wafer. Each sample includes different contact line pitches as indicated in Figure 5.1b). In order to evaluate a dependency of the contact resistivity on the contact line width, we process samples with LCO line widths of 28, 46, 64, 82 and 100 µm. The final contact, that is formed by the Al-Si alloying process, is about 40 µm wider than the LCO line width according to scanning electron microscopy (SEM) cross section images. After firing the contact lines are protected with an etch resistant hot melt wax printed with inkjet and subsequently separated from each other by a KOH Al-etch. After cleaning the different TLM samples are cut out of the wafer. Figure 5.1 schematically compares the PERC solar cells and the TLM samples.
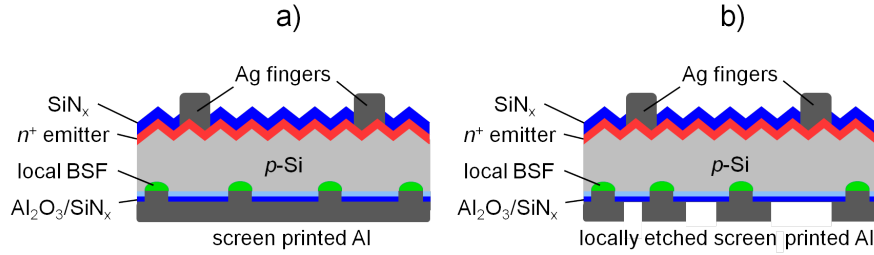

Figure 5.1: Schematic drawings of the investigated structures in this section: a) a PERC solar cell; b) a PERC-like TLM sample with isolated rear aluminum contact fingers.

Determination of ρ_c by varying the pitch of PERC solar cells

We vary the rear contact pitch p of PERC solar cells and measure the series resistance R_s in dependence of the inverse metallization fraction $1/f$ according to

$$R_s - R_b = \rho_c \cdot \frac{1}{f} + R_{const}, \tag{5.1}$$

where R_{const} summarizes the series resistance contributions that do not depend on the rear side metallization fraction (e.g. the front Ag finger grid). We need to acquire the series resistance of the bulk R_b in order to determine the contact resistivity ρ_c. Using a triple-light-level [126] simulation with Sentaurus device, we obtain the R_b values at the maximum power point of the solar cell as shown in Figure 5.2. The used simulation domain includes a fully contacted front side and therefore neglects the resistance contributions caused by lateral current flows through the emitter. However, this approach allows us to freely choose the rear contact pitch and keep the simulation domain at a manageable size. Figure 5.2 also compares the values obtained by simulation with those calculated according to the analytical model of Plagwitz [125], which is based on the calculation of the spreading resistance introduced by Gelmont et al. [127]. At pitches larger than 1500 µm the simulated values strongly exceed the calculated values according to Plagwitz, which were used in the analysis of Gatz et al. [123]. The values calculated according to
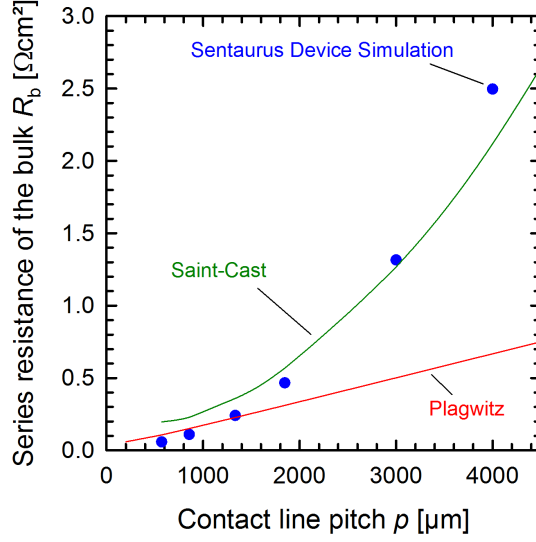
Figure 5.2: Contribution of the silicon bulk to the total series resistance R_b in dependence of the contact line pitch as determined by Sentaurus Device simulation (blue), the model of Plagwitz (red) and the model of Saint-Cast (green).

another analytical model introduced by Saint-Cast [77] (see equation 3.13) almost match the simulated values. A fit to the original data of Ref. [123], which includes R_b values according to the model of Plagwitz, strongly overestimates the specific contact resistivity $\rho_c = (55 \pm 5)\,\mathrm{m\Omega cm^2}$ as shown in Figure 5.3. Application of the numerically obtained values for R_b to equation 5.1 leads to a correction of this data with $R_s - R_b$ values following no clear trend. However, the corresponding fit results in $\rho_c = (-9 \pm 12)\,\mathrm{m\Omega cm^2}$, indicating a smaller value of ρ_c. Fig 5.3 also shows that evaluation with the Plagwitz model is only valid for small values of $^1/_f < 10$. A linear fit to the contact pitch variation of this work yields a contact resistivity of $\rho_c = (-0.9 \pm 1.1)\,\mathrm{m\Omega cm^2}$ as shown in Figure 5.4. Since the stated value for the uncertainty of ρ_c only accounts for the scattering of the data, we find a line with maximum slope within the error bars of all data points to derive an upper limit of $\rho_c < 5\,\mathrm{m\Omega cm^2}$.

Determination of ρ_c by TLM measurements

In addition to the measurements of PERC solar cells we measure the contact resistivity ρ_c in dependence of the contact line width applying the standard TLM at samples as shown in Figure 5.1b). Since the standard TLM evaluation assumes a thin conductive layer instead of a bulk of finite thickness, we expect our measurements to slightly overestimate the actual contact resistivity. The results for ρ_c (see Figure 5.5) show a trend towards larger scattering for narrower contact lines, which is probably due to the fact that the uncertainty of the contact line width translates into a relatively larger uncertainty of the area of the aluminum-silicon interface.
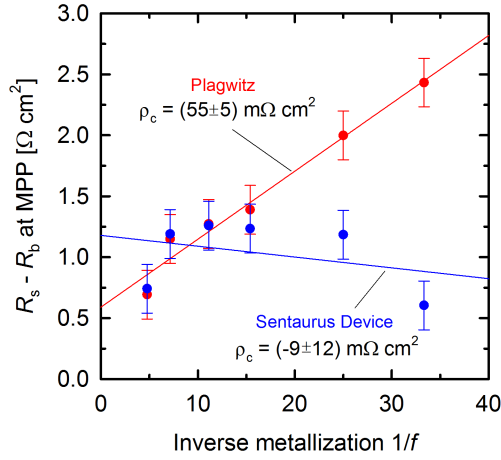
Figure 5.3: $R_s - R_b$ vs. inverse metallization fraction $^1/f$: The graph contains the original R_s-data of Ref. [123]. Red color indicates that the corresponding R_b values are obtained by calculation with the model of Plagwitz as used in Ref. [123], whereas blue color indicates that R_b is obtained by numerical simulation.
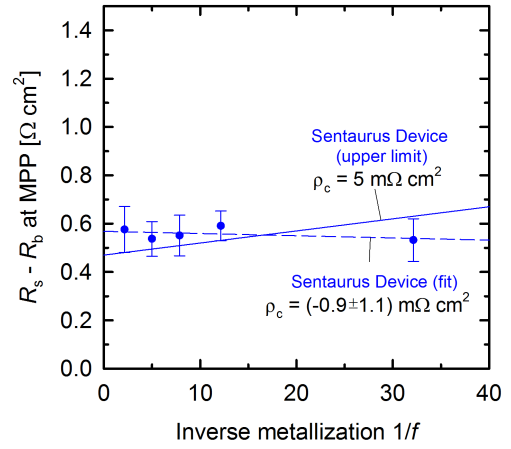
Figure 5.4: $R_s - R_b$ vs. inverse metallization fraction $^1/f$: The graph contains the data of this work. R_b-values are obtained by numerical simulation with Sentaurus Device. Since the mathematical fit results in a negative value for ρ_c an upper limit within the error bars is derived.

Figure 5.5: Specific contact resistivity ρ_c in dependence of the contact line width after firing as measured with the transmission line method (TLM). The plot shows a total of 61 measurements with 9-16 measurements per contact line width.

Furthermore we observe differences of the median values of the distributions for ρ_c when moving from one tested contact line width to the next. However, these shifts do not show any systematic behaviour, in contrast to the data reported by Urrejola et al. [128], wh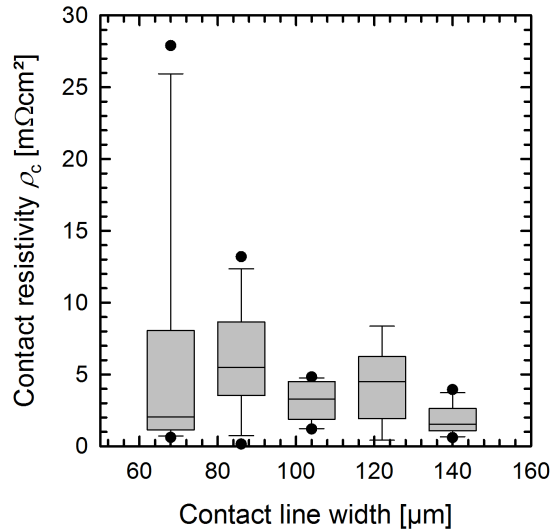o observed an increase of ρ_c from around $9\,\mathrm{m\Omega cm^2}$ to $17\,\mathrm{m\Omega cm^2}$ when moving from an LCO width of $80\,\mathrm{\mu m}$ to $170\,\mathrm{\mu m}$. With the median values for the single line widths being around or smaller than $5\,\mathrm{m\Omega cm^2}$ and an overall median value of $3\,\mathrm{m\Omega cm^2}$ the estimation $\rho_c < 5\,\mathrm{m\Omega cm^2}$ as derived from the solar cell analysis remains valid.

5.2 Modeling of local Al-BSF depths of PERC(+) solar cells

In this section we analyze and model the physical root cause of the different Al-BSF depths obtained with Al fingers versus full-area Al layers [75] and investigate the impact of different LCO line widths on the PERC and PERC+ solar cell performance.

Experimental

As mentioned before, PERC+ solar cells follow the same process flow as the reference PERC cells described in section 3.1.1. Therefore we just highlight the differences. The first difference arises during deposition of the $\mathrm{Al_2O_3/SiN_x}$ passivation layer stack on the rear. For PERC we choose a $\mathrm{SiN_x}$ capping layer thickness of $200\,\mathrm{nm}$. For PERC+ the same layer features a thickness of $80\,\mathrm{nm}$ to obtain improved anti-reflection properties when illuminated from the rear [75]. During the LCO process the PERC and PERC+ solar cells receive a line pattern of LCOs on the rear with a contact line pitch p for the PERC and $1.5p$ for the PERC+ solar cells [75]. For both solar cell types we apply different LCO line widths of 10, 35, 46, 100 and $150\,\mathrm{\mu m}$ while keeping the pitch constant for each solar cell type. We screen print a full-area Al layer for the PERC cells, whereas the PERC+ cells are printed with a 5 busbar H-pattern with an Al finger opening width of $100\,\mathrm{\mu m}$ aligned to the LCOs. For both solar cell types we use the same commercially available Al paste. We conclude the process flow by firing both solar cell types with their respective optimal set firing temperature T_{set} which is minimally lower for PERC+ compared with PERC.

Impact of voids on the Al-BSF depth

As shown in Figure 5.6, we determine the structure of the Al-Si contacts by scanning electron microscope (SEM) cross sections and assign the rear contacts to one of the following categories: a) completely filled contact, b) partial void and c) complete void. Refer to Figure 3.7 for a schematic drawing of a rectangular contact and its geometrical quantities as used throughout this work.

In order to do investigate the impact of voids on the Al-BSF depth, we dissect many PERC solar cells fabricated at SolarWorld Innovations (SWIN) technology
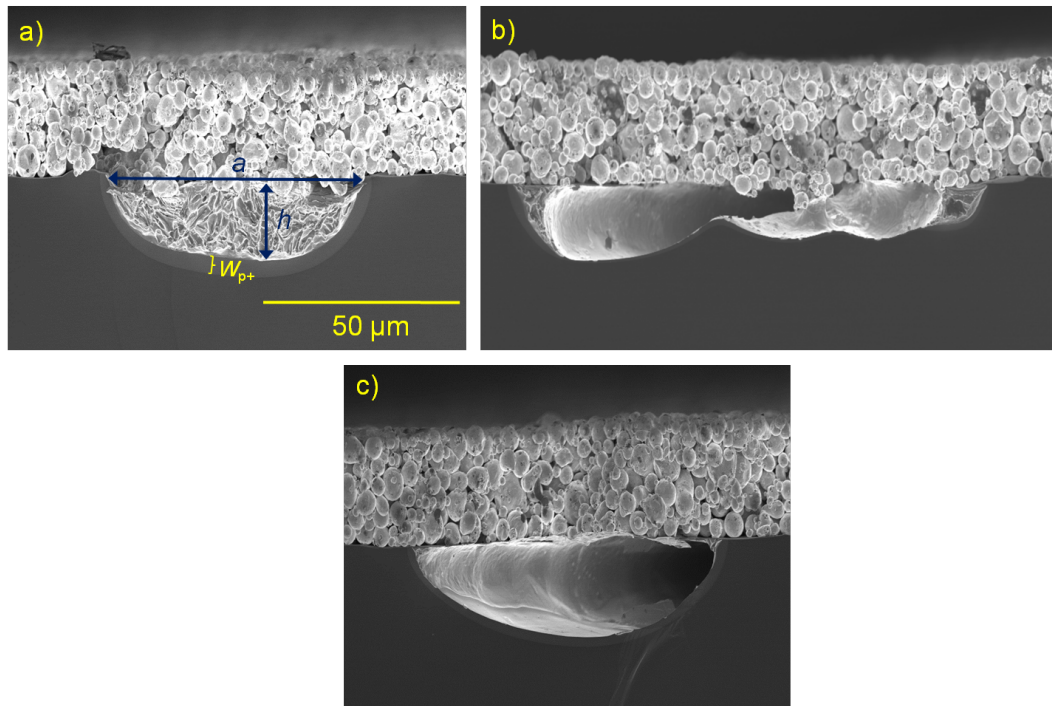
Figure 5.6: Exemplary SEM cross section images of different contact types: a) filled contact, b) partial void, c) complete void. In order to account for the 45° cleavage angle relative to the contact lines the x-axis are compressed by a factor of $1/\sqrt{2}$. The specific images are taken from PERC cells with an LCO width of 46 µm (a+c) and 100 µm (b). The scale of image a) applies to all images.

center [129] and measure the Al-BSF depth W_{p+} in the middle of the contact using SEM microscopy. We investigate 220 contacts and find 151 contacts including voids (complete or partial void) and 69 filled contacts. As shown in Figure 5.7 contacts afflicted with voids exhibit significantly reduced BSF depths with a median value of 1.8 µm compared to a median value of 2.5 µm for filled contacts. Also, the spread of data is increased for the void-afflicted contacts. We also investigate 31 contacts of PERC solar cells and 31 contacts of PERC+ solar cells fabricated at ISFH as shown in Figure 5.8. For PERC we find 3 filled contacts and 15 complete voids. Similar to the analysis of the SWIN cells we find deeper maximum Al-BSFs around 4–6 µm for filled contacts and partial voids compared to 2 µm for complete voids. For PERC+ we do not find any complete voids and BSF depths between 4 µm to 8 µm for the remaining 27 filled contacts and 4 partial voids. Figure 5.8 is generated from Figure 5.9a), but only considering contacts wider than 60 µm, where the influence of the alloying process on the Al-BSF depth is small.

The difference in BSF depth between filled contacts and voids is also represented by the images Figure 5.6a) and Figure 5.6c). It is even often observed within a single contact cross section as in Figure 5.6b), where areas with an Al-Si eutectic
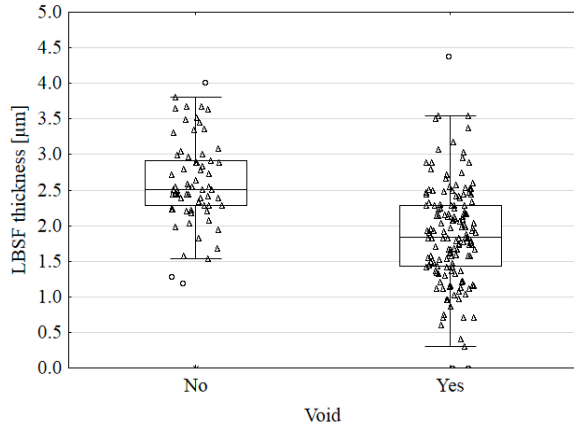
Figure 5.7: Al-BSF depth in the middle of a contact for PERC solar cells fabricated at Solar-World in dependence of the presence of a void. The overall number of contacts is 220, which split into 151 void-afflicted contacts and 69 filled contacts.
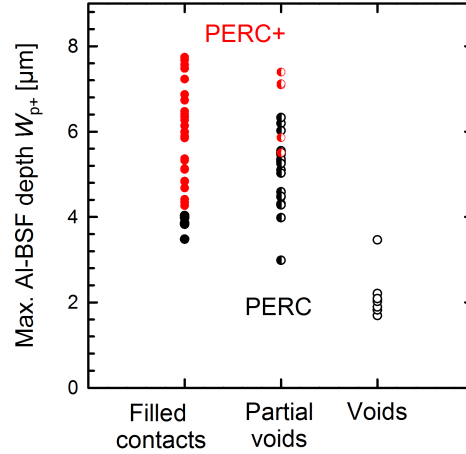

Figure 5.8: Maximum Al-BSF depths of 31 PERC (black) and 31 PERC+ (red) contacts. The plot is generated from Figure 5.9a), but only considering contacts wider than 60 µm.

underneath feature a deeper BSF compared to open Si surfaces. However, from Figure 5.7 and Figure 5.8 we read that even contacts afflicted with voids feature a nonzero BSF depth, which agrees well to the findings of Ref. [108, 113].

This observation is important in order to determine the point in time, when void formation occurs. Obviously, at some point during the cool down ramp of the firing process, when the crystallization of Si at the Si surface just begins, all silicon surfaces at the LCOs are still in contact with the Al-Si melt. The impact of the presence of voids on the BSF depth suggests that void formation occurs during this recrystallization process. At the time the Al-Si melt loses contact with the Si surface the recrystallization of Si at the corresponding surface is stopped causing the observed shallower Al-BSFs. The loss of contact is probably caused by an un-wetting process of the Al-Si melt as proposed in section 5.3.

Modeling of local Al-BSF depths

We measure the maximal Al-BSF depth W_{p+} of a contact in dependence of the final contact width a using SEM cross section images. The result is shown in Figure 5.9a). In case of PERC, we find Al-BSF depths of 4–6 µm for contacts wider than 80 µm. The Al-BSF depth strongly decreases for narrow contacts and we only find around 1 µm depth for contacts with a width of 45 µm. For PERC+ solar cells, we observe significantly deeper Al-BSFs especially in the currently relevant range for industrial production between 40 µm and 90 µm with a maximum value of 7.7 µm. For the narrowest contacts of 30 µm width, we still find an Al-BSF depth of 3 µm.

In order to apply the model by Müller et al. [102] presented in section 3.4.2, we carry out time dependent temperature measurements of solar cells during firing and determine the peak firing temperature to $T_{\text{peak}} = 760\,°C$ and the firing duration to $t_{\text{firing}} = 4.5\,s$ for both, PERC and PERC+. From Ref. [99] we read a solubility of Si in Al of $F = 25\%$ at a temperature of $760\,°C$. Furthermore, we measure the thickness of the screen printed Al-layer to $d = 30\,\mu m$. As mentioned above we expect void formation to be an overlying effect that leads to shallower BSFs and is not covered by the model. We therefore use different symbols in Figure 5.9a) to indicate the different contact types and only consider filled contacts for the fits. For a fit to the PERC data we use the model as described in section 3.4.2 and find good agreement for a choice of fit parameters of $\Delta = 60\,\mu m$ and $v_{\text{diss}} = 3.8\,\mu m/s$. The determined value for Δ agrees well to the $\Delta = 70\,\mu m$ reported in Ref. [102]. The value for v_{diss} is more than twice as high compared to $v_{\text{diss}} = 1.6\,\mu m/s$ as reported in Ref. [102]. This is most probably due to the difference in measured firing duration t_{firing} between $4.5\,s$ (this work) and $10\,s$ (Ref. [102]). From equation 3.18 we note, that we obtain identical BSF depths for every choice of constant $v_{\text{diss}} \cdot t_{\text{firing}}$.
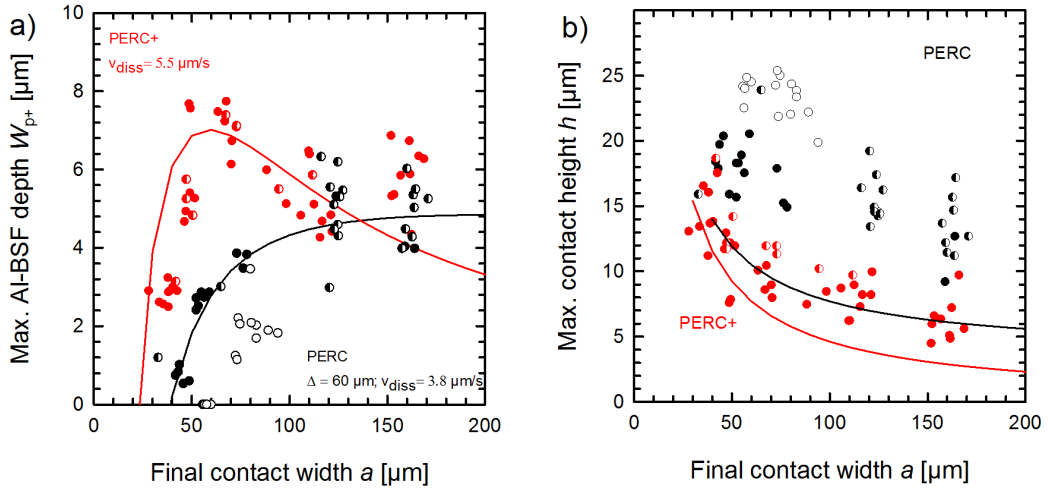
Figure 5.9: a) Maximal BSF depth at a contact in dependence of the final contact width for PERC (black) and PERC+ (red). The solid lines represent fits of the corresponding contact formation model (see text) to the data. b) Maximal contact height in dependence of the contact width. The lines represent calculated values that make use of the fit parameters determined in a). The symbols in both graphs indicate the type of the contact: filled contacts (closed symbols), partial voids (semi-filled symbols) and complete voids (open symbols).

For PERC+ solar cells the Al fingers confine the diffusion of Si and we choose to modify the model described in section 3.4.2. We define a new Al mass per contact base area

$$\frac{m_{\text{Al}}}{A} = \frac{A_{\text{Al}-\text{finger}}\rho^*_{\text{Al}}}{a}, \tag{5.2}$$

where $A_{\text{Al-finger}} = 3900\,\mu\text{m}^2$ is the measured cross sectional area of an Al finger. Equation 5.2 replaces equation 3.19 of the original model and consequently removes Δ as a fit parameter. With the only remaining fit parameter set to $v_{\text{diss}} = 1.6\,\mu\text{m/s}$, we find good agreement of the modified model and the PERC+ data. In particular the model well describes the observed optimum BSF depth at a contact width of $50\,\mu\text{m}$. The difference between model and experimental data for very wide PERC+ contacts of $150\,\mu\text{m}$ is probably due to inhomogeneities within the LCO area. For these contacts we frequently observe areas with neither eutectic nor Al-BSF in the middle of the LCO area. The fit results indicate that the obtained different Al-BSF depths for PERC and PERC+ can be described by the different Al mass printed to the rear side of the solar cells.

Figure 5.9b) shows the measured maximum contact height h in dependence of the final contact width. It is observed that PERC+ Al contacts achieve heights between 5–15 μm, whereas the PERC contacts are almost twice as high with values between 15 and 30 μm. Furthermore, there is a clear trend towards higher contacts for narrower lines for both solar cell concepts. We further extend the original BSF-formation model to calculate contact heights. In analogy to equation 3.17 we can calculate the height of the contact

$$h = \frac{m_{\text{Al}}}{A\rho_{\text{Si}}} \left(\frac{E}{1-E} \right). \tag{5.3}$$

for all cases, where $c_{\text{Si}}(t_{\text{firing}})$ reaches at least the eutectic concentration (and thus the BSF depth $W_{\text{p+}}$ is non-zero). Please note, that this approach includes no additional fitting and, in case of PERC, only re-uses the previously obtained value for Δ. The calculated values for h are clearly below the measured values. However, the slope of both data sets is reasonably well described. The discrepancy between experimental and modeled contact height indicates that experimentally more Si is dissolved in the Al paste than required for eutectic and Al-BSF formation as predicted by the model. From Figure 5.9b) we also note, that voids almost only occur for contacts with a height of $20\,\mu$m and above. This relation is described by a model for void formation presented in section 5.3.

From Figure 5.9a) we observe clustered data points, where each cluster represents a group of contacts with the same LCO width. We also observe, that the PERC clusters are shifted towards wider contacts, when compared to the PERC+ data. For example, application of an LCO width of $10\,\mu$m results in PERC contacts with an average final contact width a of $39\,\mu$m, whereas the corresponding PERC+ contacts exhibit an average width of $27\,\mu$m. From the measured heights we are able to understand the differences in final contact width at identical LCO width: Due to the smaller Al-volume printed on the rear side of the PERC+ cells the Si concentration saturates faster, leading to a faster decline of the Si dissolution process when compared to PERC. Therefore PERC+ contacts are on average $6\,\mu$m shallower for a given LCO width (compare Figure 5.9b). Assuming that the dissolution of Si is naturally not a directed but an isotropic process, we would

expect a difference in contact widening of 6 μm between PERC and PERC+ for both contact edges. The expected offset in contact width of 12 μm agrees well to our data, where the average final contact widths range from 49 μm to 162 μm for PERC and 37 μm to 150 μm for PERC+.

In order to measure the resulting silicon concentrations directly we carry out energy-dispersive x-ray spectroscopy (EDX) mappings. Figure 5.10 shows the silicon signal of a PERC and PERC+ rear contact in yellow color. Figure 5.11 shows a line scan in the Al layer of the PERC contact of Figure 5.10a) and reveals a gradient in the silicon concentration from $(15 \pm 3)\%$ directly above the contact to $(4 \pm 2)\%$ in a distance of 300 μm. These values are very similar to those reported in Ref. [100].
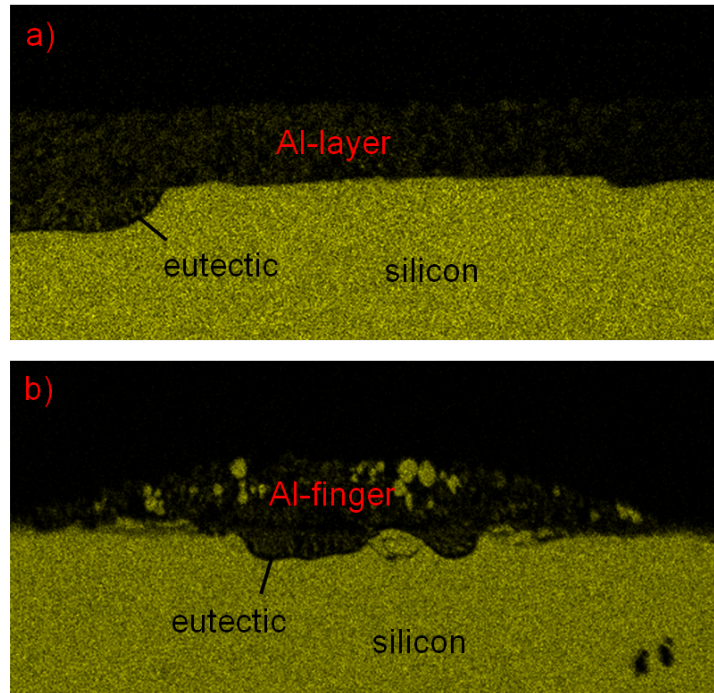
Figure 5.10: EDX images displaying the color coded silicon signal of an Al contact of a PERC (a) and a PERC+ (b) solar cell. In contrast to PERC the PERC+ cells shows silicon precipitations in the Al paste with a grain size of up to 5 μm.

The model assumes that the whole silicon in the Al paste beyond the solubility of 12% migrates to the Al-Si interface, which is obviously not the case due to the strong non-equilibrium conditions during cooldown. According to equation 3.17 the measured offset in concentration of 3% already explains around 4 μm of the offset in height as shown in Figure 5.9b) as it represents silicon dissolved from the wafer, but not contributing to the Al-BSF formation. As shown in Figure 5.10b) the PERC+ cells possess grains with a diameter of up to 5 μm of almost pure silicon ($c > 97\%$) in the Al paste. In the remaining volume we determine a silicon concentration of $(15 \pm 3)\%$, matching the value for the near-contact concentration of the PERC

Figure 5.11: EDX-measured silicon concentration of the Al-layer of Figure 5.10a). The vertical dashed line indicates the edge of the contact. The red line indicates the 12% eutectic concentration as assumed by the model as well as the fit result $\Delta = 60\,\mu\text{m}$.

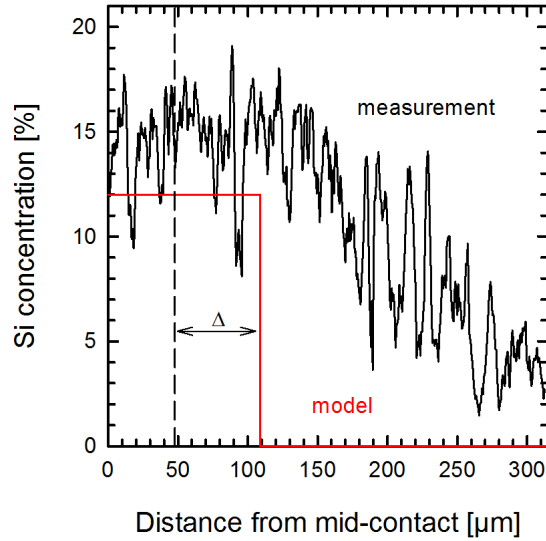cells. The averaged Si concentration over the hole cross section of the Al-finger is $(31 \pm 5)\%$. Apparently, in case of PERC+ the higher Si concentration during the firing process leads to "spontaneous" recrystallization inside the Al-finger. We speculate that this process occurs at elevated temperatures, where diffusion is still enabled and allows the silicon to move to the locations of crystallization and form the observed grains. At lower temperatures during the cooldown ramp diffusion might be suppressed leading to silicon precipitating at its current position and causing the homogeneous 15% concentration in the Al-paste for both, PERC and PERC+ solar cells. For comparison we use the fit results and equation 3.18 to calculate values for $c_{\text{Si}}(t_{\text{firing}})$ of 17% and 21% for the PERC and PERC+ contact, respectively.

IV results

The efficiencies of the PERC and PERC+ cells of this study as measured on a brass chuck are shown in Figure 5.12. The PERC solar cells achieve best efficiencies up to 21.2% for a contact width of 81 μm. For narrower contact lines the efficiency strongly decreases to values around 19.5% at 49 μm width due to increased rear contact recombination caused by shallow Al-BSF depths. In contrast, the PERC+ cells allow for deep Al-BSFs and hence low contact recombination even for narrow contact lines. This leads to a best efficiency of 21.1% at a contact line width of 48 μm. The lower efficiencies of PERC+ cells with very wide contacts above 100 μm

are partly caused by an imperfect alignment of the screen printed Al fingers to the LCOs.
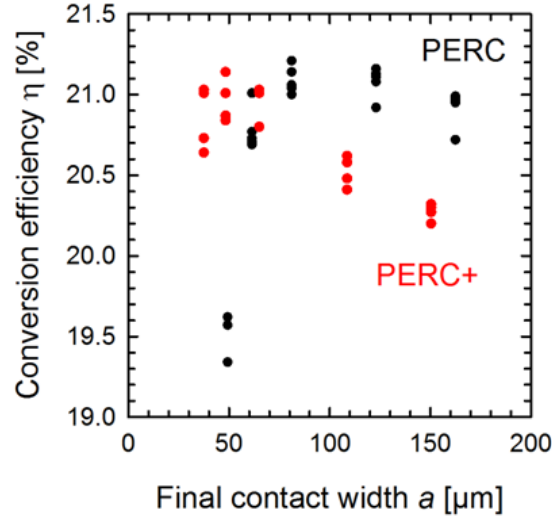

Figure 5.12: Energy conversion efficiencies of PERC (black) and PERC+ (red) solar cells for different widths of the line shaped local rear contacts. The values represent in-house measurements on a brass chuck for both solar cell types.

PERC cell manufacturers generally prefer narrow contact lines due to fewer laser spots and thus higher throughput of the LCO process. For PERC cells applying full area screen printing it is therefore necessary to trade throughput versus improved contact properties. This work demonstrates that bifacial PERC+ cells – in addition to the advantages of bifaciality and reduced Al paste consumption – can potentially combine a high throughput LCO process with low Al contact recombination by achieving narrow Al contact lines with deep Al-BSFs.

5.3 Void formation modeled by surface energy minimization

So far, the Kirkendall effect [114] has been proposed as root cause for the formation of voids in local Al-Si contacts. The Kirkendall effect describes the interdiffusion of two solid metals with different diffusion coefficients into each other. In such a system a net diffusion of lattice vacancies from the material with the lower diffusion coefficient into the material with the higher diffusion coefficient occurs. These vacancies can accumulate and form the so-called Kirkendall-pores [130]. This mechanism of void formation would start from the beginning of the firing process and hence during cool down there would be no Al-Si melt being in contact with the silicon interface and hence no Al-BSF could epitaxially re-grow. However, from section 5.2 we learned that voids generally exhibit shallow Al-BSFs and therefore void formation probably occurs during Al-BSF growth. Additionally, a mechanism

based on vacancy interdiffusion of solids is not applicable to our system, where one participant is the liquid Al-Si melt. Both circumstances contradict the Kirkendall effect to be the root cause of void formation. Hence, this section introduces a new model of void formation that is based on surface energy minimization of the liquid Al-Si melt (which will be called the Al melt in the following).

The surface energy σ of a body can be considered as the "energy required to create one unit of surface area" and thus allows assigning an energy E to a certain surface area A:

$$E = \sigma A. \tag{5.4}$$

In case of liquids, σ is often called surface tension. We schematically draw a contact for different points in time during firing as shown in Figure 5.13. During the time steps t_1–t_4 the Al melts and dissolves silicon from the wafer surface increasing the Si concentration in the Al melt. At t_5 BSF growth has just started. At this point we allow for two possible configurations of the Al melt: the filled contact where the Al melt is in contact with the silicon surface and a complete void where the Al melt is located in-between the Al particles and their surface consisting primarily of aluminum oxide [131, 132]. So far, there are little experimental indications on where the Al melt is located in case of a void. It appears reasonable to assume that during cool down some of the Al melt is transported back to the inside of the aluminum oxide shells, where it originated from. The additional material, however, which results from the dissolution of Si might wet the outside of the aluminum oxide shells. In order to indicate this potential wetting from the outside we schematically draw the Al melt continuously in-between the aluminum oxide shells. From the SEM images in Fig. 1, however, we notice that the screen printed paste is not a compact layer after firing. Großer et al. [133] identified a comparably dense interfacial layer at the surface of the Al paste layer facing the void. This interfacial layer probably contributes to the disposition of the Al melt, although it only exhibits a thickness of 25 nm.

From Figure 5.13 we are now able to state the total surface energy of both configurations at the time t_5. In case of the filled contact, we obtain

$$E_1 = \sigma_{\mathrm{Si,Al}} A_{\mathrm{Si}} + \sigma_{\mathrm{Al}} A_{\mathrm{Al}} + \sigma_{\mathrm{sh}} A_{\mathrm{sh}} + \sigma_{\mathrm{sh,Al}} A_{\mathrm{sh,Al}} \tag{5.5}$$

with $\sigma_{\mathrm{Si,Al}}$, σ_{Al}, σ_{sh} and $\sigma_{\mathrm{sh,Al}}$ as the surface energies of the Si-Al interface, the Al melt, the aluminum-oxide shells and the shell-Al interface, respectively. Accordingly, A_{Si}, A_{Al}, A_{sh} and $A_{\mathrm{sh,Al}}$ are the surface areas of the Si trench, the Al melt, the aluminum-oxide shells and the shell-Al interface. In case of voids we obtain

$$E_2 = \sigma_{\mathrm{Si}} A_{\mathrm{Si}} + \sigma_{\mathrm{Al}} A'_{\mathrm{Al}} + \sigma_{\mathrm{sh}} A'_{\mathrm{sh}} + \sigma_{\mathrm{sh,Al}} A'_{\mathrm{sh,Al}} \tag{5.6}$$

with σ_{Si} as the surface energy of silicon. Dashes indicate that in the void configuration the corresponding surface areas are in general different to the ones of the filled contact configuration. From the two possible scenarios described above, the
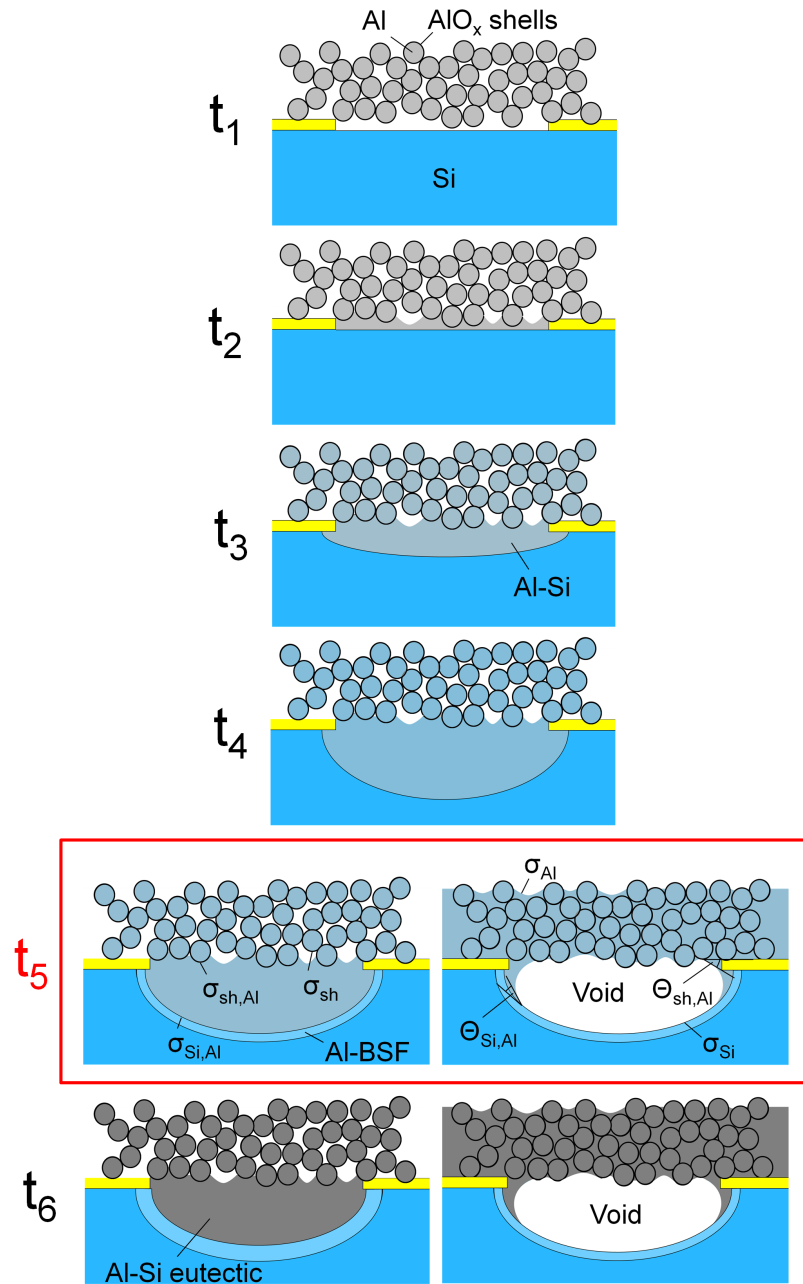
Figure 5.13: Schematic drawing of a contact at different points in time (t_x) during firing: t_1 – before firing, t_2 – Al melts, t_3 – Si dissolution begins, t_4 – Si dissolution continues, t_5 – two possible configurations of the Al melt shortly after BSF growth has started, t_6 – contact geometries after solidification. In case of a filled contact, the BSF growth continued before solidification leading to a deeper BSF. The different colorings of the Al melt indicate different Si concentrations.

Al melt favors the configuration with the lower total surface energy. Therefore, we calculate the difference

$$\Delta E = E_2 - E_1 = (\sigma_{\text{Si}} - \sigma_{\text{Si,Al}})A_{\text{Si}} + \sigma_{\text{Al}}\Delta A_{\text{Al}} + \sigma_{\text{sh}}\Delta A_{\text{sh}} + \sigma_{\text{sh,Al}}\Delta A_{\text{sh,Al}}, \quad (5.7)$$

where the surface areas marked with a delta denominate the difference between the quantities with and without a dash but the same index. We neglect a potential increase of the Al particle diameter due to wetting of the surface during firing and instead assume a constant total surface area of the aluminum oxide shells, which leads to $\Delta A_{\text{sh}} = -\Delta A_{\text{sh,Al}}$ and reduces equation 5.7 to:

$$\Delta E = (\sigma_{\text{Si}} - \sigma_{\text{Si,Al}})A_{\text{Si}} + \sigma_{\text{Al}}\Delta A_{\text{Al}} + (\sigma_{\text{sh}} - \sigma_{\text{sh,Al}})\Delta A_{\text{sh}}. \quad (5.8)$$

The Al melt favors the filled contact configuration if $\Delta E > 0$. Thus, it might be instructional to discuss the signs of the different summands, before analyzing geometrical effects. The second summand is the easiest to discuss. As a comparison of the two configurations at t_5 indicates the surface area of the Al melt is larger in the void configuration due to the additional surface area at the bottom of the melt, making ΔA_{Al} as wells as the second summand in equation 5.8 positive (surface energies are always positive). To discuss the other contributions, we use Young's equation

$$\cos\Theta = \frac{\sigma_{\text{Si}} - \sigma_{\text{Si,Al}}}{\sigma_{\text{Al}}} \quad (5.9)$$

which puts the stated surface energies in relation to the contact angle Θ that is formed, e.g., when a droplet of liquid aluminum is located on a silicon surface. From this equation we read, that in case of an acute angle $\Theta < 90°$, the term in brackets must be positive, or $\sigma_{\text{Si}} > \sigma_{\text{Si,Al}}$. Thus, in this case, wetting the surface is favorable in terms of energy. Similarly, obtuse angles of $\Theta > 90°$ indicate that wetting the surface is unfavorable. From SEM cross section images of partial voids as shown in Figure 5.6b), we read, that the angle at the Al-Si interface $\Theta_{\text{Si,Al}}$ (compare Figure 5.13) is always $< 90°$ as can be seen for the eutectic layer at the contact edge. From the same image we also observe acute contact angles of the Al melt to the screen printed layer of aluminum oxide shells $\Theta_{\text{sh,Al}}$. Thus, both terms in brackets in equation 5.8 are positive, indicating that the Al melt possesses a tendency to wet both, the silicon surface and the aluminum-oxide shells. Finally, a comparison of the two configuration at t_5 indicates that ΔA_{sh} is negative, as the surface area of the aluminum-oxide shells that is not wetted, is smaller in the void configuration. This concludes our analysis of signs, leaving the first two summands in equation 5.8 with positive and the third summand with negative sign. Since we only observe filled contacts in case of $\Delta E > 0$, this means, that both, the wetting of the silicon surface and the avoidance of Al melt surface, are the driving forces towards the configuration of a filled contact. On the other hand, the tendency of wetting the aluminum oxide shells functions as a driving force towards the void

configuration. One might think of the aluminum oxide layer as a "sponge", which has a strong tendency to be wetted by the Al melt due to its large surface area.

In order to analyze geometric effects in a simple way, we assume rectangular shaped contacts:

$$A_{\text{Si}} = (a + 2h)l \tag{5.10}$$

with a as contact width, h as contact height (see Figure 5.13) and l as the length of the contact line. Also, in a first approximation ΔA_{Al} is considered to be the lower Al surface in the void schematic at t_5:

$$\Delta A_{\text{Al}} = al. \tag{5.11}$$

As discussed above the Al melt does not fill the complete volume in-between the aluminum oxide shells in reality. This probably leads to a further surface enhancement of the Al melt when comparing the filled contact and void configuration. This surface enhancement should be proportional to the contact area: $\Delta A_{\text{Al}} = (1 + s_{\text{enh}})al$. However, as a first approximation we use equation 5.11. Finally, for the screen printed layer of aluminum-oxide shells, we define a geometric ratio

$$k(V_{\text{Al}}) = \frac{dA_{\text{sh}}}{dV_{\text{Al}}} \tag{5.12}$$

which includes the surface area dA_{sh} of aluminum-oxide shells, that is wetted, when a volume of Al melt dV_{Al} from the filled contact configuration is added to the aluminum-oxide shell layer. This wetting can in principle take place at the inside or the outside of the aluminum oxide shells. In case of a large, perfectly homogeneous layer $k(V_{\text{Al}}) = k$ should be constant. As the volume $V_{\text{Al}} = ahl$ is known for the filled contact configuration, equation 5.8 can now be written in its rectangular geometry approximation:

$$\Delta E = (\sigma_{\text{Si}} - \sigma_{\text{Si,Al}})(a + 2h)l + \sigma_{\text{Al}}al + (\sigma_{\text{sh}} - \sigma_{\text{sh,Al}})kahl. \tag{5.13}$$

We use the abbreviations $(\sigma_{\text{x}} - \sigma_{\text{x,Al}}) = \Delta\sigma_{\text{x}}$ and write equation 5.13 for the two-dimensional situation as depicted in Figure 5.13 by dividing equation 5.13 by l:

$$\frac{\Delta E}{l} = (2\Delta\sigma_{\text{Si}} - \Delta\sigma_{\text{sh}}ka)h + \sigma_{\text{Al}}a + \Delta\sigma_{\text{Si}}a. \tag{5.14}$$

which, for a given contact width a, is a function of the contact height h. From literature, we read $\sigma_{\text{Al}} = 0.865\,\text{N/m}$ for liquid aluminum at a temperature around $953\,\text{K}$ [134] and $\sigma_{\text{Si}} = 1.41\,\text{N/m}$ for a (100) surface and $\sigma_{\text{Si}} = 1.36\,\text{N/m}$ for a (111) surface of silicon [135]. We therefore use $\sigma_{\text{Si}} = 1.4\,\text{N/m}$. We estimate a contact angle of $\Theta_{\text{Si,Al}} = 20\,° \pm 10\,°$ from Figure 5.6b), which translates into $\sigma_{\text{Si,Al}} = 0.58\,\text{N/m}$ according to Young's equation 5.9. This again yields $\Delta\sigma_{\text{Si}} = 0.82\,\text{N/m}$ and leaves $\Delta\sigma_{\text{sh}}k$ as the only unknown parameter in equation 5.14. Figure 5.14 shows $\Delta E/l$ as calculated by equation 5.14 for a contact width a of $60\,\mu\text{m}$ and
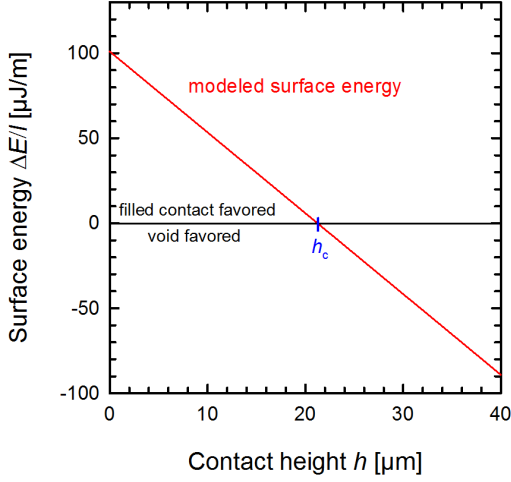
Figure 5.14: Surface energy $\Delta E/l$ according to equation 5.14 for a contact width a of $60\,\mu\text{m}$ in dependence of the contact height h. The critical height h_c is defined as the height where the surface energy ΔE changes from positive to negative values and hence where voids are energetically more favorable than filled contacts.
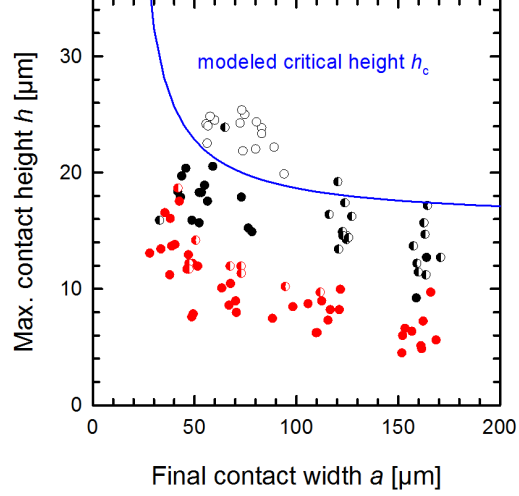

Figure 5.15: Critical height h_c according to equation 5.15 in dependence of the contact width a. The data points represent measured local contacts of PERC (black) and PERC+ (red) solar cells. The symbol shape indicates the contact type: filled contacts (filled symbols), partial voids (semi-filled symbols) and complete voids (open symbols).

$\Delta\sigma_\text{sh}k = 0.107\,\text{N}/(\text{m}\cdot\mu\text{m})$ (the reason for this value will become apparent soon). For small contact heights h, we see that $\Delta E/l > 0$ and thus the filled contact configuration is favored. With increasing height the energy $\Delta E/l$ decreases until the void configuration is favored for $\Delta E/l < 0$. Apparently, at a certain height, it is more favorable for the Al melt, which is "stored" in the filled contact configuration, to wet the aluminum-oxide shells of the Al paste and in turn release the silicon surface. We call the height, where $\Delta E/l = 0$ and hence neither of the configurations is favored, the critical height h_c. It can be calculated, when equation 5.14 equals zero:

$$h_\text{c} = \frac{-(\sigma_\text{Al} + \Delta\sigma_\text{Si})}{\frac{2\Delta\sigma_\text{Si}}{a} - \Delta\sigma_\text{sh}k}. \tag{5.15}$$

The critical height h_c is shown in Figure 5.15 as a function of the final contact width a after firing. It strongly increases for narrow contact lines since then the contact trenches act as a capillary tube. Figure 5.15 also shows measured maximum contact heights of local contacts in dependence of a, as determined from the variation of LCO line widths of PERC and PERC+ solar cells described in section 5.2 (compare Figure 5.9b). The symbol shape of the experimental data again indicates the type of the local contact using the same categorization as in Figure 5.6. We observe, that complete voids only emerge from contacts with a height above $20\,\mu\text{m}$. For a

choice of $\Delta\sigma_{\text{sh}}k = 0.107\,\text{N}/(\text{m}\cdot\text{µm})$ as the only fit parameter, the critical height as calculated from equation 5.15 nicely separates the void afflicted PERC contacts from the filled PERC contacts in the range between $40\,\text{µm}$ and $90\,\text{µm}$, which is the currently relevant range for industrial-type rear contacts. Please note that the approximately $7\,\text{µm}$ difference in contact height between voided and filled contacts in Figure 5.15 is not due to the different Al-BSF depths, which account for only $2\,\text{µm}$ contact height difference as displayed in Figure 5.9. The physical reason, why a void is formed, is, that for large contact heights in case of filled contacts only a relatively small portion of the Al-Si melt wets the Si surface, whereas in the void case a large portion of the Al-Si melt wets a large surface area of aluminum oxide shells making this case energetically favorable.

Contacts with a width of more than $100\,\text{µm}$ exhibit a very inhomogeneous morphology and generally contain partial voids (compare Figure 5.6b). We expect our simplified rectangular geometry to be less accurate for these contacts. PERC+ contacts exhibit smaller heights compared to PERC and therefore we do not find a single complete void among the 50 PERC+ contacts investigated. However, we find a few partial voids for PERC+ which feature a thick eutectic layer and BSF at the entire silicon surface. For PERC+ the volume of Al-Si melt V_{Al} is comparable to PERC, but the amount of Al paste and thus aluminum oxide shells is strongly reduced by one order of magnitude. Therefore in case of PERC+ it might be possible, that the Al-Si melt can wet both, the entire silicon and the entire aluminum-oxide shell surface, by only forming a small cavity in the middle of the contact. Such an interstitial state between void and filled contact, however, is not covered by this model.

As described in section 5.2 and indicated by Figure 5.13, we expect all contacts to be initially filled during firing and void formation to occur at some point during cool down. At this time the contact height actually decreases and the contact growth itself cannot be the root cause of void formation. Instead the critical height h_{c} probably decreases during cool down. We speculate that the temperature dependencies of the participating surface energies in equation 5.15 might cause this change. Also, the geometry parameter $k(V_{\text{Al}})$ might not be constant but dependent of the Al volume V_{Al}. The thermal contraction of the Al melt during cool down thus possibly contributes to a decreasing h_{c}.

Comparison with fired PVD-Al contacts

The proposed model for void formation suggests that the aluminum oxide shells provide the driving force towards the void configuration of the Al melt. Hence, without these shells we expect a reduced amount of voids or no voids at all. In order to test this assumption we prepare special samples, which use physical vapor deposited (PVD) Al instead of screen printed Al on the rear side.

The samples are planar Cz-Si wafers with a $200\,\text{nm}$ thick PECVD-SiN$_{\text{x}}$ deposited on the rear side. Line shaped LCOs with a width of $64\,\text{µm}$ are then used to locally

ablate the SiN$_x$. We deposit the PVD-Al on the rear side with a final layer thickness of 20 μm. The three samples are fired at set peak temperatures of 870 °C, 900 °C and 950 °C using the same firing profile as for PERC solar cells. We dissect the samples for cross sectional SEM imaging.

Figure 5.16 shows exemplary panorama images – each consisting of different SEM images – of the two samples fired at a temperature of 870 °C and 950 °C. In case of 870 °C (Figure 5.16a) we observe a homogeneous Al layer of ~20 μm thickness on top of the wafer. For higher temperatures the Al layer becomes increasingly inhomogeneous and we measure local thicknesses between 5 μm and 50 μm for the sample fired at 950 °C. The highest thickness is generally observed in the middle of two contact lines (see Figure 5.16b). These "hills" are visible with the naked eye as droplet shaped structures arranged along lines in between the LCOs. Probably, as temperature increases and the viscosity of the liquid Al decreases, the Al melt starts to form droplets in order to reduce its surface and surface energy.

We observe several small voids within the PVD-Al layer. These voids appear to be different in nature when compared to the voids known from the contacts of screen printed Al due to two observations:

1. The voids exhibit an oval or even spherical shape with a diameter of several micrometers (see Figure 5.17). The voids of screen printed contacts are actually channels with typically millimeters or centimeters in length [106], which is the reason why the end of a void is generally not visible in SEM cross section images.

2. Voids can be found within the Al-Si eutectic of a contact and in the Al layer in the passivated unopened areas. From the SEM images it appears that the voids favor areas where the Al layer is thick, which are the contacts and in case of higher firing temperatures the areas in the middle of two contact lines (see e.g. Figure 5.16b). For screen printed Al voids are only observed in the contact areas and not in the passivated areas.

Similar to the analysis of screen printed contacts, we categorize 67 contact cross sections of the three samples and find 30 filled contacts and 37 contacts partially afflicted by voids. Among these contacts, we do not find any "complete void" as there is always some solid eutectic present in the volume of the Si trenches and most of the Si surface is in contact with it. Figure 5.18a)-c) shows measured widths and heights of contacts of all three samples and compares them to the results of screen printed Al contacts of PERC solar cells. For a peak firing temperature of 870 °C, which is close to the peak firing temperature of PERC cells, the contact widths and heights are comparable to those PERC contacts applying the same LCO width. Both quantities increase with increasing firing temperature due to the higher solubility of Si at elevated temperatures and therefore enhanced Si dissolution. However, we do not observe a systematic trend of the contact type in dependence of the width, height or firing temperature. The voids appear to be
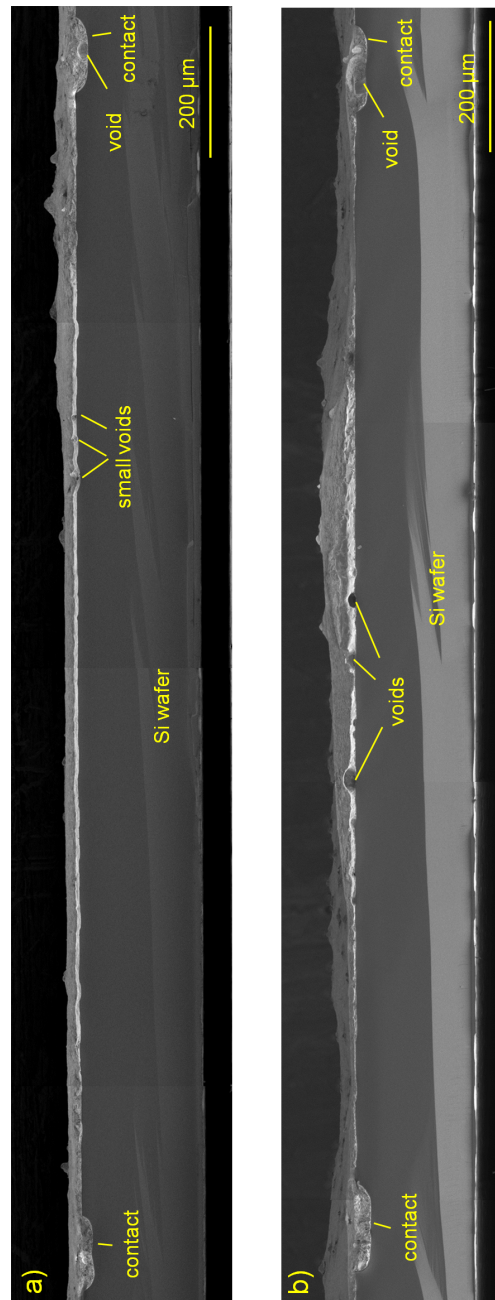
Figure 5.16: Panorama SEM cross section images of two samples with PVD-Al after firing. The displayed samples are fired at a temperature of $870\,^\circ$C(a) and $950\,^\circ$C(b). The images indicate the increasingly inhomogeneous Al layer thickness in case of higher firing temperatures and the postion of the largest voids found for both samples.
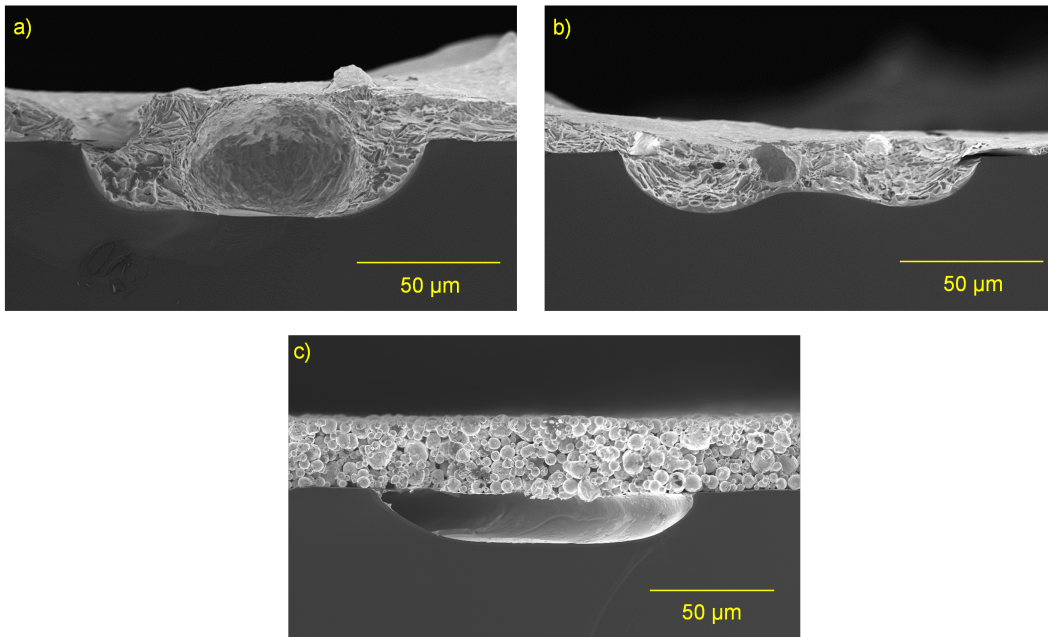
Figure 5.17: Exemplary SEM cross section images of two PVD-Al contacts afflicted by almost spherical voids (a+b). In contrast to the voids of screen printed Al contacts (c) the "Al rear side" is easily visible. Images a) and b) are taken from the sample fired at a temperature of 950 °C.

rather randomly distributed within the PVD-Al layer. In particular there is no critical height that separates filled contacts from contacts with cavities.

We speculate that the root cause of void formation in case of PVD-Al is a solidification process during cool down that begins at the surface of the Al melt. The liquid Al melt within the resulting hull is possibly redistributed as thermal contraction reduces the volume of the melt. As calculated in Ref. [132] an Al-Si alloy at eutectic concentration increases its volume by 10.2% during melting.

Void formation for PVD-Al and screen printed Al might have in parts a common root cause. However, the comparison above shows that the presence of the aluminum oxide shells in case of screen printed Al strongly enhances void formation for high contacts as predicted by the model.
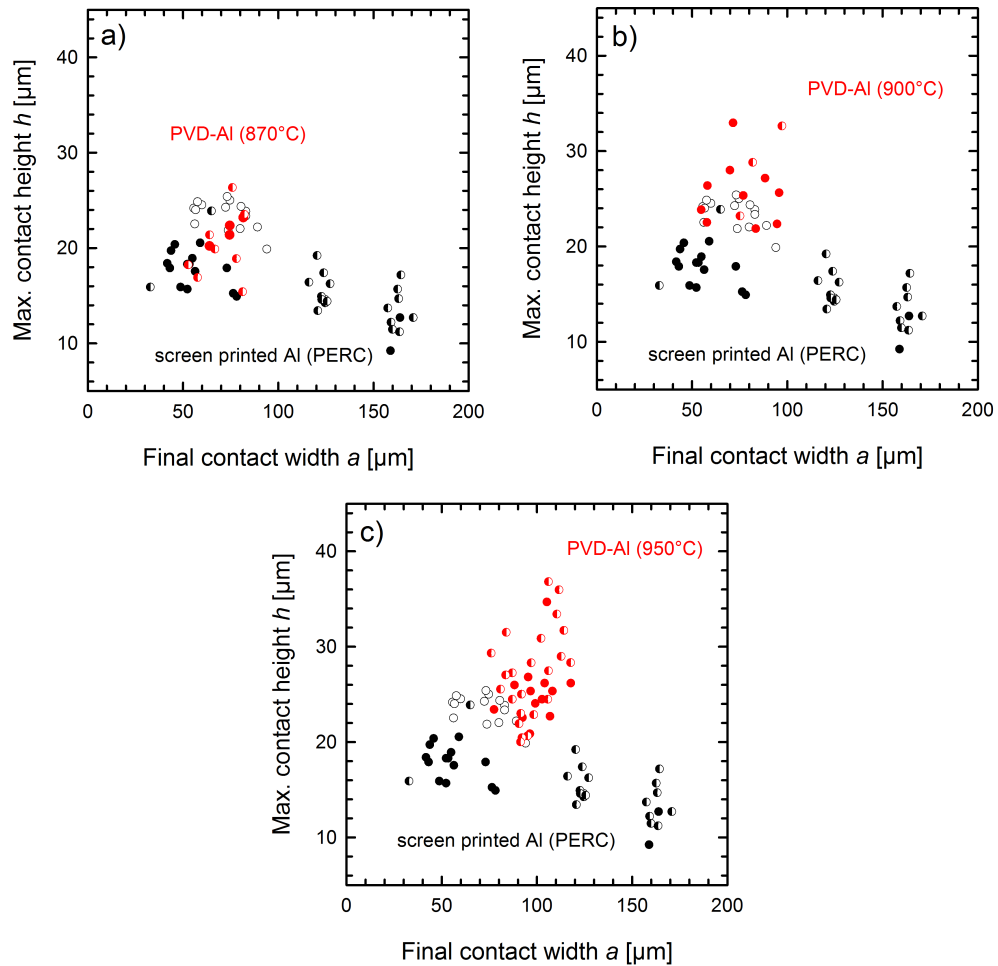
Figure 5.18: Measured heights and widths of PVD-Al contacts (red) in comparison to the results of screen printed Al contacts of PERC solar cells (black) from the previous section. The symbols indicate the contact type: filled contacts (closed symbols), partial voids (semi-filled symbols) and complete voids (open symbols). The results are shown for three different firing temperatures of the PVD-Al samples: 870 °C(a), 900 °C(b), 950 °C(c).

5.4 Chapter summary

We processed PERC solar cells and PERC-like TLM samples in order to measure the specific contact resistivity ρ_c of line-shaped screen printed Al contacts via contact pitch variation and TLM, respectively. A fit to the solar cell data yielded a small value of $\rho_c = (-0.9 \pm 1.1)\,\text{m}\Omega\text{cm}^2$, whereas the TLM measurements resulted in a median value of $3\,\text{m}\Omega\text{cm}^2$. We therefore derive an upper limit of $\rho_c < 5\,\text{m}\Omega\text{cm}^2$. Müller et al. [124] reported an absolute resistance per line of 0.46 Ωcm, which – using their contact width of $60\,\mu\text{m}$ – corresponds to a contact resistivity of $3\,\text{m}\Omega\text{cm}^2$ and is in good accordance with our results. Using the upper limit of $5\,\text{m}\Omega\text{cm}^2$ and a typical metallization fraction of $f = 10\%$ we estimate a small rear contact resistance of $R_c = \rho_c/f = 0.05\,\Omega\text{cm}^2$, which contributes to a total series resistance of $R_s = 0.7\,\Omega\text{cm}^2$. As demonstrated in the synergetic efficiency gain analysis (SEGA) in chapter 6, which applies the determined upper limit, the 21.2%-efficient PERC cells [6, 24] of this experiment only hold a potential of an absolute increase in efficiency of 0.06% when completely avoiding the contact resistivity of the rear Al contacts. Hence, it is presently not a dominant power loss mechanism.

We categorize local rear contacts into filled contact, partial voids and complete voids and notice, that complete voids exhibit shallower BSFs around $2\,\mu\text{m}$ compared to filled contacts with BSF depths of $4\,\mu\text{m}$. A similar analysis of 220 PERC cells fabricated at SolarWorld Innovations yields values of $1.8\,\mu\text{m}$ and $2.5\,\mu\text{m}$, respectively. We therefore identify void formation as an overlying effect occurring during BSF growth. We measure the BSF depth of PERC and PERC+ solar cells and find significantly deeper BSFs of up to $8\,\mu\text{m}$ for PERC+ compared to $4\,\mu\text{m}$ for PERC at a contact width of $80\,\mu\text{m}$. In order to model the different BSF depth we modify an existing analytical model for PERC cells [102] and take the limited Al mass of the screen printed Al fingers of PERC+ into account. We find good agreement between the models and their corresponding experimental data and thus show, that the different BSF depths are a consequence of the different amounts of Al taking part in the alloying process. We further extend the model of Ref. [102] to calculate contacts heights without any further fitting. The calculated contact heights underestimate the experimentally measured heights especially in case of PERC. EDX measurements reveal that this discrepancy is explained by Si that is experimentally dissolved, but not contributing to the Al-BSF formation as assumed by the model. In addition, the EDX measurements show silicon grains of several micrometers in diameter within the Al paste indicating a higher Si concentration in the Al paste during firing and therefore additional crystallization within the Al paste. From the measured heights, we observe that (complete) voids only emerge from contacts with a height above $20\,\mu\text{m}$, disclosing a geometry dependence of void formation. In accordance with the BSF analysis, we obtain highest PERC+ front side efficiencies of 21.1% at narrow contact lines of $48\,\mu\text{m}$ width, whereas the PERC cells achieve a maximum efficiency of 21.2% at a contact width of $81\,\mu\text{m}$.

For narrow contact lines of 49 µm width the efficiency strongly decreases due to increased rear contact recombination.

For the first time we show that the presence of voids inside local Al contacts is dependent on the contact geometry. Furthermore, from the impact of voids on the BSF depth, we conclude that void formation occurs during BSF growth in the liquid Al-Si phase. Both findings contradict the Kirkendall effect [114] and the connected void formation mechanism via lattice vacancy diffusion to be the physical root cause for voids. We introduce a new physical model that describes void formation as a consequence of surface energy minimization of the Al-Si melt. Using different geometrical approximations, we demonstrate that such a mechanism is in particular able to describe the experimentally observed critical height h_c. h_c is the height where neither a filled contact nor a void is energetically favored. According to the model, all contacts that are higher than the critical height should result in voids, whereas smaller contacts should remain filled with Al-Si melt until solidification. The physical reason is, that for large contact heights in case of filled contacts only a relatively small portion of the Al-Si melt wets the Si surface whereas in the void case a large portion of the Al-Si melt wets a large surface area of aluminum oxide shells making this case energetically favorable. The shallower contacts of PERC+ cells thus explain, why void formation is almost completely suppressed for this solar cell type. A comparison with test samples including fired contacts of PVD-Al and thus no aluminum oxide shells shows that these shells are indeed responsible for void formation as we do not find the characteristic large voids with several millimeters or centimeters in length for those samples.

6

Synergetic efficiency gain analysis of 21.2%-efficient industrial-type PERC solar cells

As the best industrial-type PERC cells achieve efficiencies of 22% and beyond, a quantification of the impact of all power loss mechanisms is required to ensure that future technological improvements reduce the dominating losses and hence provide a high efficiency improvement. The Free Energy Loss Analysis (FELA) [136] frequently used in solar cell analysis accounts for electrical power losses and represents those as free energy dissipation rates. Therefore the total extracted power P of a solar cell is the free energy generation rate ($\dot{F}_g$) minus the free energy dissipation rates caused by recombination ($\dot{F}_r$) and transport of charge carriers ($\dot{F}_t$):

$$P = \dot{F}_g - \dot{F}_r - \dot{F}_t. \tag{6.1}$$

For a given working point of a solar cell, one is now able to calculate for example the power loss $\dot{F}_r$ for a specific recombination channel. However, the potential in power gain by improving that recombination channel is higher than $\dot{F}_r$ since avoiding this loss will simultaneously increase the generated free energy

$$\dot{F}_g = \int_V dV (E_{FC} - E_{FV})g \tag{6.2}$$

where g is the generation rate in the cell volume V and $E_{FC} - E_{FV}$ denotes the splitting of the quasi-Fermi level of electrons and holes. The increase of free energy generation is noted by the experimentalist primarily as an increase of the solar cell's open circuit voltage V_{oc} and thus also by change of the working point V_{mpp}. Another approach to power loss analysis [137] uses analytic expressions to calculate the current losses by recombination and imperfect optics. In order to acquire the power losses these current losses are multiplied with the internal voltage of the solar cell at the maximum power point (mpp). This approach, as well as the FELA, does not account for the shift of the working point that goes along with avoiding a

loss. Correspondingly the calculated power losses underestimate the potential in power gain and will not add up to the theoretical limit of around 29%. To access the full potential power gains ΔP of each power loss mechanism, we apply the synergetic efficiency gain analysis (SEGA) [138] to our 21.2%-efficient industrial PERC solar cell [24]. The SEGA explains the efficiency gap between the cell under investigation and an ideal cell. It treats optical, electrical and resistive losses on an equal footing and makes these different losses directly comparable.

Numerical model

We model our 21.2%-efficient dual-printed 5 busbar (5BB) PERC solar cell (labeled "group 3" in Ref. [24]) which is schematically shown in Figure 6.1a) by a 3-step simulation sequence. Raytracing of a textured solar cell with SUNRAYS [139] generates a 1-dimensional photogeneration profile. This profile is then used in a 2D Sentaurus device [140] simulation of a PERC solar cell with a non-textured planar front surface. The unit cell is sketched in Figure 6.1b). Finally, the I-V curve resulting from the Sentaurus simulation is used for a grid simulation with LTSpice IV [141] to include resistive losses of front fingers and busbars. All simulations apply realistic input parameters that are either measured on test structures or are taken from literature.
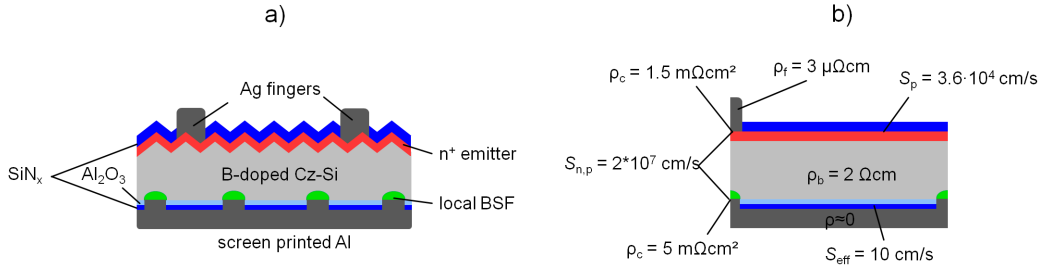

Figure 6.1: Schematic drawing of: a) the experimental 21.2% efficient PERC solar cell; b) the unit cell used in Sentaurus Device to simulate the PERC solar cell.

The raytracing simulation applies a SiN_x-coated random pyramid structure and a rear side with a SiN_x layer and an additional Al-layer on it. SUNRAYS provides a Monte-Carlo approach to optical simulation and generates single rays which are traced through the defined geometry. The Sentaurus simulation requires the width of the local Al-contacts that we determine from SEM images. We simulate the rear side Al contact pitch to be half of the front side pitch in order to keep the simulation domain at a manageable size. Since the experimental ratio of front and rear side pitch is not an integer, we scale the width of the rear contacts to match the actual metalization fraction. All contacts are assumed to be planar. The SRV of the SiN_x-passivated front surface S_p is adjusted to $3.6 \cdot 10^4$ cm/s in a separate simulation of a J_{0e} test structure (compare Figure 4.13a) that uses the measured phosphorus doping profile to match the measured J_{0e} values of 100 fA/cm^2 of the emitter of our PERC

cells [5]. Similarly, the SRV S_n of the local rear contact is adjusted in a simulation with a secondary ion mass spectroscopy (SIMS)-measured local aluminium doping profile to match the recombination current of a contact with an effective SRV S_{eff} of about $300\,cm/s$ (see section 4.1). In this case we use $S_n = 2 \cdot 10^7\,cm/s$ [142]. For the recombination at the Al_2O_3/SiN_x rear side passivation we use the parameterization by Black et al. [143] and adjust the interface defect density to a value that results in a recombination current that corresponds a surface recombination velocity of $S_{eff} = 10\,cm/s$, which is a typical value for our Al_2O_3/SiN_x passivation after firing (see section 4.1). The bulk material for the solar cell is the one labeled as "Cz $2\,\Omega cm$" in Ref. [144]. Annealing under illumination deactivates the BO_x-defects and results in effective lifetimes of around $1\,ms$ at an injection level of $\Delta n = 10^{15}\,cm^3$. The photoconductance measurement of the effective lifetime is fitted using 2 Shockley-Read-Hall (SRH) defects at mid-bandgap and the resulting τ_n and τ_p values of both defects are used in the Sentaurus simulation. The contact resistivity of the front Ag finger to the silicon is set to $1.5\,m\Omega cm^2$ as measured by TLM, whereas the contact resistivity of the aluminum-silicon interface is $5\,m\Omega cm^2$ (see section 5.1). A histogram for the distribution of the Ag finger cross sections is obtained by optical profilometer measurements. Using a specific resistivity of $3\,\mu\Omega cm$, based on the finger cross section distribution we calculate the distribution of the local finger line resistances and apply these values to the SPICE simulation in order to account for resistive losses due to non-ideal finger geometries. The resulting effective values of the finger line resistance correspond well to electrical measurements of the finger line resistance. Column 2 of Table 6.1 summarizes the input parameters applied for the simulation. The simulated PERC cell matches the experimental I-V parameters reasonably well as shown in Table 6.2.

Synergetic power gain analysis (SEGA)

We now perform different simulations, where each simulation applies one input parameter set to an ideal or close to ideal value. The differences in efficiency of the simulations to the initial (realistic) simulation quantifies the maximum efficiency gain obtainable from the deactivation of the respective single loss channel. All efficiency gains $\Delta\eta$ in this section are given in %abs, however, to improve readability we use % as an abbreviation. Column 3 of Table 6.1 lists the ideal values of the simulation parameters. The improvements in efficiency $\Delta\eta$ for each loss mechanism as resulting from our SEGA are shown in Figure 6.2. It shows that there is no single large dominating loss in our PERC cell. Only two loss mechanisms have a potential for an efficiency increase by more than 0.5%: This is front grid shadowing (0.82%) and recombination in the emitter and its surface (0.72%). Without surprise the first result agrees well to the quick linear approximation, that avoidance of the 4% front grid shadowing increases the short circuit current J_{sc} by 4% and therefore the efficiency by $4\% \cdot 21.2\% = 0.82\%$. The total saturation current density J_0 of our PERC solar cell is around $(250\pm30)\,fA/cm^2$ as determined by

Table 6.1: Input parameters of the numerical simulations of the 21.2%-efficient PERC solar cell in comparison to the theoretically ideal parameters. (* = measured; # = adjusted to match measured data)

	Realistic input parameters of 21.2% PERC cell	Ideal input parameters
Finger & busbar line resistance	$\rho_{\text{finger}} = 3\,\mu\Omega\text{cm}^*$, $\rho_{\text{busbar}} = 3\,\mu\Omega\text{cm}^*$	ρ_{finger} and $\rho_{\text{busbar}} \approx 0$
Front contact resistance	$\rho_{\text{c}} = 1.5\,\text{m}\Omega\text{cm}^{2*}$	$\rho_{\text{c}} \approx 0$
Bulk & emitter sheet resistance	$\rho_{\text{b}} = 2\,\Omega\text{cm}$ [144], $\rho_{\text{sh}} \approx 70\,\Omega/\text{sq.}$ [24]	$\rho_{\text{b}} \approx 0$, $\rho_{\text{sh}} \approx 0$
Rear contact resistance	$\rho_{\text{c}} = 5\,\text{m}\Omega\text{cm}^2$ (see section 5.1)	$\rho_{\text{c}} \approx 0$
SiN$_{\text{x}}$ front surface reflection	raytraced random pyramid SiN$_{\text{x}}$	transmission $T = 1$
Rear surface reflection	raytraced SiN$_{\text{x}}$/Al layers	$R_{\text{b}} = 1$, $\Lambda = 1$
Front grid shadowing	shadowing = 4% [24]	shadowing = 0%
Ag contacts	$S_{\text{p}} = 2 \cdot 10^7\,\text{cm/s}$ [142]	$S_{\text{p}} = 1\,\text{cm/s}$
Phosphorus emitter & SiN$_{\text{x}}$ passivation	measured ECV dopant profile, $S_{\text{p}} = 36000\,\text{cm/s}^{\#}$	$\tau_{\text{SRH}} = 1\,\text{s}$, no Auger, $S_{\text{p}} = 1\,\text{cm/s}$
Silicon bulk	SRH model	$\tau_{\text{SRH}} = 1\,\text{s}$
Rear Al-contact & Al-BSF	metal surface: $S_{\text{n}} = 2 \cdot 10^7\,\text{cm/s}$ [142], Al-BSF measured by SIMS	metal surface: $S_{\text{n}} = 1\,\text{cm/s}$, BSF: $\tau_{\text{SRH}} = 1\,\text{s}$, no Auger
Al$_2$O$_3$/SiN$_{\text{x}}$ rear passivation	$S_{\text{eff}} = 10\,\text{cm/s}$ (see section 4.1)	$S_{\text{eff}} \approx 0$

Table 6.2: I-V parameters of the experimental 5BB PERC solar cell and the simulated PERC cell. (* = independently confirmed by Fraunhofer ISE Callab)

	$\eta[\%]$	$V_{\text{oc}}[\text{mV}]$	$J_{\text{sc}}[\text{mA/cm}^2]$	$FF[\%]$
Experimental 5BB PERC solar cell [24]	21.22*	662.1	39.8	80.6
Numerical simulation of 5BB PERC cell	21.27	661.5	39.7	80.9

a fit to the IV curve. Thus the emitter with its J_{0e} of $100 \, \text{fA/cm}^2$ has also been expected to dominate recombination losses and to imply a large potential for power gains. The next three large contributors are 0.47% from the SiN_x ARC surface reflection, 0.46% from the bulk and emitter resistivity and 0.43% from recombination at the local rear Al-contacts. The first one is also plausible since the SiN_x-coated random pyramid surface reflects about 2.4% of the incident photons of a AM1.5G spectrum. Applying the same rule of thumb as for the shadowing above yields $2.4\% \cdot 21.2\% = 0.50\%$. The internal bulk & emitter resistance is the largest contributor to the 0.8% power gain due to resistive losses. The contribution of the front Ag-finger grid is considerably smaller because of the 5BB design of the cell. In order to obtain the gain for the bulk & emitter resistance we carry out a simulation of a triple-light-level measurement [126] of a solar cell without front and rear contact resistances and the Ag-finger grid resistance. This results in a measured voltage-dependent lumped series resistance for the bulk and emitter $R_{s,b+em}(V)$. Based on this result and the IV-curve of the basic 21.2%-efficient, we can calculate the enhanced voltages V_{enh} for an IV-curve of a solar cell without the bulk & emitter resistance: $V_{enh} = V + R_{s,b+em}(V) \cdot I$. To gain confidence in this result we can support our simulation with some quick analytic calculations. The resistance of the finger grid is $R_{grid} = 0.17 \, \Omega\text{cm}^2$ as noted from our SPICE simulation. Using analytic expressions for the resistance of the emitter R_{em} [46], the resistance of the bulk R_b [77] and calculating the contact resistances according to $R_c = \rho_c/f$ with f as the corresponding metallization fractions (4% front side, 10% rear side) we find $R_{grid} = 0.17 \, \Omega\text{cm}^2$, $R_{em} = 0.15 \, \Omega\text{cm}^2$, $R_{bulk} = 0.17 \, \Omega\text{cm}^2$, $R_{c,front} = 0.04 \, \Omega\text{cm}^2$, $R_{c,rear} = 0.05 \, \Omega\text{cm}^2$. These resistances add up to $0.58 \, \Omega\text{cm}^2$, which is close to the total series resistance of $0.62 \, \Omega\text{cm}^2$ of the 21.2% PERC cell that we measure with the fill factor method. Calculating the relative contribution to the resistance and multiplying with the total resistive power loss reproduces the results of the simulation with reasonable accuracy, for example $\Delta\eta = (0.17 + 0.15)/0.62 \cdot 0.8\% = 0.41\%$ for the bulk & emitter contribution. Finally, the recombination at the local Al-contacts with an effective SRV of $300 \, \text{cm/s}$ is, as expected, the second largest contributor to recombination.

Apart from the single efficiency gains due to deactivation of specific power loss mechanisms Figure 6.2 shows two columns for each power loss category (resistance, optics, recombination). The column labeled as "sum" sums up all the individual power gains of the simulations of its category. The columns labeled as "all" in the respective category represent additional simulations that apply simultaneous deactivation of all the power losses of the corresponding category. Comparison of the "sum" with the "all"-simulation allows the assessment of the impact of nonlinearities or synergies in each category. Simultaneously avoiding all resistive losses leads to an efficiency enhancement of 0.8%, which is equal to the sum. This indicates that all individual resistances add to a total lumped resistance. The sum of all optical gains is 1.6% and thus twice as large as all the resistive gains. A simulation that avoids all the optical losses yields an efficiency gain of 1.7%.
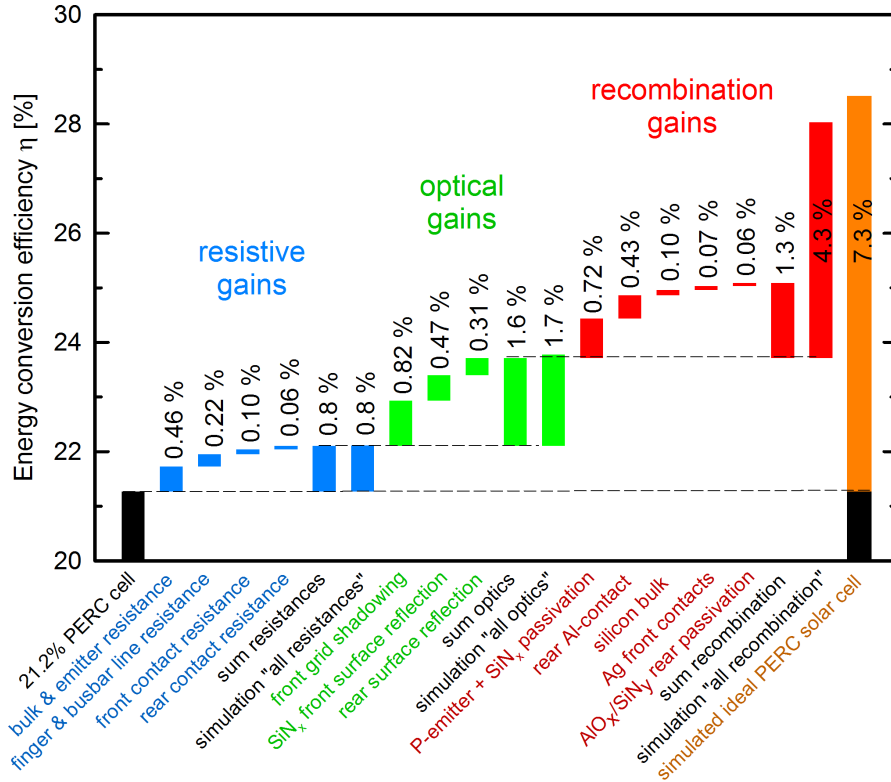
Figure 6.2: Absolute gains in efficiency $\Delta\eta$ after deactivating single power loss mechanisms. The entries labeled as "sum" sum up the $\Delta\eta$ values for a category (i.e. resistance, optics, recombination), whereas the entries labeled as "all" represent simulations with the corresponding parameters set to their ideal values. The "ideal PERC solar cell" models the case that all input parameters assume ideal values.

There is thus 0.1% synergetic efficiency enhancement due to effects such as the open circuit voltage enhancement due to enhanced photogeneration. Summing up the various individual recombination gains enhances the efficiency by 1.3%. The separate simulation, that simultaneously applies all ideal values of Table 6.1 (and thus only contains unavoidable intrinsic bulk recombination), yields 4.3% efficiency increase. The synergetic efficiency enhancement of the recombination losses is thus 3% which makes recombination the most important loss mechanism when compared to optical and resistive efficiency losses. Finally, when all input parameters are set to their ideal values, the resulting simulated efficiency is 28.5% and thus 7.3% higher than the efficiency of the experimental 21.2% efficient PERC cell. The sum of all individual losses account for 3.7% = 0.8% + 1.6% + 1.3% only. This shows that the synergetic efficiency increase originating from the coupling of the various recombination loss mechanisms is 3.6% and is thus as large as the sum of all individual gains. The efficiency of our simulated ideal solar cell is still slightly lower

than the theoretical limit of 28.8% [145] for a 180 µm thick bulk when considering radiative and Auger recombination as the only loss mechanisms (without photon recycling). This might be due to remaining extrinsic recombination that we allowed in our "ideal" solar cell.

Conclusion

For the first time, we apply the simulation-based synergetic efficiency gain analysis (SEGA) to industrial-type PERC solar cells. The SEGA allows assessment of the full potential power gain by improving single power loss mechanisms. Furthermore, it is able to treat resistive, optical and recombinative power losses in an equal manner in terms of their power loss impact. Application of the SEGA to our 21.2%-efficient PERC solar cell shows that synergies of the recombination losses are particularly strong and amount to 3%. They contribute largely to the efficiency gap of 7.3% that our cell has with reference to an ideal cell. The SEGA shows that the power loss due to recombination in the phosphorus-doped emitter and its SiN_x-passivated surface currently limits the solar cell efficiency with a potential power gain of 0.7%. Another power loss mechanism that allows for large efficiency increases is the shadowing of the finger and busbars with a potential gain of 0.8%, although the cell has a shadowing of only 4% due to its advanced 5BB-design.

Summary

For the first time, we have investigated the impact of the rear surface roughness on the electrical and optical properties of PERC solar cells with screen printed rear metalization applying an Al_2O_3/SiN_x or a SiO_2/SiN_x passivation layer stack. Using lifetime test wafers we have measured generally smaller SRVs for higher polishing removals of a previously textured surface. In case of Al_2O_3/SiN_x we have found SRVs below $S_{pass} = 20\,cm/s$ even for small polishing removals of $5\,\mu m$. In contrast, the SiO_2/SiN_x passivation layer stack requires polishing removals of $10\,\mu m$ or more to exhibit similar values. In accordance with the test wafer results Al_2O_3/SiN_x-passivated solar cells show a smaller dependence of the IQE in the infrared regime on the rear surface roughness when compared to SiO_2/SiN_x. For Al_2O_3/SiN_x we have consequently found small effective SRVs at the rear below $S_{rear} = 100\,cm/s$ even for small polishing removals. Also from the IQE and reflectance measurements, we have determined an increase of internal rear reflectance by 2%abs, which leads to an increase in J_{sc} of $0.2\,mA/cm^2$ at the most. The measured efficiency improvement of 1%abs when comparing textured with planar rear surfaces is therefore primarily caused by recombination and only secondarily by an improved light trapping. Based on these findings, we have presented for the first time, a lean industrial-type PERC process flow applying double-sided texturing, double sided $POCl_3$ diffusion and subsequent single-sided polishing to remove the rear emitter and reduce surface roughness. The polished PERC solar cells, which apply a polishing removal of $5\,\mu m$, achieve efficiencies of up to 20.7% comparable to the reference PERC process applying a rear protection layer instead of a polishing step. Using the same reference PERC process, we have investigated industrially feasible cleaning sequences prior to $ALD-Al_2O_3/SiN_x$ passivation. Using an industrial batch-type cleaning tool a two-step sequence of pSC1, HF/HCl results in PERC cell efficiencies up to 20.4%, which is comparable to PERC cells cleaned with a high quality laboratory-type RCA. An even shorter one-step process of HF/O_3 allows for an excellent rear surface passivation with SRVs $S_{pass} < 15\,cm/s$ and effective rear SRVs $S_{rear} < 50\,cm/s$ as measured on lifetime test samples and PERC solar cells, respectively, where both

values are comparable to the RCA clean. However, in case of strongly n^+-doped surfaces such as the PERC front side, we have found that the HF/O$_3$ process leads to a roughening of the surface on a nanometer scale. The rough surface causes an enhanced front surface recombination for PERC solar cells and thus leads to a strong decrease in efficiency.

We have determined an upper limit of $\rho_c < 5\,\text{m}\Omega\text{cm}^2$ for the effective contact resistivity of the screen printed local Al contacts to the Si bulk at the rear of the PERC solar cells using TLM measurements as well as a rear contact pitch variation of PERC cells. We have compared local Al contacts of bifacial PERC+ and PERC solar cells and found significantly deeper BSFs in case of PERC+. At a contact width of 60 μm we found BSF depths of around 8 μm and 4 μm for PERC+ and PERC, respectively. We have extended an existing analytical model for calculation of BSF depths in order to account for the limited Al-finger mass in case of PERC+. The resulting model showed excellent agreement with the measured data indicating that the deeper BSFs of PERC+ are indeed caused by the different amount of Al printed to the rear side of the solar cells. A further extension of the analytical model allowed for calculation of the contact heights, which again agreed well to measured values. We have found evidence for a higher Si concentration of the Al fingers compared to a full area Al layer, as the fingers incorporate grains of almost pure silicon that are not observed for the closed layer. In accordance with the BSF depth analysis we found high PERC+ efficiencies of up to 21.1% even for narrow contacts of 48 μm in width, whereas PERC cells using a comparable contact width only achieved 19.5% efficiency. We have categorized the rear contacts into three different types, i.e. filled contact, partial void and complete void, and found that complete voids are typically accompanied by shallower BSFs compared to filled contacts. We have therefore concluded that void formation occurs during BSF growth and thus in the liquid Al-Si phase. Furthermore, for the first time, we have demonstrated a dependence of the void ratio on the contact geometry, i.e. the contact height. As both observations concerning void formation contradict the commonly used explanation including the Kirkendall effect, we have introduced a new physical model that describes void formation as a consequence of surface energy minimization of the Al-Si melt during firing. The model attributes the root cause of void formation to the aluminum oxide shells incorporated in screen printed Al and is in particular able to describe the experimental finding that voids only originate from contacts that exceed a certain height. The model is supported by measurements on test samples with fired PVD-Al contacts and, hence, no aluminum oxide shells as these samples do not show the typical voids with several centimeters in length.

For the first time, we have applied the synergetic efficiency gain analysis to an industrial-type PERC solar cell. By doing so, we have identified the dominant power loss mechanisms of our PERC cell with 21.2% efficiency, which was a record efficiency at the time of publication. The analysis shows that avoiding recombination offers the largest potential of 4.3%abs for a future efficiency improvement. This is

caused by the strong nonlinear coupling of the different recombination channels, whereas resistive and optical losses (almost) sum up linearly. The single most important power loss mechanisms are the recombination in the phosphorus-doped emitter and its SiN_x-passivated surface and front grid shadowing, which offer an efficiency gain of 0.7%abs and 0.8%abs, respectively.

References

[1] P. J. Verlinden, Y. Zhang, T. Kondo, and Z. Feng. Advanced silicon solar cell strategy for lower cost of electricity. Presented at the nPV Workshop 2014.

[2] International Technology Roadmap for Photovoltaic. (ITRPV): Results 2015, Seventh Edition: March 2016.

[3] A. Metz, D. Adler, S. Bagus, H. Blanke, M. Bothar, E. Brouwer, S. Dauwe, K. Dressler, R. Droessler, T. Droste, M. Fiedler, Y. Gassenbauer, T. Grahl, N. Hermert, W. Kuzminski, A. Lachowicz, T. Lauinger, N. Lenck, M. Manole, M. Martini, R. Messmer, C. Meyer, J. Moschner, K. Ramspeck, P. Roth, R. Schönfelder, B. Schum, J. Sticksel, K. Vaas, M. Volk, and K. Wangemann. Industrial high performance crystalline silicon solar cells and modules based on rear surface passivation technology. *Solar Energy Materials and Solar Cells*, 120, Part A:417 – 425, 2014.

[4] International Technology Roadmap for Photovoltaic. (ITRPV): Results 2012, (semi PVGroup, 2013), Fig. 34.

[5] H. Hannebauer, M. Sommerfeld, J. Müller, T. Dullweber, and R. Brendel. Analysis of the emitter saturation current density of industrial type silver screen-printed front contacts. In *Proceedings of the 27th European Photovoltaic Solar Energy Conference, Frankfurt, Germany*, pages 1360–1363, 2012.

[6] T. Dullweber, H. Hannebauer, U. Baumann, T. Falcon, K. Bothe, S. Steckemetz, and R. Brendel. Fine-line printed 5 busbar PERC solar cells with conversion efficiencies beyond 21%. In *In Proceedings of the 29th European Photovoltaic Solar Energy Conference, Amsterdam, Netherlands*, pages 621–626, 2014.

[7] Trina solar, press release, December 2015. Available at: `http://ir.trinasolar.com/phoenix.zhtml?c=206405&p=irol-newsArticle&ID=2122938` [accessed on 03 Jun 2016].

[8] F. Ye, W. Deng, W. Guo, R. Liu, D. Chen, Y. Chen, Y. Yang, N. Yuan, J. Ding, Z. Feng, P. P. Altermatt, and P. J. Verlinden. 22.13% efficient industrial p-type mono PERC solar cell. In *Proceedings of the 43rd IEEE Photovoltaic Specialists Conference*, 2016. In press.

References

[9] International Technology Roadmap for Photovoltaic. (ITRPV): Results 2014, Sixth Edition: July 2015.

[10] A. Rohatgi and D. Meier. Developing novel low-cost, high-throughput processing techniques for 20%-efficient monocrystalline silicon solar cells. *Photovoltaics International*, 10:87–93, 2010.

[11] M. Tucci, E. Talgorn, L. Serenelli, E. Salza, M. Izzi, and P. Mangiapane. Laser fired back contact for silicon solar cells. *Thin Solid Films*, 516(20):6767 – 6770, 2008. Proceedings on Advanced Materials and Concepts for Photovoltaics {EMRS} 2007 Conference, Strasbourg, France.

[12] A. W. Blakers, A. Wang, A. M. Milne, J. Zhao, and M. A. Green. 22.8% efficient silicon solar cell. *Applied Physics Letters*, 55(13):1363–1365, 1989.

[13] J. Zhao, A. Wang, and M. A. Green. 24 · 5% efficiency silicon pert cells on mcz substrates and 24 · 7% efficiency perl cells on fz substrates. *Progress in Photovoltaics: Research and Applications*, 7(6):471–474, 1999.

[14] M. A. Green. The path to 25% silicon solar cell efficiency: History of silicon cell evolution. *Progress in Photovoltaics: Research and Applications*, 17(3):183–189, 2009.

[15] Panasonic, press release, April 2014. Available at: `http://news.panasonic.com/global/press/data/2014/04/en140410-4/en140410-4.html` [accessed on 03 Jun 2016].

[16] M. A. Green. Crystalline silicon solar cells. Photovoltaics Special Research Centre (2001).

[17] G. Agostinelli, P. Choulat, H. F. W. Dekkers, E. Vermarien, and G. Beaucarne. Rear surface passivation for industrial solar cells on thin substrates. In *IEEE 4th World Conference on Photovoltaic Energy Conference*, pages 1004–1007, 2006.

[18] K. A. Münzer, J. Schöne, A. Teppe, R. E. Schlosser, M. Hein, D. Hammer, S. Hüls, M. Hanke, S. Keller, and P. Fath. Advanced rear side technology for industrial high efficiency solar cells. In *Proceedings of the 25th European Photovoltaic Solar Energy Conference and Exhibition, Valencia, Spain*, pages 2314–2318, 2010.

[19] S. Gatz, H. Hannebauer, R. Hesse, F. Werner, A. Schmidt, T. Dullweber, J. Schmidt, K. Bothe, and R. Brendel. 19.4%-efficient large-area fully screen-printed silicon solar cells. *physica status solidi (RRL)-Rapid Research Letters*, 5(4):147–149, 2011.

[20] Bosch Solar Energy AG, press release, April 2011. Available at: `http://www.pv-tech.org/news/bosch_solar_energys_perc_cell_achieves_record_breaking_efficiency` [accessed on 03 Jun 2016].

[21] Schott Solar AG, press release, August 2011. Available at: `http://www.schmid-group.com/en/press-%2B-news/press-releases/a67/efficiency-record-of-over-20--for-mono-crystalline-solar-cells.html` [accessed on 03 Jun 2016].

[22] P. Engelhart, D. Manger, B. Klöter, S. Hermann, A. A. Stekolnikov, S. Peters, H. C. Ploigt, A. Eifler, C. Klenke, A. Mohr, et al. Q. ANTUM–Q-Cells next generation high-power silicon cell & module concept. In *Proceedings of the 26th Photovoltaic Solar Energy Conference, Hamburg, Germany*, pages 821–826, 2011.

[23] A Lachowicz, K Ramspeck, P Roth, M Manole, H Blanke, W Hefner, E Brouwer, B Schum, and A Metz. NO_x-free solution for emitter etch-back. In *Proceedings of the 27th European Photovoltaic Solar Energy Conference and Exhibition, Frankfurt*, pages 1846–1850, 2012.

[24] H. Hannebauer, T. Dullweber, U. Baumann, T. Falcon, and R. Brendel. 21.2%-efficient fineline-printed PERC solar cell with 5 busbar front grid. *Physica Status Solidi – Rapid Research Letters*, 8(8):675–679, 2014.

[25] P. J. Verlinden, W. Deng, Y. Zhang, X. Yang, Z. Xiong, J. Xu, P. Shu, Y. Quan, J. Sheng, Y. Chen, S. Zhang, J. Bao, F. Ping, Y. Zhang, and Z. Feng. Strategy, development and mass-production of high-efficiency crystalline silicon pv modules. In *Proceedings of the 6th World Conference on Photovoltaic Energy Conversion*, pages 485–488, 2014.

[26] SolarWorld AG, press release, Juli 2015. Available at: `http://www.solarworld.de/en/group/investor-relations/news-announcements/corporate-news/single-ansicht/article/solarworld-ag-sets-new-world-record-for-solar-cell-efficiency/` [accessed on 03 Jun 2016].

[27] T. Dullweber and J. Schmidt. Industrial silicon solar cells applying the passivated emitter and rear cell (PERC) concept – A review. *IEEE Journal of Photovoltaics*, 6(5):1366–1381, 2016.

[28] SolarWorld AG, press release, January 2016. Available at: `http://www.pv-tech.org/news/solarworld-reaches-22-efficiency-in-p-type-perc-cell` [accessed on 06 Jun 2016].

[29] E. Schneiderlöchner, R. Preu, R. Lüdemann, and S. W. Glunz. Laser-fired rear contacts for crystalline silicon solar cells. *Progress in Photovoltaics: Research and Applications*, 10(1):29–34, 2002.

References

[30] T. Böscke, R. Hellriegel, T. Wütherich, L. Bornschein, A. Helbig, R. Carl, M. Dupke, D. Stichtenoth, T. Aichele, R. Jesswein, T. Roth, C. Schöllhorn, T. Geppert, A. Grohe, J. Lossen, and H. J. Krokoszinski. Fully screen-printed PERC cells with laser-fired contacts – An industrial cell concept with 19.5% efficiency. In *Proceedings of the 37th IEEE Photovoltaic Specialists Conference*, pages 003663–003666, June 2011.

[31] J. Nekarda, A. Grohe, O. Schultz, and R. Preu. Aluminum foil as back side metallization for LFC cells. In *Proceedings of the 22nd European Photovoltaic Solar Energy Conference, Milan, Italy*, pages 1499–1501, 2007.

[32] M. J. Kerr and A. Cuevas. Very low bulk and surface recombination in oxidized silicon wafers. *Semiconductor Science and Technology*, 17(1):35, 2002.

[33] J. Schmidt, A. Merkle, R. Bock, P. P. Altermatt, A. Cuevas, N.-P. Harder, B. Hoex, R. Van de Sanden, E. Kessels, and R. Brendel. Progress in the surface passivation of silicon solar cells. In *Proceedings of the 23rd European Photovoltaic Solar Energy Conference, Valencia, Spain*, 2008.

[34] M. Stocks, A. Cuevas, and A. Blakers. Minority carrier lifetimes of multicrystalline silicon during solar cell processing. In *Proceedings of the 14th European Photovoltaic Solar Energy Conference, Barcelona, Spain*, pages 770–773, 1997.

[35] B. Hoex, J. Schmidt, P. Pohl, M. C. M. van de Sanden, and W. M. M. Kessels. Silicon surface passivation by atomic layer deposited al2o3. *Journal of Applied Physics*, 104(4), 2008.

[36] R. Hezel and K. Jaeger. Low-temperature surface passivation of silicon for solar cells. *Journal of the Electrochemical Society*, 136(2):518–523, 1989.

[37] G. Agostinelli, A. Delabie, P. Vitanov, Z. Alexieva, H. F. W. Dekkers, S. De Wolf, and G. Beaucarne. Very low surface recombination velocities on p-type silicon wafers passivated with a dielectric with fixed negative charge. *Solar Energy Materials and Solar Cells*, 90(18):3438–3443, 2006.

[38] S. Dauwe, L. Mittelstädt, A. Metz, and R. Hezel. Experimental evidence of parasitic shunting in silicon nitride rear surface passivated solar cells. *Progress in Photovoltaics: Research and Applications*, 10(4):271–278, 2002.

[39] P. Saint-Cast, D. Kania, M. Hofmann, J. Benick, J. Rentsch, and R. Preu. Very low surface recombination velocity on p-type c-si by high-rate plasma-deposited aluminum oxide. *Applied Physics Letters*, 95(15), 2009.

[40] T. Dullweber, C. Kranz, B. Beier, B. Veith, J. Schmidt, B. F. P. Roos, O. Hohn, T. Dippell, and R. Brendel. Inductively coupled plasma chemical

vapour deposited alox/siny layer stacks for applications in high-efficiency industrial-type silicon solar cells. *Solar Energy Materials and Solar Cells*, 112:196 – 201, 2013.

[41] F. Werner, W. Stals, R. Görtzen, B. Veith, R. Brendel, and J. Schmidt. High-rate atomic layer deposition of al2o3 for the surface passivation of si solar cells. *Energy Procedia*, 8:301 – 306, 2011.

[42] M. Schubert and W. Warta. Prediction of diffusion length in multicrystalline silicon solar cells from trapping images on starting material. *Progress in photovoltaics: research and applications*, 15:331–336, 2006.

[43] S. Braun, G. Micard, and G. Hahn. Solar cell improvement by using a multi busbar design as front electrode. *Energy Procedia*, 27:227 – 233, 2012.

[44] S. Braun, G. Hahn, R. Nissler, C. Pönisch, and D. Habermann. Multi-busbar solar cells and modules: High efficiencies and low silver consumption. *Energy Procedia*, 38:334 – 339, 2013.

[45] J. Walter, M. Tranitz, M. Volk, C. Ebert, and U. Eitner. Multi-wire inter-connection of busbar-free solar cells. *Energy Procedia*, 55:380 – 388, 2014.

[46] A. Mette. PhD thesis, Albert-Ludwigs-Universität Freiburg im Breisgau, Fakultät für Angewandte Wissenschaften, 2007. p.17.

[47] SolarWorld AG, press release, May 2015. Available at: `http://www.pv-magazine.com/news/details/beitrag/solarworld-to-introduce-five-busbars-to-us-production_100019319/#axzz4B0MN1Vdb` [accessed on 08 Jun 2016].

[48] T. Röder, P. Grabitz, S. Eisele, C. Wagner, J. R. Köhler, and J. H. Werner. 0.4% absolute efficiency gain of industrial solar cells by laser doped selective emitter. In *Proceedings of the 34th IEEE Photovoltaic Specialists Conference*, pages 871–873, 2009.

[49] T. C. Röder, S. J. Eisele, P. Grabitz, C. Wagner, G. Kulushich, J. R. Köhler, and J. H. Werner. Add-on laser tailored selective emitter solar cells. *Progress in Photovoltaics: Research and Applications*, 18(7):505–510, 2010.

[50] T. Pletzer, E. Stegemann, L. Janßen, H. Windgassen, D. L. Bätzner, and H. Kurz. Selective emitters by phosphorus screen-printing for industrial processing of very thin MC-Si solar cells. In *Proceedings of the 22nd European Photovoltaic Solar Energy Conference, Milan, Italy*, pages 1604–1607, 2007.

[51] F. Book, T. Wiedenmann, A. Dastgheib-Shirazi, B. Raabe, and G. Hahn. Large area n-type silicon solar cells with selective front surface field and screen printed aluminium-alloyed rear emitter. In *Proceedings of the 25th European*

Photovoltaic Solar Energy Conference, Valencia, Spain, pages 1465–1468, 2010.

[52] H. Hannebauer, T. Dullweber, S. Wyczanowski, K. Weise, F. Delahaye, O. Doll, I. Köhler, and R. Brendel. Gas phase etch back: A new selective emitter technology for high-efficiency PERC solar cells. In *Proceedings of the 28th European Photovoltaic Solar Energy Conference and Exhibition, Paris, France*, pages 752–756, 2013.

[53] pv-tools. Hamelin, Germany. Available at: `http://www.pv-tools.de/products/loana-system/loana-start.html` [accessed on 13 Jun 2016].

[54] P. Würfel. *Physics of solar cells: from principles to new concepts.* John Wiley & Sons, 2005.

[55] M. A. Green. "Efficiency limits, losses, and measurement" in: "Solar cells: Operating principles, technology, and system applications". *Englewood Cliffs, NJ, USA: Prentice-Hall*, 1992.

[56] R. A. Sinton and A. Cuevas. Contactless determination of current-voltage characteristics and minority carrier lifetimes in semiconductors from quasi-steady-state photoconductance data. *Appl. Phys. Lett.*, 69:2510–2512, 1996.

[57] J. M. Dorkel and P. Leturcq. Carrier mobilities in silicon semi-emirically related to temperature, doping and injection-level. *Solid-State Electron.*, 24:821–825, 1981.

[58] K. Ramspeck, S. Reissenweber, J. Schmidt, K. Bothe, and R. Brendel. Dynamic carrier lifetime imaging of silicon wafers using an infrared-camera-based approach. *Applied Physics Letters*, 93(10), 2008.

[59] K. Ramspeck, K. Bothe, J. Schmidt, and R. Brendel. Combined dynamic and steady-state infrared camera based carrier lifetime imaging of silicon wafers. *Journal of Applied Physics*, 106(11), 2009.

[60] S. Herlufsen, J. Schmidt, D. Hinken, K. Bothe, and R. Brendel. Photoconductance-calibrated photoluminescence lifetime imaging of crystalline silicon. *Physica Status Solidi – Rapid Research Letters*, 2:245–247, 2008.

[61] S. Herlufsen, J. Schmidt, D. Hinken, K. Bothe, and R. Brendel. Camera-based photoluminescence lifetime imaging of crystalline silicon wafers. In *Proceedings of the 24th European Photovoltaic Solar Energy Conference, Hamburg, Germany*, volume 1, 2009.

[62] K. L. Luke and L. Cheng. Analysis of the interaction of a laser pulse with a silicon wafer: Determination of bulk lifetime and surface recombination velocity. *Journal of Applied Physics*, 61(6):2282–2293, 1987.

[63] B. Fischer. *Loss analysis of crystalline silicon solar cells using photoconductance and quantum efficiency measurements.* PhD thesis, University of Konstanz, 2003.

[64] R. Brendel, M. Hirsch, R. Plieninger, and J. J. H. Werner. Quantum efficiency analysis of thin-layer silicon solar cells with back surface fields and optical confinement. *IEEE Transactions on Electron Devices*, 43(7):1104–1113, 1996.

[65] H. H. Berger. Contact resistance and contact resistivity. *Journal of the Electrochemical Society*, 119(4):507–514, 1972.

[66] D. K. Schroder. *Semiconductor material and device characterization.* John Wiley & Sons, 2006.

[67] S. Eidelloth, F. Haase, and R. Brendel. Simulation tool for equivalent circuit modeling of photovoltaic devices. *IEEE Journal of Photovoltaics*, 2 (4):572–579, 2012.

[68] T. Dullweber, S. Gatz, H. Hannebauer, T. Falcon, R. Hesse, J. Schmidt, and R. Brendel. Towards 20% efficient large-area screen-printed rear-passivated silicon solar cells. *Progress in Photovoltaics: Research and Applications*, 20(6):630–638, 2012.

[69] H. Hannebauer, T. Dullweber, T. Falcon, and R. Brendel. Fineline printing options for high efficiencies and low ag paste consumption. *Energy Procedia*, 38:725 – 731, 2013.

[70] H. Hannebauer, S. Schimanke, T. Falcon, P. P. Altermatt, and T. Dullweber. Optimized stencil print for low ag paste consumption and high conversion efficiencies. *Energy Procedia*, 67:108 – 115, 2015.

[71] H. Fischer. *A history of the central limit theorem: From classical to modern probability theory.* Springer Science & Business Media, 2010. Chapter 2.

[72] R. C. Sprinthall. *Basic Statistical Analysis.* 2011.

[73] Student. The probable error of a mean. *Biometrika*, 6(1):1–25, 1908.

[74] B. L. Welch. The generalization of 'Student's' problem when several different population variances are involved. *Biometrika*, 34(1-2):28–35, 1947.

[75] T. Dullweber, C. Kranz, R. Peibst, U. Baumann, H. Hannebauer, A. Fülle, S. Steckemetz, T. Weber, M. Kutzer, M. Müller, G. Fischer, P. Palinginis, and H. Neuhaus. PERC+: industrial PERC solar cells with rear Al grid enabling bifaciality and reduced Al paste consumption. *Progress in Photovoltaics: Research and Applications*, 24:1487–1498, 2015.

References

[76] T. Dullweber, C. Kranz, R. Peibst, U. Baumann, H. Hannebauer, A. Fülle, S. Steckemetz, T. Weber, M. Kutzer, M. Müller, G. Fischer, P. Palinginis, and H. Neuhaus. The PERC+ cell: More output power for less aluminum paste. *Photovoltaics International*, 30:53–63, 2016.

[77] P. Saint-Cast. PhD thesis, University of Konstanz, 2012.

[78] T. Dullweber, C. Kranz, R. Peibst, U. Baumann, H. Hannebauer, A. Fülle, S. Steckemetz, T. Weber, M. Kutzer, M. Müller, G. Fischer, P. Palinginis, and H. Neuhaus. The PERC+ cell: A 21%-efficient industrial bifacial PERC solar cell. In *Proceedings of the 31th European Photovoltaic Solar Energy Conference, Munich, Germany*, pages 341–350, 2016.

[79] S. Queisser, K. De Keersmaecker, T. Borgers, E. Wefringhaus, D. Nagel, B. U. Sander, M. Loehmann, M. Weber, and F. Delahaye. Inline single side polishing and junction isolation for rear side passivated solar cells. In *Proceedings of the 24th European Photovoltaic Solar Energy Conference, Hamburg, Germany*, pages 1792–1794, 2009.

[80] K. R. McIntosh and L. P. Johnson. Recombination at textured silicon surfaces passivated with silicon dioxide. *Journal of Applied Physics*, 105(12), 2009.

[81] T. Lauinger, J. Schmidt, A. G. Aberle, and R. Hezel. Record low surface recombination velocities on 1 Ωcm p-silicon using remote plasma silicon nitride passivation. *Applied Physics Letters*, 68(9):1232–1234, 1996.

[82] A. Stesmans and V. V. Afanasa´ev. Thermally induced interface degradation in (100) and (111) Si/SiO$_2$ analyzed by electron spin resonance. *Journal of Vacuum Science & Technology B*, 16(6):3108–3111, 1998.

[83] S. C. Baker-Finch and K. R. McIntosh. The contribution of planes, vertices, and edges to recombination at pyramidally textured surfaces. *IEEE Journal of Photovoltaics*, 1(1):59–65, 2011.

[84] P. J. Cousins and J. E. Cotter. Minimizing lifetime degradation associated with thermal oxidation of upright randomly textured silicon surfaces. *Solar Energy Materials and Solar Cells*, 90(2):228 – 240, 2006.

[85] M. J. Kerr, J. Schmidt, A. Cuevas, and J. H. Bultman. Surface recombination velocity of phosphorus-diffused silicon solar cell emitters passivated with plasma enhanced chemical vapor deposited silicon nitride and thermal silicon oxide. *Journal of Applied Physics*, 89(7):3821–3826, 2001.

[86] H. Jin, K. J. Weber, and A. W. Blakers. Depassivation of Si-SiO$_2$ interface following rapid thermal annealing. In *Conference Record of the IEEE 4th World Conference on Photovoltaic Energy Conversion*, pages 1078–1080, 2006.

[87] H. Jin, K. J. Weber, and A. W. Blakers. The effect of a post oxidation in-situ nitrogen anneal on si surface passivation. In *Conference Record of the IEEE 4th World Conference on Photovoltaic Energy Conversion*, pages 1071–1073, 2006.

[88] F. W. Chen, T.-T. A. Li, and J. E. Cotter. PECVD silicon nitride surface passivation for high-efficiency *n*-type silicon solar cells. In *Conference Record of the IEEE 4th World Conference on Photovoltaic Energy Conversion*, pages 1020–1023, 2006.

[89] D. Kray, M. Hermle, and S. W. Glunz. Theory and experiments on the back side reflectance of silicon wafer solar cells. *Progress in Photovoltaics: Research and Applications*, 16(1):1–15, 2008.

[90] C. Schwab, A. Wolf, M. Graf, N. Wöhrle, S. Kühnhold, J. Greulich, G. Kästner, D. Biro, and R. Preu. Recombination and optical properties of wet chemically polished thermal oxide passivated Si surfaces. *IEEE Journal of Photovoltaics*, 3(2):613–620, 2013.

[91] A. Dastgheib-Shirazi, M. Steyer, J. Junge, S. Gindner, and G. Hahn. A study of the surface morphology of silicon: Effect of parasitic emitter etching on the rear side performance of silicon solar cells. In *Proceedings of the 25th European Photovoltaic Solar Energy Conference and Exhibition, Valencia, spain*, 2010.

[92] W. Kern and D. A. Puotinen. Cleaning solutions based on hydrogen peroxide for use in silicon semiconductor technology. *RCA Review*, 31:187, 1970.

[93] B. Vermang, A. Rothschild, K. Kenis, K. Wostyn, T. Bearda, A. Racz, X. Loozen, J. John, P. W. Mertens, J. Poortmans, et al. Surface passivation for Si solar cells: a combination of advanced surface cleaning and thermal atomic layer deposition of Al_2O_3. *Solid State Phenomena*, 187:357–361, 2012.

[94] A. Rothschild, J. Toman, J. Penaud, P. Jaffrennou, P. Choulat, E. Cornagliotti, M. R. Payo, B. Pawlak, J. Das, A. Uruena, et al. Impact of surface preparation prior to ALD-Al_2O_3 for PERC type solar cell. In *Proceedings of the 27th European Photovoltaic Solar Energy Conference, Frankfurt, Germany*, pages 1974–1977, 2012.

[95] B. Ferstl, S. Rajagopalan, S. Thate, M. Ross, E. Cornagliotti, M. Haslinger, and J. John. Investigation of wet chemical solutions performing pre-diffusion and pre-passivation cleans in next-generation PERC-type silicon solar cells. In *Proceedings of the 28th Photovoltaic Solar Energy Conference, Paris, France*, pages 1295–1299, 2013.

[96] E. J. Bergman, S. Lagrange, M. Claes, S. De Gendt, and E. Röhr. Pre-diffusion cleaning using ozone and hf. *Solid State Phenomena*, 76–77:85–88, 2001.

References

[97] G. M. Choi, I. Yokoi, and T. Ohmi. The role of oxidant in HF-based solution for noble metal removal from substrate. 76–77:267–270, 2001.

[98] A. Moldovan, K. Birmann, J. Rentsch, M. Zimmer, T. Gitte, and J. Fittkau. Combined Ozone/HF/HCI based cleaning and adjusted emitter etch-back for silicon solar cells. *Solid State Phenomena*, 195:305–309, 2013.

[99] J. L. Murray and A. J. McAlister. The Al-Si (aluminum-silicon) system. *Bulletin of Alloy Phase Diagrams*, 5(1):74–84, 1984.

[100] T. Lauermann, B. Fröhlich, G. Hahn, and B. Terheiden. Diffusion-based model of local al back surface field formation for industrial passivated emitter and rear cell solar cells. *Progress in Photovoltaics: Research and Applications*, 23(1):10–18, 2013.

[101] J. Müller, K. Bothe, S. Gatz, H. Plagwitz, G. Schubert, and R. Brendel. Contact formation and recombination at screen-printed local aluminum-alloyed silicon solar cell base contacts. *Electron Devices, IEEE Transactions on*, 58(10):3239–3245, 2011.

[102] J. Müller, K. Bothe, S. Gatz, and R. Brendel. Modeling the formation of local highly aluminum-doped silicon regions by rapid thermal annealing of screen-printed aluminum. *Physica Status Solidi – Rapid Research Letters*, 6(3):111–113, 2012.

[103] J. del Alamo, J. Eguren, and A. Luque. Operating limits of Al-alloyed high-low junctions for BSF solar cells. *Solid-State Electronics*, 24(5):415 – 420, 1981.

[104] M. Rauer, R. Woehl, K. Ruhle, C. Schmiga, M. Hermle, M. Horteis, and D. Biro. Aluminum alloying in local contact areas on dielectrically passivated rear surfaces of silicon solar cells. *IEEE Electron Device Letters*, 32(7):916–918, 2011.

[105] E. Urrejola, K. Peter, H. Plagwitz, and G. Schubert. Understanding and avoiding the formation of voids for rear passivated silicon solar cells. In *Presentation at the 3rd Metallization workshop, Charleroi, Belgium*, 2011.

[106] K. Dressler, S. Dauwe, T. Droste, J. Rossa, B. Meidel, K. Schünemann, K. Ramspeck, Y. Gassenbauer, and A Metz. Characterisation of rear local contacts including BSF formation using raman and scanning acoustic microscopy. In *Proceedings of the 27th European Photovoltaic Solar Energy Conference, Frankfurt, Germany*, pages 755–758, 2012.

[107] Y. Chen, P. P. Altermatt, J. Dong, S. Zhang, J. Liu, D. Chen, W. Deng, Y. Jiang, B. Liu, W. Xiao, H. Zhu, H. Chen, H. Jiao, X. Pan, M. Zhong, D. Wang, J. Sheng, Y. Zhang, H. Shen, Z. Feng, and P. J. Verlinden. Al-alloyed

106

local contacts for industrial PERC cells by local printing. In *Proceedings of the 40th IEEE Photovoltaic Specialist Conference*, pages 3322–3325, June 2014.

[108] R. Horbelt, G. Hahn, R. Job, and B. Terheiden. Void formation on PERC solar cells and their impact on the electrical cell parameters verified by luminescence and scanning acoustic microscope measurements. *Energy Procedia*, 84:47 – 55, 2015. Proceedings of the EMRS 2015 Spring meeting – Symposium C on Advanced Inorganic Materials and Structures for Photovoltaics.

[109] F. Lottspeich, M. Müller, M. Schuchart, T. Dullweber, G. Fischer, and E. Schneiderlöchner. Investigation of rear contact resistance of line contacted industrial PERC solar cells. In *Proceedings of the 30th European Photovoltaic Solar Energy Conference, Hamburg, Germany*, pages 485–488, 2015.

[110] D. Chen, W. Deng, J. Sheng, H. Zhu, M. Zhong, W. Wang, F. Ye, W. Cai, Z. Feng, Y. Zhang, et al. Preventing the formation of voids in the rear local contact areas for industrial-type PERC solar cells. In *Proceedings of the 28th European Photovoltaic Solar Energy Conference and Exhibition*, pages 770–774, 2013.

[111] K. Dressler, M. Kratt, P. A. Voss, S. Ebert, A. Herguth, and G. Hahn. Influence of Al particle size and firing profile on void formation in rear local contacts of silicon solar cells. *IEEE Journal of Photovoltaics*, 6(1):68–73, Jan 2016.

[112] C. Kranz, B. Wolpensinger, R. Brendel, and T. Dullweber. Analysis of local aluminum rear contacts of bifacial PERC+ solar cells. *IEEE Journal of Photovoltaics*, 6(4):830–836, 2016.

[113] E. Urrejola, K. Peter, H. Plagwitz, and G. Schubert. Silicon diffusion in aluminum for rear passivated solar cells. *Applied Physics Letters*, 98(15), 2011.

[114] A. D. Smigelskas and E. O. Kirkendall. Zinc diffusion in alpha brass. *Trans. Aime*, 171:130–142, 1947.

[115] J. Müller, K. Bothe, S. Gatz, F. Haase, C. Mader, and R. Brendel. Recombination at laser-processed local base contacts by dynamic infrared lifetime mapping. *Journal of Applied Physics*, 108(12), 2010.

[116] H. Plagwitz, M. Schaper, J. Schmidt, B. Terheiden, and R. Brendel. Analytical model for the optimization of locally contacted solar cells. In *Conference Record of the 31st IEEE Photovoltaic Specialists Conference*, pages 999–1002, 2005.

References

[117] S. Gatz, J. Müller, T. Dullweber, and R. Brendel. Analysis and optimization of the bulk and rear recombination of screen-printed PERC solar cells. *Energy Procedia*, 27:95 – 102, 2012. Proceedings of the 2nd International Conference on Crystalline Silicon Photovoltaics SiliconPV 2012.

[118] P. A. Basore. Extended spectral analysis of internal quantum efficiency. In *Conference Record of the 23rd IEEE Photovoltaic Specialists Conference*, pages 147–152, 1993.

[119] J. A. Rand and P. A. Basore. Light-trapping silicon solar cells-experimental results and analysis. In *Conference Record of the 22nd IEEE Photovoltaic Specialists Conference*, pages 192–197, 1991.

[120] E. Cornagliotti, A. Uruena, J. Horzel, J. John, L. Tous, D. Hendrickx, V. Prajapati, S. Singh, R. Hoyer, F. Delahaye, et al. How much rear side polishing is required? A study on the impact of rear side polishing in PERC solar cells. In *Proceedings of the 27th European Photovoltaic Solar Energy Conference, Frankfurt, Germany*, pages 561–566, 2012.

[121] J. Horzel, A. Lorenz, E. Cornagliotti, A. Uruena, J. John, M. Izaaryene, D. Habermann, P. Jaffrennou, and J. Penaud. Development of rear side polishing adapted to advanced solar cell concepts. In *Proceedings of the 26th European Photovoltaic Solar Energy Conference, Hamburg, Germany*, pages 2210–6, 2011.

[122] T. Dullweber, H. Hannebauer, C. Kranz, R. Hesse, S. Wyczanowski, V. Bhosle, C. Bubé, K. Weise, F. Delahaye, O. Doll, I. Kohler, and R. Brendel. Emitter technology options for industrial PERC solar cells with up to 20.3% conversion efficiency. *Photovoltaics International*, 21:44–50, 2013.

[123] S. Gatz, T. Dullweber, and R. Brendel. Evaluation of series resistance losses in screen-printed solar cells with local rear contacts. *IEEE Journal of Photovoltaics*, 1(1):37–42, 2011.

[124] M. Müller and F. Lottspeich. Evaluation of determination methods of the Si/Al contact resistance of screen-printed passivated emitter and rear solar cells. *Journal of Applied Physics*, 115(8), 2014.

[125] H. Plagwitz. *Surface passivation of crystalline silicon solar cells by amorphous silicon films.* PhD thesis, Gottfried Wilhelm Leibniz Universität Hannover, 2007.

[126] K. C. Fong, K. R. McIntosh, and A. W. Blakers. Accurate series resistance measurement of solar cells. *Progress in Photovoltaics: Research and Applications*, 21(4):490–499, 2013.

[127] B. Gelmont, M. S. Shur, and R. J. Mattauch. Disk and stripe capacitances. *Solid-State Electronics*, 38(3):731 – 734, 1995.

[128] E. Urrejola, K. Peter, H. Plagwitz, and G. Schubert. Al-Si alloy formation in narrow *p*-type Si contact areas for rear passivated solar cells. *Journal of Applied Physics*, 107(12), 2010.

[129] T. Weber, G. Fischer, A. Oehlke, C. Kusterer, K. Strauch, R. Schiepe, M. Mühlbauer, M. Müller, F. Wolny, R. Köhler, G. Grupp-Mueller, E. Schneiderlöchner, K.H. Stegemann, and H. Neuhaus. High volume pilot production of high efficiency PERC solar cells – analysis based on device simulation. *Energy Procedia*, 38:474, 2013.

[130] F. Seitz. On the porosity observed in the Kirkendall effect. *Acta Metallurgica*, 1(3):355 – 369, 1953.

[131] G. A. Storaska and J. M. Howe. In-situ transmission electron microscopy investigation of surface-oxide, stress-relief mechanisms during melting of sub-micrometer Al-Si alloy particles. *Materials Science and Engineering: A*, 368(1–2):183 – 190, 2004.

[132] M. Balucani, L. Serenelli, K. Kholostov, P. Nenzi, M. Miliciani, F. Mura, M. Izzi, and M. Tucci. Aluminum-silicon interdiffusion in screen printed metal contacts for silicon based solar cells applications. *Energy Procedia*, 43:100 – 110, 2013. Proceedings of the Fourth Workshop on Metallization for Crystalline Silicon Solar Cells.

[133] S. Großer, M. Werner, and C. Hagendorf. Microstructure of void formation stages at local rear contacts. *Energy Procedia*, 77:701 – 706, 2015.

[134] T. Miyoshi, S. Hara, T. Mukai, and K. Higashi. Development of a closed cell aluminum alloy foam with enhancement of the compressive strength. *Materials Transactions*, 42(10):2118–2123, 2001.

[135] A. A. Stekolnikov, J. Furthmüller, and F. Bechstedt. Absolute surface energies of group-IV semiconductors: Dependence on orientation and reconstruction. *Phys. Rev. B*, 65:115318, 2002.

[136] R. Brendel, S. Dreissigacker, N.-P. Harder, and P. P. Altermatt. Theory of analyzing free energy losses in solar cells. *Applied Physics Letters*, 93(17), 2008.

[137] P. J. Verlinden, M. Aleman, N. Posthuma, J. Fernandez, B. Pawlak, J. Robbelein, M. Debucquoy, K. Van Wichelen, and J. Poortmans. Simple power-loss analysis method for high-efficiency Interdigitated Back Contact (IBC) silicon solar cells. *Solar Energy Materials and Solar Cells*, 106:37 – 41, 2012.

[138] J. H. Petermann. PhD thesis, Gottfried Wilhelm Leibniz Universität Hannover, 2014.

References

[139] R. Brendel. Sunrays: A versatile raytracing program for the photovoltaic community. In *Proceedings of the 12th European Photovoltaic Solar Energy Conference*, 1994.

[140] Synopsys, Inc., Mountain View, CA. *Sentaurus Process User Guide, Version G-2012.06.* 2012.

[141] Linear technology. Available at: `http://www.linear.com/designtools/software/` [accessed on 03 Jun 2016].

[142] P. P. Altermatt, J. O. Schumacher, A. Cuevas, M. J. Kerr, S. W. Glunz, R. R. King, G. Heiser, and A. Schenk. Numerical modeling of highly doped Si:P emitters based on Fermi-Dirac statistics and self-consistent material parameters. *Journal of Applied Physics*, 92(6):3187–3197, 2002.

[143] L. E. Black and K. R. McIntosh. Modeling recombination at the Si-Al$_2$O$_3$ interface. *IEEE Journal of Photovoltaics*, 3(3):936–943, 2013.

[144] T. Dullweber, C. Kranz, U. Baumann, R. Hesse, D. Walter, J. Schmidt, P. Altermatt, and R. Brendel. Silicon wafer material options for highly efficient p-type PERC solar cells. In *Proceedings of the IEEE 39th Photovoltaic Specialists Conference*, pages 3074–3078, 2013.

[145] A. Richter, M. Hermle, and S. W. Glunz. Reassessment of the limiting efficiency for crystalline silicon solar cells. *IEEE Journal of Photovoltaics*, 3 (4):1184–1191, 2013.

List of publications

Refereed journal papers

1. C. Kranz, B. Wolpensinger, R. Brendel, T. Dullweber. Analysis of local aluminum rear contacts of bifacial PERC+ solar cells. *IEEE Journal of Photovoltaics*, vol. 6 (4), p. 830–836, 2016.

2. C. Kranz, U. Baumann, B. Wolpensinger, F. Lottspeich, M. Müller, P. Palinginis, R. Brendel, T. Dullweber. Void formation in screen-printed local aluminum contacts modeled by surface energy minimization. *Solar Energy Materials & Solar Cells*, vol. 158, p. 11–18, 2016.

3. T. Dullweber, C. Kranz, R. Peibst, U. Baumann, H. Hannebauer, A. Fülle, S. Steckemetz, T. Weber, M. Kutzer, M. Müller, G. Fischer, P. Palinginis, H. Neuhaus. PERC+: Industrial PERC solar cells with rear Al grid enabling bifaciality and reduced Al paste consumption. *Progress in Photovoltaics - Research and Applications*, vol. 24, p. 1487–1498, 2015.

4. T. Dullweber, C. Kranz, B. Beier, B. Veith, J. Schmidt, B.F.P. Roos, O. Hohn, T. Dippell, R. Brendel. Inductively coupled plasma chemical vapour deposited AlO_x/SiN_y layer stacks for applications in high-efficiency industrial-type silicon solar cells. *Solar Energy Materials & Solar Cells*, vol. 112, p. 196–201, 2013.

5. R. Brendel, T. Dullweber, R. Peibst, C. Kranz, A. Merkle, D. Walter. Breakdown of the efficiency gap to 29% based on experimental input data and modeling. *Progress in Photovoltaics - Research and Applications*, doi:10.1002/pip.2696, 2015.

Non-refereed journal papers

1. T. Dullweber, C. Kranz, R. Peibst, U. Baumann, H. Hannebauer, A. Fülle, S. Steckemetz, T. Weber, M. Kutzer, M. Müller, G. Fischer, P. Palinginis, H. Neuhaus. The PERC+ cell: More output power for less aluminum paste. *Photovoltaics International*, vol. 30, p. 53–63, 2016.

2. T. Dullweber, H. Hannebauer, C. Kranz, R. Hesse, S. Wyczanowski, V. Bhosle, C. Dubé, K. Weise, R. Delahaye, O. Doll, I. Köhler, R. Brendel. Emitter technology options for industrial PERC solar cells with up to 20.3% conversion efficiency. *Photovoltaics International*, vol. 21, p. 1–7, 2013.

Refereed conference papers

1. C. Kranz, J.H. Petermann, T. Dullweber, R. Brendel. Simulation-based efficiency gain analysis of 21.2%-efficient screen-printed PERC solar cells. *Energy Procedia*, vol 92, p. 109–115, 2016.

2. C. Kranz, B. Lim, U. Baumann, T. Dullweber. Determination of the contact resistivity of screen-printed Al contacts formed by laser contact opening. *Energy Procedia*, vol. 67, p. 64–69, 2014.

3. C. Kranz, S. Wyczanowski, U. Baumann, S. Dorn, S. Queisser, J. Schweckendiek, D. Pysch, T. Dullweber. Industrial cleaning sequences for Al2O3-passivated PERC solar cells. *Energy Procedia*, vol. 55, p. 211–218, 2014.

4. C. Kranz, S. Wyczanowski, U. Baumann, K. Weise, C. Klein, F. Delahaye, T. Dullweber, R. Brendel. Wet chemical polishing for industrial type PERC solar cells. *Energy Procedia*, vol. 38, p. 243–249, 2013.

5. C. Kranz, S. Wyczanowski, S. Dorn, K. Weise, C. Klein, K. Bothe, T. Dullweber, R. Brendel. Impact of the rear surface roughness on industrial-type PERC solar cells. *27th European Photovoltaic Solar Energy Conference and Exhibition*, Frankfurt, Germany, p. 557–560, 2012.

6. T. Dullweber, C. Kranz, R. Peibst, U. Baumann, H. Hannebauer, A. Fülle, S. Steckemetz, T. Weber, M. Kutzer, M. Müller, G. Fischer, P. Palinginis, D. H. Neuhaus. The PERC+ cell: a 21%-efficient industrial bifacial PERC solar cell. *31st European Photovoltaic Solar Energy Conference and Exhibition*, Hamburg, Germany, p. 341–350, 2015.

7. T. Dullweber, C. Kranz, U. Baumann, R. Hesse, D. Walter, J. Schmidt, P. Altermatt, R. Brendel. Silicon wafer material options for highly efficient p-type PERC solar cells. *Proc. 39th IEEE Photovoltaic Specialists Conference*, Tampa, USA, 2013.

8. B. Veith, T. Dullweber, M. Siebert, C. Kranz, F. Werner, N.-P. Harder, J. Schmidt, B.F.P. Roos, T. Dippell, R. Brendel. Comparison of ICP-AlO$_x$ and ALD-Al$_2$O$_3$ layers for the rear surface passivation of c-Si solar cells. *Energy Procedia*, vol. 27, p. 379–384, 2012.

9. T. Dullweber, M. Siebert, B. Veith, C. Kranz, J. Schmidt, R. Brendel, B.F.P. Roos, T. Dippell, A. Schwabedissen, S. Peters. High-efficiency industrial-type PERC solar cells applying ICP AlO$_x$ as rear passivation layer. *27th European Photovoltaic Solar Energy Conference and Exhibition*, Frankfurt, Germany, p. 672–675, 2012.

Prizes and Awards

- SiliconPV Award 2016 for the contribution "*Analysis of local aluminum back surface fields of bifacial PERC+ solar cells*" as one of the 10 best ranked contributions of the SiliconPV 2016 conference.

- Member of the project team HighScreen, that won the enercity award 2015 by developing an industrial-type PERC solar cell with a record efficiency of 21.2%.

Lebenslauf

Persönliche Daten

Name	Christopher Kranz
Anschrift	Eichenkamp 21, 31789 Hameln
Geburtsdatum	30. Juni 1985
Geburtsort	Minden
Nationalität	deutsch

Ausbildung

Juni 2004	Abitur am Städtischen Gymnasium Porta Westfalica
Juli 2004 - März 2005	Grundwehrdienst in Coesfeld und Minden
Oktober 2005 - Juli 2011	Studium der Physik an der Westfälischen Wilhelms-Universität Münster Diplom im Juli 2011
Okt. 2011 - Sep. 2016	Doktorand am Institut für Solarenergieforschung Hameln (ISFH)

Danksagung

Ganz herzlich möchte ich mich bei all denen bedanken, die zum Gelingen dieser Arbeit beigetragen haben:

- Allen Kollegen am ISFH für das sehr angenehme und freundliche Arbeitsklima, die stetige Diskussionsbereitschaft bei Fachfragen sowie die zahllosen Tipps und Anregungen.

- Allen ehemaligen Mitgliedern der "Kochgruppe", die mir am Mittagstisch Gesellschaft geleistet haben und mich stets mit leckerem Essen versorgt haben, darunter: Udo Römer, Ralf Gogolin, Marco Ernst, Martin Lehr, Michael Rienäcker, Malte Vogt, Irene Berardone, Henning Schulte-Huxel, Andreas Moor u.v.m.

- Meinen Kollegen und Freunden Udo Römer und Ralf Gogolin für die super Bürogemeinschaft, die enge Zusammenarbeit und die schönen Momente auf und nach der Arbeit.

- Meiner Familie für die liebevolle Unterstützung.

- Meiner Freundin Stefanie Fussek für die moralische Unterstützung während der Zeit des Zusammenschreibens.